PREPARATION AND CHARACTERIZATION OF SINTERED Ti-6Al-4V POWDER COMPACTS

By

Emrah ÇELİK

A Dissertation Submitted to the
Graduate School in Partial Fulfillment of the
Requirements for the Degree of

MASTER OF SCIENCE

Department: Materials Science and Engineering
Major: Materials Science and Engineering

İzmir Institute of Technology
İzmir, Turkey

July, 2004

ACKNOWLEDGMENTS

I am very grateful to Associate Professor Mustafa Güden for his supervision, kind guidance and support during my studies. I would like to thank Associate Professor Sedat Akkurt for his valuable comments and recommendations. I am also very grateful to University of Delaware staff for high strain rate compression tests. I would like to thank Egemen Akar, master degree student and Levent Saatçi, undergraduate student, for their assistance in my experimental studies. I would also thank to IYTE-MAM staff for their helps during my material characterization processes. Finally, I would like to acknowledge Hipokrat A.Ş. for financial support given to my thesis.

ABSTRACT

Sintered Ti6Al4V powder compacts were prepared using atomized spherical and angular powders in the porosity range of 29-63%. Cylindrical green powder compacts were cold compacted at various compaction pressures and then sintered at 1200 ^{o}C for 2 h. The final porosities and average pore sizes were determined as functions of the applied compaction pressure and powder type. The compression deformation behavior of Ti6Al4V powder compacts was also investigated at quasi-static ($1.6x10^{-3}$-$1.6x10^{-1}s^{-1}$) and high strain rate (300 and 900 s^{-1}) conditions using conventional mechanical testing and Split Hopkinson Pressure Bar techniques, respectively.

The mean pore size of the compacts varied between 29 and 171 μm depending on the particle size range of the powders used and the compaction pressure applied. Microscopic studies of as-received powders and sintered powder compacts showed that sintering at high temperature (1200^{o}C) and subsequent relatively slow-rate cooling in the furnace transformed the microstructure of spherical powder from the acicular alpha (α) to the Widmanstätten (α+β) microstructure and angular powder from bimodal to equiaxed+ Widmanstätten microstructure.

In compression testing, at both quasi-static and high strain rate conditions, the compacts failed primarily by shear band formation along the diagonal axis 45° to the loading direction. Increasing strain rate ($\dot{\varepsilon}$) was found to increase both the flow stress and the compressive strength of spherical powder compacts while it did not affect the critical strain for shear localization. The mechanical properties of angular powder compacts were further shown to be a function of powder size; larger the particle size higher the percentage of equiaxed structure while in compacts of particles <100 μm relatively large voids resulted in reduced strength and ductility. Microscopic analyses of deformed but not failed and failed spherical powder compact samples further showed that fracture occurred in a ductile (dimpled) mode consisting of void initiation and growth in α phase and/or at the α/β interface and macrocraking by void coalescence in the interparticle bond region. In angular powder compacts, the failure was granular brittle type at the interparticle bond region while the compact samples of particles <100 μm fractured transgranularly through the voids.

The strength of the sintered compacts was further shown to satisfy the strength requirements for cancellous bone replacement. The strength of the compacts having porosity level of 40% and/or lower was comparable with that of human cortical bone. Compared to Ti powder compacts of previous studies, Ti6Al4V powder compacts provided higher strength and increased porosity level of the compacts suitable for cortical bone replacement.

ÖZ

Küresel şekilli ve şekilsiz tozlar kullanılarak, 29-63% gözenek aralığında sinterlenmiş Ti6Al4V toz tabletleri hazırlanmıştır. Silindirik tabletler farklı basınçlarda preslenerek 1200 °C’de 2 saat sinterlenmiştir. Sinterlenen tabletlerin gözenek miktarları ve ortalama gözenek boyutları uygulanan presleme basıncı ve toz çeşidine göre tespit edilmiştir. Ayrıca, Ti6Al4V toz tabletlerin basma altındaki deformasyon davranışları geleneksel mekanik test ve Split Hopkinson dinamik test teknikleri kullanılarak statik ($1.6x10^{-3}$-$1.6x10^{-1}s^{-1}$) ve dinamik (300 and 900 s^{-1}) deformasyon hızlarında araştırılmıştır.

Tabletlerin ortalama gözenek boyutları kullanılan tane boyutu ve uygulanan presleme basıncına bağlı olarak 34 ile 171 μm arasında değişim göstermiştir. Ayrıca başlangıç tozlarının ve sinterlenen tabletlerin mikroskopik incelenmesi, yüksek sıcaklıkta (1200 °C) yapılan sinterleme ve ardından fırın içinde uygulanan düşük hızlı soğutmanın sonucunda, küresel tozun mikroyapısının iğnemsi alfa (α)‘ dan Widmanstätten (α+β) yapısına, şekilsiz tozun ise ikili mod yapısından eş taneli+ Widmanstätten mikroyapısına değiştiğini göstermiştir.

Statik ve dinamik basma testlerinde tabletlerin, yükleme doğrultusuna 45° açıyla, diyagonal olarak ortaya çıkan kayma bantları oluşumu ile kırıldıkları tespit edilmiştir. Küresel toz tabletlerde şekil değişim hızının $(\dot{\varepsilon})$ artması kayma yoğunlaşması için kritik olan şekil değişimini etkilememekle beraber gerek akma gerilmesinin gerekse basma mukavemetinin artmasına neden olmuştur. Ayrıca şekilsiz toz tabletlerin mekanik özellikleri toz boyutuna bağlı olarak belirlenmiştir. Büyük tanelerden oluşan tabletler daha yüksek oranda eş tane yapıya sahiplerken 100 μm den küçük tozların oluşturduğu kompaktlarda mukavemeti ve süneklği önemli ölçüde düşüren boşluklar gözlenmiştir. Kırılan ve deformasyona uğramış ancak kırılma gözlemlenmemiş kompaktlara uygulanan mikroskobik analizler, α fazında ve/veya α/β arayüzeyinde oluşan boşluk oluşumu, büyümesi ve taneler arası bağlanma bölgesinde meydana gelen makro çatlak oluşumu aşamalarını içeren sünek kırılmanın varlığını ortaya koymuştur. Şekilsiz toz tabletlerde kırılma, taneler arasındaki bağlanma bölgesinde oluşan taneli gevrek kırılmadır. Ancak, 100 μm boyutundan küçük tozlardan

üretilmiş olan tabletlerde kırılma bu tabletlerde görülen boşluklar vasıtasıyla taneler boyunca oluşmaktadır.

Sinterlenmiş tabletlerin mukavemetinin süngersi kemik değişimi için yeterli olduğu gösterilmiştir. Bunun yanında, %40 ve/veya daha düşük gözenek oranına sahip tabletlerin mukavemetlerinin insan kortikal kemiğinin mukavemetiyle kıyaslanabilir olduğu belirlenmiştir. Daha önceki çalışmalarda üretilen Ti tabletlerle karşılaştırıldığında Ti6Al4V toz tabletler daha yüksek mukavemete ve bu nedenle de kortikal kemik değişimi için uygun olan gözenek miktarının artmasına neden olmuştur.

TABLE OF CONTENTS

LIST OF FIGURES

LIST OF TABLES

Chapter 1

INTRODUCTION

Biomaterials, either natural or synthetic, find a wide range of medical and dental implant and prosthesis applications for the repair or replacement of natural tissues. They are in many applications used directly to support or replace the functions of living tissues of the human body. The need for novel biomaterials developed based on available materials processing to tackle with current existent problems of biomedical applications is increasing constantly.

The use of common engineering group of materials for the replacement of human body tissues was not a new concept and dates far back into ancient civilizations. Artificial eyes, ears, teeth, and noses were found on Egyptian mummies [1]. Over the centuries, advancements in synthetic materials, surgical techniques and sterilization methods have permitted the use of biomaterials in many ways. Today a large number of devices and implants are widely used to replace and restore the functions of deformed or degenerated tissues or organs. They assist in healing to improve function, to correct abnormalities, and thus improve the quality of life of the patients. Synthetic implant materials are currently produced from all varieties of materials, metals, ceramics, polymers and their composites.

Metals have a particular importance among the biomaterials because of their superior mechanical properties combined with relatively easy production lines and lower costs. Many metals, including even copper which is known as a toxic material for human body, have been used in biomedical applications since ancient times. Cobalt (Co) based alloys, stainless steels and titanium (Ti) and its alloys are three major metallic materials widely used in implant applications. Ti and its alloys have been recently attracted more interest despite their higher cost and complex production processes than other metals. Their major advantage lies in its inherent corrosion resistance, which is attributable to the spontaneous formation of an oxide layer particularly resistant to many acids and saline solutions. Excellent biocompatibility and fatigue properties are other advantages of Ti and its alloys. These superior properties have made Ti and its alloys one of the most important class of materials in orthopedic and dental applications.

Unfortunately, most bulk metallic implant materials currently used in orthopedic applications including Ti and its alloys, suffer from problems of interfacial stability with host tissues and biomechanical mismatch of elastic moduli. These problems stem from weak bonding of implant to the adjacent bone and high elastic modulus of bulk metallic implants. Developments in tissue engineering have demonstrated that these problems can be solved using porous implant components based on biocompatible metallic materials by providing better interaction with bone. This is partly due to higher degree of bone growth into porous surfaces and higher degree of body fluid transport through three-dimensional interconnected array of pores [2], leading to improved implant fixation. Furthermore, relatively low elastic modulus of porous metals as compared with those of bulk metals is expected to reduce the extent of stress shielding, which causes the well-known *implant loosening,* and hence to prolong implant life-time [3].

Open cell Ti foams potentially to be used in biomedical applications were previously prepared using a powder metallurgical process, known as space holder method [4-5]. This method allows a direct near net-shape fabrication of foamed implant components having elastic modulus comparable with that of natural bone and with a relatively homogeneous pore structure and a high level of porosity (60-80%) [4-5]. By reducing the "elastic-mismatch" as well as "strength-mismatch" between metallic implant and bone, it is expected to have better performance of implant-bone compound which can be called as "iso-elastic multi-material system". For this purpose several innovative investigations have been undertaken world-wide. Oh and co-workers [6] reported that the modulus and bending strength of sintered Ti powder compacts were also comparable with those of human bone. It was further shown by the same authors that the porosity level of sintered Ti compacts suitable for the bone replacement was around 30%, which was in accord with the proposed optimal porosity for the ingrowths of new-bone tissues. The compressive yield strength of sintered Ti compacts was however lower than that of the human cortical bone due to the relatively low yield strength of Ti powder [6]. One way of increasing the yield strength of powder compacts is to use biocompatible stronger Ti alloy powders. This experimental study is therefore conducted to produce stronger sintered powder compacts that can potentially be used in biomedical applications (load carrying implants) including human cortical bone replacement. The experimental work presented focused so far on (a) the preparation of Ti6Al4V compacts with various porosity and pore sizes using commercially available powders and (b) the determination of compression mechanical properties of compacts as function of porosity at quasi-static and high strain rates. The interest in strain rate dependent properties of compact simply arises from the fact that the mechanical properties of bone are strain rate sensitive as recently shown by Yeni and Fyrie [7] on the basis of extensive literature survey. The ultimate goal of the work was the optimization of the process and properties to satisfy the bio-mechanical design requirements for certain implants.

Chapter 2

BIOMATERIALS

Biomaterials can be defined as any substance that has the capacity to function in contact with living tissue and not be rejected by the body. Biomaterials can be produced from metals, ceramics and polymers and used for the reconstruction or repair of a tissue. The use of synthetic biomaterials to repair or replace defects in the human body dates back thousands of years. Early civilizations such as the Egyptians, Romans and Aztecs used wood, ivory, gem stones and other objects to replace missing teeth and fill in bone defects more than 2,500 years ago. Since then, scientific developments have led to the use of a number of different synthetic and natural materials in the human body. From World War I through World War II a number of natural rubbers, celluloids, vinyl polymers and polyurethanes were used for grafts, artificial hearts and catheters. During World War II, silicon was used in Japan to enhance the breasts of prostitutes and polymethylmethacrylate (PMMA), the main component in many of today's bone cements, was used in dental and craniofacial applications. Metallic alloys have been used as pins and plates in the human body since the early nineteenth century.

Biomaterials are expected to perform in body’s very aggressive internal environment. For example the pH of body fluids in different tissues varies in the range from 1 to 9. The mean load on a hip joint is up to 3 times body weight (3000 N) and peak load during jumping can be as high as 10 times body weight [1]. It should also be noted that the stresses are repetitive and fluctuating depending on the activities such as standing, sitting, jogging, stretching and climbing. The biological environment depends also on the patient’s conditions and activities.

Any natural or synthetic material that interfaces with living tissue or biological fluids may be classified as a biomaterial. Clinical experience however indicates that only various materials are suitable for biomedical applications for that certain physical, chemical, and mechanical characteristics make some materials more desirable than others for biological applications. Determination of these desirable properties depends on the material’s intended use in the body. For example, the material for a bone implant must exhibit high compressive strength, while the material for a ligament replacement must display far more flexibility and tensile strength. In Figure 2.1, tensile stress and elastic modulus properties of several different materials including metals, ceramics, polymers and composites are shown as a guide for the material selection based on the mechanical aspects. For the replacement of bone tissue, for example materials that have similar mechanical properties with those of natural bone should be chosen from this figure. In all cases, however, the biocompatibility and in some cases, bioactivity of the material comprise key factors in determining whether a new graft or implant succeeds in the body.

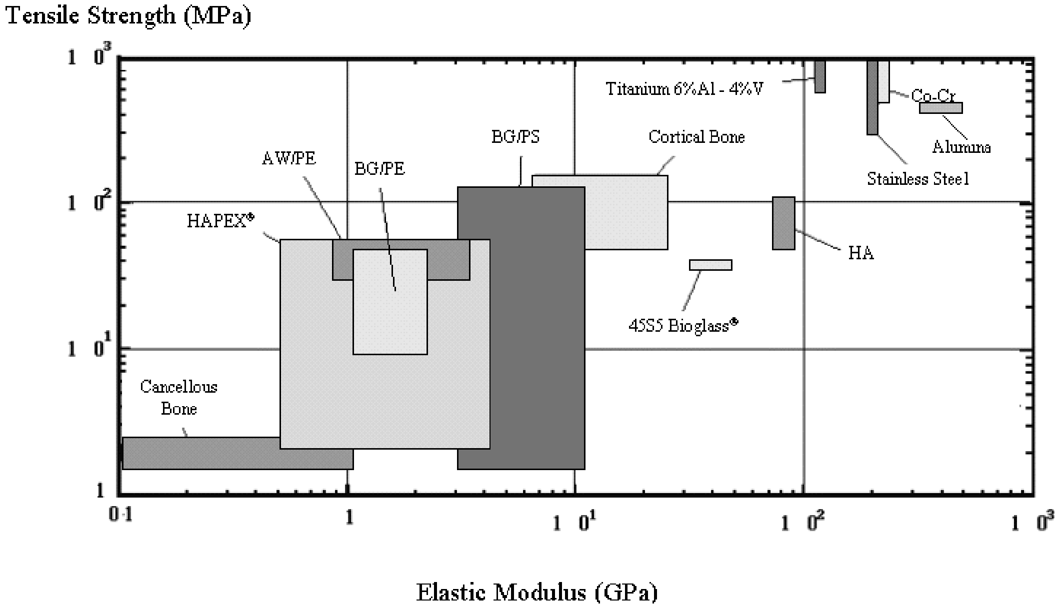

Figure 2.1 Tensile strength-elastic modulus of several materials.

In the early days all kinds of natural materials such as wood, glue and rubber and tissue from living forms and manufactured materials such as iron, gold, zinc and glass were used as biomaterials based on trial and error. The responses of the body to these materials were also extremely different. Some materials were accepted by the body whereas others were not. Over the last 30 years considerable progress has been made in understanding the interactions between the tissues and the materials. It has been acknowledged that there are profound differences between non-living and living materials. Scientists have used the word of biocompatibility to indicate the biological performance of biomaterials. Biocompatibility is a descriptive term which indicates the ability of a material to perform with an appropriate host response, in a specific application. In simple terms it implies compatibility or harmony of the biomaterial with the living system. A biocompatible material deteriorates normal body functions as little as possible. Therefore, the biocompatible material causes no thrombogenic, toxic, or allergic inflammatory response when placed in vivo. The material must not stimulate changes in plasma proteins and enzymes or cause an immunologic reaction, nor can it induce carcinogenic and mutagenic effects. Furthermore, it should be noted that success of a biomaterial in the body also depends on many other factors such as surgical techniques, health condition and activities of the patient.

Bioactive materials play a more aggressive role in the body. While a biocompatible material should affect the equilibrium of the body as little as possible, a bioactive material may form specific interactions between the material and surrounding tissue. Although many current medical procedures call for inert biocompatible materials, the increasing understanding of tissue interaction promises many more applications for aggressive bioactive materials.

2.1 Polymers

Polymers consist of small repeating units, or isomers, bound together in long chains. The flexible structure of polymers has enabled this group of materials to be useful in many applications such as plastic garbage bags and rubber tires. In many materials, processing conditions can induce the polymer chains to link with each other along the length of the chain to produce a wide variety of mechanical properties. The process, known as cross-linking, can increase the density of materials to improve their strength and hardness. However, cross-linked materials often loose their flexibility and become more brittle. These parameters are easily varied in order to suit current biomedical applications.

The wide use of polyethylene (PE) in medicine illustrates the typical versatility of a polymer. Depending on the processing of the material, PE can be elastic and flexible, or hard and smooth. Low-density polyethylene serves as tubing in catheters, while ultra-high-molecular-weight (UHMW) polyethylene is one of the major joint surfaces used in total hip or knee replacements. The smooth surface of UHMW creates extremely low friction with other materials and increases the durability of the artificial joint. Figure 2.2 (a) shows an acetabular cup produced from UHMW polyethylene material.

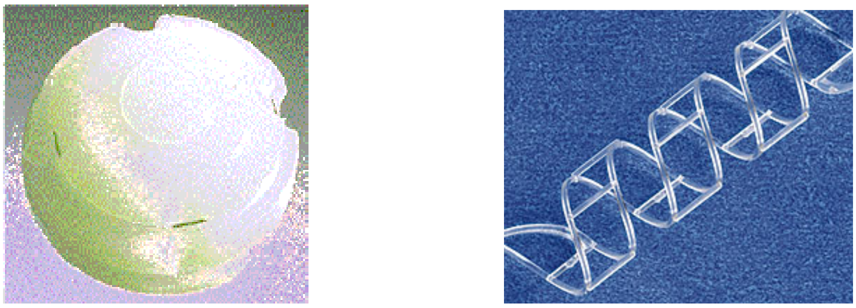

(a) (b)

Figure 2.2 Polymeric biomaterials (a) acetabular cup and (b) biodegradable stent.

Hydrogels comprise another subdivision of this unique group of materials. These polymer structures form a hydrophilic cross-linked network that swells in water until equilibrium is reached between the bonding force of the network and the thermodynamic swelling force. The applications of hydrogels cover a range as broad as their physical properties. The ability of hydrogels to swell and dehydrate depending on composition and environment can be used to facilitate the controlled release of drugs. Soft contact lenses also rely on their hydrogel content to induce equilibrium between the lens and the surface of the eye, at the same time allowing gas exchange and visibility without distortion. These polymers show promise in blood contact applications as well as wound-healing and artificial cartilage and skin.

Natural and synthetic biodegradable polymers have emerged as reliable and effective materials for purposes that require only temporary stability in order to support tissue ingrowth. Biodegradable polymers degrade when placed in the body while allowing functional tissue to grow in its place. Biodegradable stent is given in Figure 2.2 (b) for an example of biodegradable polymeric biomaterials. Typical applications of these polymers include their use in absorbable sutures. These sutures degrade slowly into by products that the body can destroy through natural functions and they eliminate the need for a second operation to remove them. Biodegradable polymers show promise in many tissue engineering applications due to their ability to degrade while encouraging functional tissue from the body to take its place.

Biodegradable polymers can be natural or synthetic. Some natural polymers include collagen, which already comprises about 30% of the protein in the body, chitosan, which is derived from a polysaccharide called chitin found in crustacean exoskeletons, and polyhydroxyalkanoates (PHA), which are secreted by certain species of microorganisms. Synthetic polymers include polyglycolicacid (PGA), which has been used in absorbable sutures, polylacticacid (PLA), copolymers of PGA and PLA, and polydioxananone (PDS).

2.2 Ceramics

This category consists of inorganic, nonmetallic compounds that exhibit a variety of combinations of ionic and covalent bonding. They have been widely used in biomedical applications for load bearing implants and the dental industry. Most members of this group are characterized by a high Young's modulus, very low ductility, and a hard, brittle surface. They can be used for load bearing applications, such as total hip replacements. Alumina, for example, is often used as a pair in a ball and socket hip implant. Porous ceramic materials exhibit much lower strengths but have been found extremely useful as coatings for metallic implants. The coating aids in tissue fixation of the implant by providing a porous surface for the surrounding tissue to grow into and provide mechanical interlocking. Certain ceramics are considered as bioactive ceramics if they establish bonds with bone tissue. This bonding activity increases the interfacial strength of adhesion greatly. Hydroxyapatite (HA) is a natural mineral component of bone tissue that can be added into the implants to encourage bone ingrowth that can reinforce implants as they begin to age. The images of porous HA biomaterials used as biomaterial are shown in Figure 2.3.

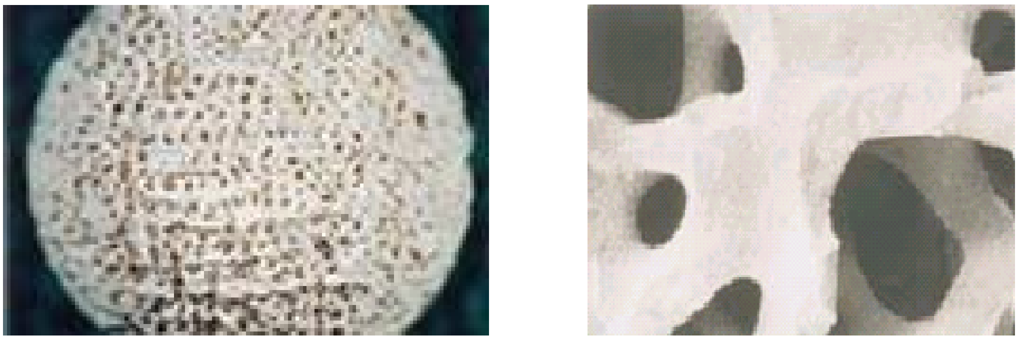

Figure 2.3 Porous Hydroxyapatite (HA).

2.3 Metals

Metallic biomaterials have the longest history among all synthetic biomaterials. The use of gold as a dental biomaterial existed nearly 2000 years ago. Similarly, bronze and copper also found application despite the toxic effect of copper for body. At the present, metals are still widely used due to their biocompatibility and mechanical properties. Closely packed crystal structure and metallic bonding in metals or metal alloys make them valuable as load bearing implants and internal fixation devices in large part for orthopedic applications as well as dental implants. Three major metallic biomaterials in these application fields are stainless steel, Ti and its alloys, and Co-based alloys. They contribute high tensile, fatigue and yield strengths; low reactivity and good ductility for the implant devices. Their properties depend on the processing method and purity of the metal. Examples of metallic implants are shown in Figure 2.4.

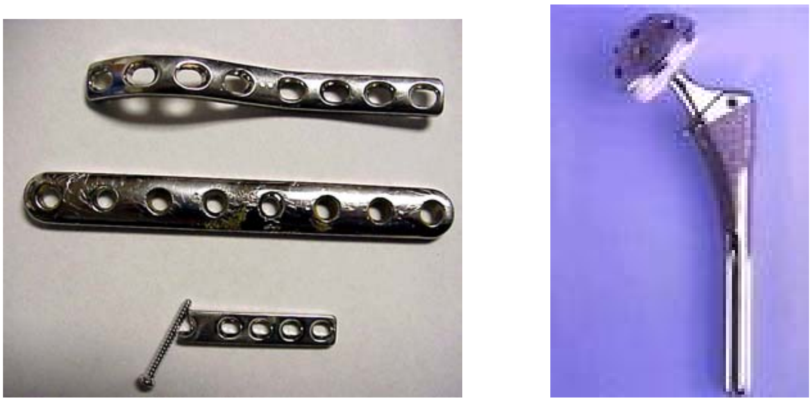
(a) (b)

Figure 2.4 Examples for metallic biomaterials (a) fixation equipments and (b) Femoral stem.

The number of the aged people demanding replacement of failed tissue with metallic biomaterials is growing. The development of metallic materials for biomedical applications is very important. According to the background on the metallic biomaterials, there is a trend for development of new metallic biomaterials especially on the improvement of biocompatibility and mechanical properties of these materials. New generation Ti alloys are produced for this purpose.

2.4 Titanium and its alloys

Ti and its alloys are used in a variety of demanding applications in which reliability and performance are of major concern. Ti alloys surpass the competition because of the superior strength to weight ratio that they possess. They are taking more attention in both medical and dental fields because of excellent biocompatibility, light weight, mechanical properties and corrosion behavior. Commercially pure Ti and its alloys are routinely used in a variety of biomedical applications such as: implants for dental (Figure 2.5 (a)) and orthopedic surgery; prosthesis devices such as total joint replacement, in particular for hip (Figure 2.5 (b)) and knee joints; osteosynthesis devices such as bone fracture plates and screws and spinal surgery devices; prosthetic heart valves, artificial hearts, pacemakers, and vascular stent components in cardiac and cardiovascular applications; and bone-anchored hearing aids in audiological applications [8].

(a) (b)

Figure 2.5 Applications of Ti and its alloys (a) dental root implant and (b) hip joint.

Ti and its alloys show the best biocompatibility among the metallic biomaterials. From the point of view of allergy problems, Ti and its alloys are also advantageous for biomedical applications. Fracture of the alloys is, however, one of the biggest problems for their reliable use in the body. The fracture characteristics of the alloys are affected by changes in microstructure. Therefore, their fracture characteristics, including tension and fatigue should be clearly understood with respect to microstructures. The fracture characteristics in the simulated body environment should also be identified. The effect of living body environment on the mechanical properties is also very important parameter affecting the implant life.

Commercially pure Ti, Ti6Al4V and Ti6Al4V ELI have basically been developed for structural materials although they are still widely used as representative Ti alloys for implant materials. Low modulus alloys are nowadays desired because the moduli of alloys are required to be more similar to that of bone. They are composed of nontoxic elements such as Nb, Ta, and Zr. Pure Ti and Ti6Al4V are also the main implant materials in the dental field. Ti alloys for dental implant materials are the same as those for surgical implant materials.

The interpretation of Ti alloy microstructures has assisted in the design of alloys for particular applications by manipulating the parameters of composition, processing and heat treatment to develop microstructures that correspond to the desired mechanical properties. Ti undergoes an allotropic transformation at 882 °C, having a body centered cubic structure, beta (β) phase above the transformation temperature and hexagonal close packed structure, alpha phase (α) below 882 °C. This allotropic nature of Ti provides the basis for the development of a large spectrum of alloy compositions. Various alloying elements can raise or lower the transformation temperature, resulting in stabilization of either α or β phase. Alloying elements used to stabilize α and β phases are tabulated in Table 2.1. The alloying element selection is made for the intended purpose of applications. For example, lenticular alpha (α) phase is known to provide excellent elevated-temperature creep resistance, hence alloys to be used in high temperature applications are specifically formulated to stabilize the α phase. Similarly, properties such as corrosion resistance, fracture toughness and fatigue life can be optimized by means of alloy addition to manipulate the microstructure.

Table 2.1 Alloying elements of titanium and their effects.

Alloying Element	**Effect**
Aluminum	α stabilizer
Tin	α stabilizer
Vanadium	β stabilizer
Molybdenum	β stabilizer
Chromium	β stabilizer
Zirconium	A and β strengthener

Many of the alloys developed for structural applications however contain a mixture of α and β phases, whose morphologies and distributions can be altered by processing or heat treatment. In addition, depending upon alloy composition, the metastable β phase can decompose on cooling to mixtures of α and β, to martensite or to a metastable transition phase. Microstructures can therefore be adjusted by alloying as well as by heat treatment and processing.

The α alloy contains α grains having a lenticular morphology that form on cooling from the β phase region. The transformation from body-centered-cubic β phase to hexagonal-closed-packed α is controlled by the crystallographic relationship. In general, orientation relationship between α and β phases holds whether α phase forms martensitically or by nucleation and growth. In both cases, the resulting α has an elongated grain structure and the aspect ratio of the α grains can be controlled by adjusting the cooling rate from the β phase field.

The commercially important β alloys are more properly designated "metastable" β alloys because, although they can be quenched from high temperature to retain 100% β phase, they can be aged at intermediate temperatures to precipitate α phase. Since the bcc β phase is more easily worked than hcp α phase, the β alloys are used in applications where cold forming is required. Because these alloys are age-hardenable, they can be used in thick cross-sectional components, such as heavy forgings that can be strengthened through thickness. After forming, aging treatments that precipitate α phase can improve mechanical properties. Depending upon the specific alloying element and its concentration, decomposition of β phase can take several different paths. For instance, despite the fact that rapid cooling may cause martensitic transformation, at slower cooling rates decomposition occurs by nucleation and growth of α phase.

Microstructures of the α+β alloys consist of a mixture of two phases, with volume fractions being a function of alloy composition and thermal treatment. The β phase can be retained below the β/α+β transition temperature because partitioning of the β stabilizing elements during cooling results in continued enrichment of the β phase to the point that the composition lies in the β phase field. Ti6Al4V, the most widely used titanium alloy, is α+β type alloy and show transition properties between α and β alloys. In Figure 2.6 the effect of vanadium addition on the β phase stabilization and cooling diagram of Ti6Al4V between β and α+β phase regions are given.

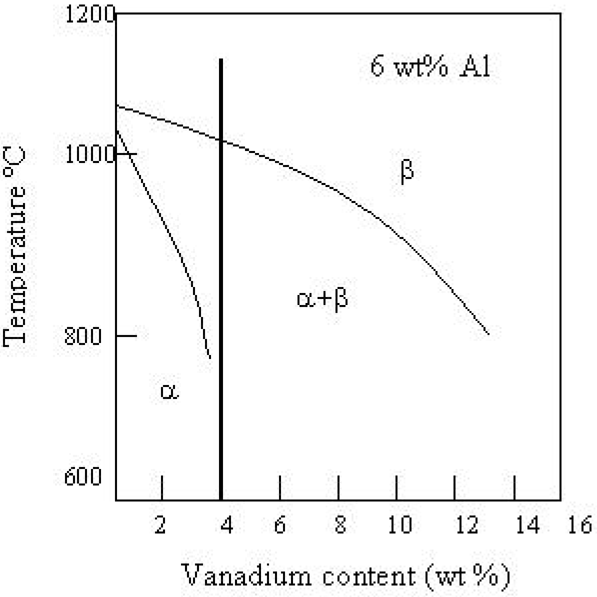

Figure 2.6 Phase diagram of Ti6Al4V.

The heat treatment of α+β alloys typically results in two main microstructures. The first consists solely of Widmanstätten precipitates of the hexagonal close packed α phase distributed in a matrix of body centered cubic β phase, often referred to as the β processed microstructure. Example of a Widmanstätten structure in Ti-6Al-2Sn-4Zr-2Mo alloy is shown in Figure 2.7 [9]. It is also reported that such microstructures result from thermo-mechanical processing of the alloy above the β-transition temperature.

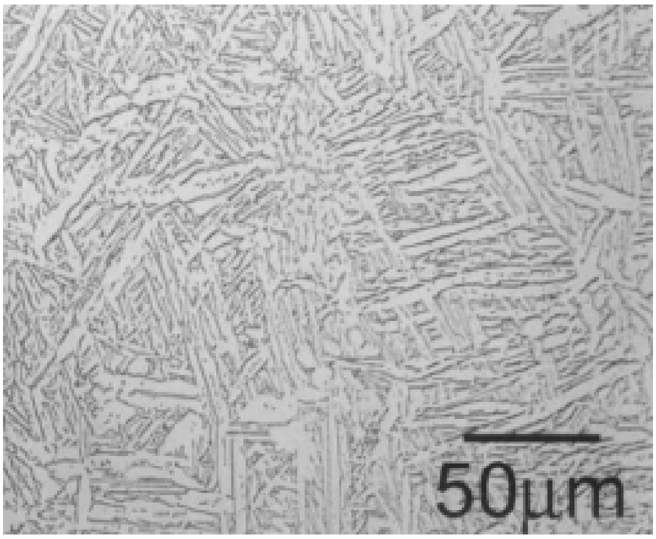

Figure 2.7 Widmanstätten microstructure.

The second type consists of a combination of equiaxed α grains dispersed in a transformed β matrix, often referred to as the α/β processed microstructure. The transformed β matrix, in turn, consists of fine scale Widmanstätten α platelets separated by β laths**.** Such microstructures result from thermo-mechanical processing of the alloy below the β-transition temperature and known as bimodal microstructure (Figure 2.8). The condition has also been termed as ‘‘solution treated and overaged’’ (STOA) [10].

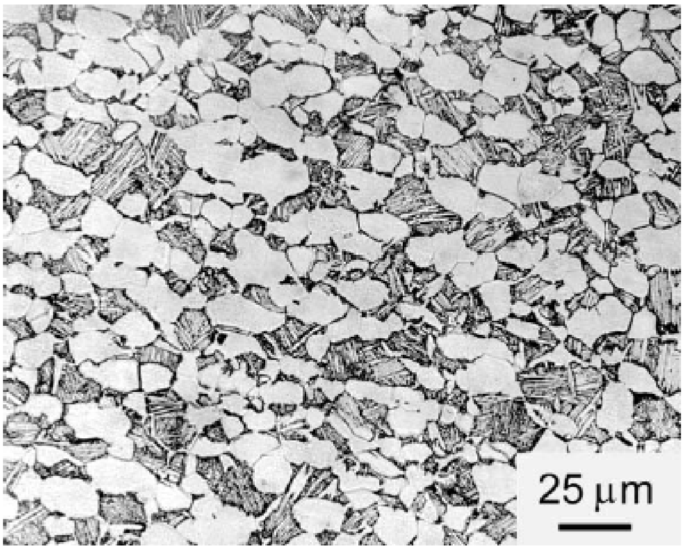

Figure 2.8 Ti6Al4V bimodal structure (equiaxed α+transformed β).

The mechanical properties of titanium alloys not only depend on the chemistry but also is strongly influenced by their microstructure. In Table 2.2 the strength and fracture toughness of equiaxed and Widmanstätten Ti alloys are tabulated [11]. As noted in this table, the yield strength of the alloy is higher in equiaxed microstructure than that of Widmanstätten. However the greatest effect of microstructure is observed on the other properties such as fracture toughness and high temperature flow characteristics. High fracture toughness is associated with the α phase having a high aspect ratio (Widmanstätten) while lower fracture toughness values correspond to the α phase with a low aspect ratio (equiaxed).

Table 2.2 Effect of microstructure on mechanical properties of Ti alloys.

Titanium Alloy Selected	**α Phase Morphology**	**Yield Strength (MPa)**	**Fracture Toughness (MPa.m$^{1/2)}$**
Ti6Al4V	Equiaxed	910	44-66
	Widmanstätten	875	88-110
Ti6Al4V2Sn	Equiaxed	1085	33-55
	Widmanstätten	980	55-77
Ti6Al4V2Sn4Zr6Mo	Equiaxed	1155	22-23
	Widmanstätten	1120	33-55

The increase of fracture toughness in Widmanstätten microstructure stems from longer propagation path of crack. In Widmanstätten microstructure elongated α platelets behave as obstacles for rapid crack propagation and crack propagates at weaker α-β interfaces and intergranular failure occurs. Consequently relatively long crack path increases fracture toughness in Widmanstätten microstructure while crack can propagate rapidly through interior of grains in microstructure. Therefore, more brittle granular fracture is dominant failure type in equiaxed structures.

Although different standards have been developed for characterizing microstructures, the quantification of microstructural features in α/β Ti alloys is very difficult. This is primarily due to the fact that the microstructure is quite complex and involves features spanning a wide range of size scales. If the case of β processed microstructures is considered, Widmanstätten Ti6Al4V microstructure can exist in different forms as shown in Figures 2.9 (a-c). The martensitic structure shown in Figure 2.9 (a) was due to water quenching after β annealing at 1040 °C. The microstructure in Figure 2.10 (b) was achieved via a post-rolling heat treatment of 1065 °C/15 min + 940 °C/5 min + 815 °C/15 min and then air cooling to room temperature. The microstructure in Figure 2.9 (c), Widmanstätten, was obtained after a heat treatment of 1040 °C/1 h + furnace cool to room temperature +970°C/4 h + furnace cool to room temperature.

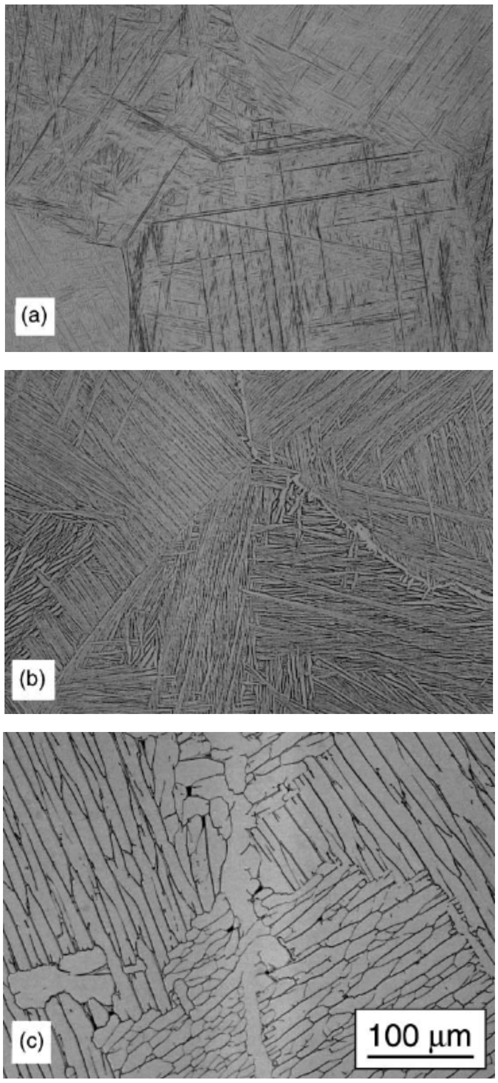

Figure 2.9 Ti6Al4V Widmanstätten structure annealed over β transition temperature. (a) 1040 °C water quenched (b) air cooled and (c) furnace cooled [12].

Ti and its alloys fail by shear banding under compressive forces. This is an important deformation mode generally observed in ballistic impact, explosive fragmentation, machining, grinding, forging and high velocity of fabrication [13]. An example of the shear band formation is shown in Figure 2.10, which was formed in orthogonal cutting of Ti6Al4V [14]. During shear banding, deformation is localized through a region and further deformation occurs in the localized region leading to the failure of the sample. In compression, shear banding forms at 45^{o} to the loading axis as shown for a Ti6Al4V cylindrical sample tested under compression in Figure 2.11.

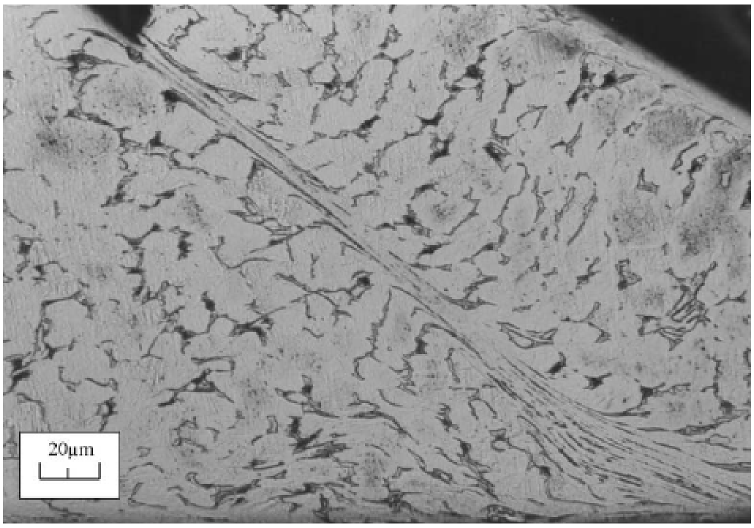

Figure 2.10 Adiabatic shear band formation in a chip of Ti6Al4V [14].

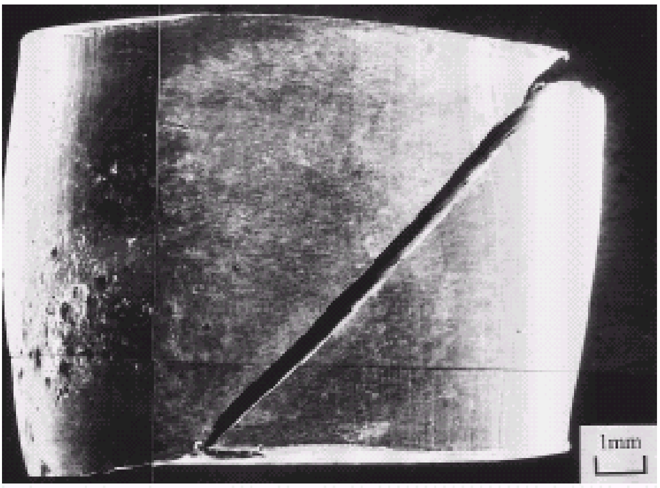

Figure 2.11 Failure of Ti6Al4V via shear banding [15].

The localization of plastic flow in shear bands leading to fracture of a material is usually attributed to the plastic instability resulting from thermal instability. Especially, when one examines the width of a shear band, the effect of thermal diffusion must be taken into account and cannot be treated as adiabatic. However this instability can occur when the local rate of heat generation due to plastic flow exceeds the rate of heat dissipation to the surrounding material. Hence generally mechanism is called as adiabatic shear banding [13]. It has been reported that the localization occurs more easily in materials with low strain hardening rate, low strain rate sensitivity, low thermal conductivity and high thermal softening rate. Perhaps, Ti and its alloys are the metals which are most sensitive to adiabatic shear localization, because Ti alloys possess the properties of high strength and low thermal conductivity, about one order of magnitude less than steel. It is generally agreed that adiabatic shear bands are triggered by a local inhomogeneity such as geometric or dimensional variations, temperature differences and perhaps the presence of voids or inclusions in the microstructure of the material within the shear band was higher than that of the surrounding.

Shear localization proceeds through inclusions such as voids and cracks. The nucleation of micro-voids is considered as a result of the tensile stress inside shear bands as shown in Figure 2.12. Void evolution is comprised of three main stages: nucleation, growth, and coalescence. Figure 2.13 (a) shows nucleation stage of voids within shear bands. These voids nucleate completely inside the band and are surrounded by the flow of localized deformation. They grow up with the localization progress in the growth stage. Most of voids first grow to the width of the band and then are elongated to elliptical shape along the direction of the shear band (Figure 2.13 (b)). Several voids are elongated to ellipse shape and rotated along direction of shear moment in Figure 2.13 (c). The third stage of void development is coalescence of voids and crack generation. Figure 2.13 (d) shows the whole process of void coalescence.

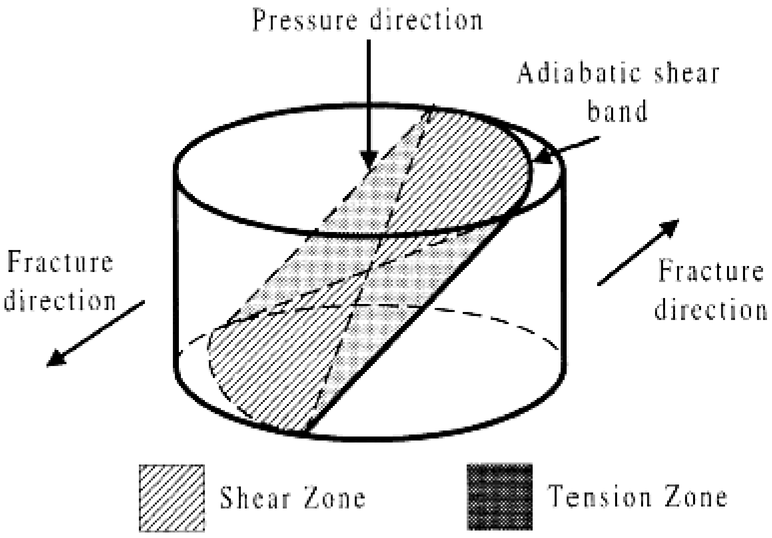

Figure 2.12 Schematic illustration of shear banding failure [15].

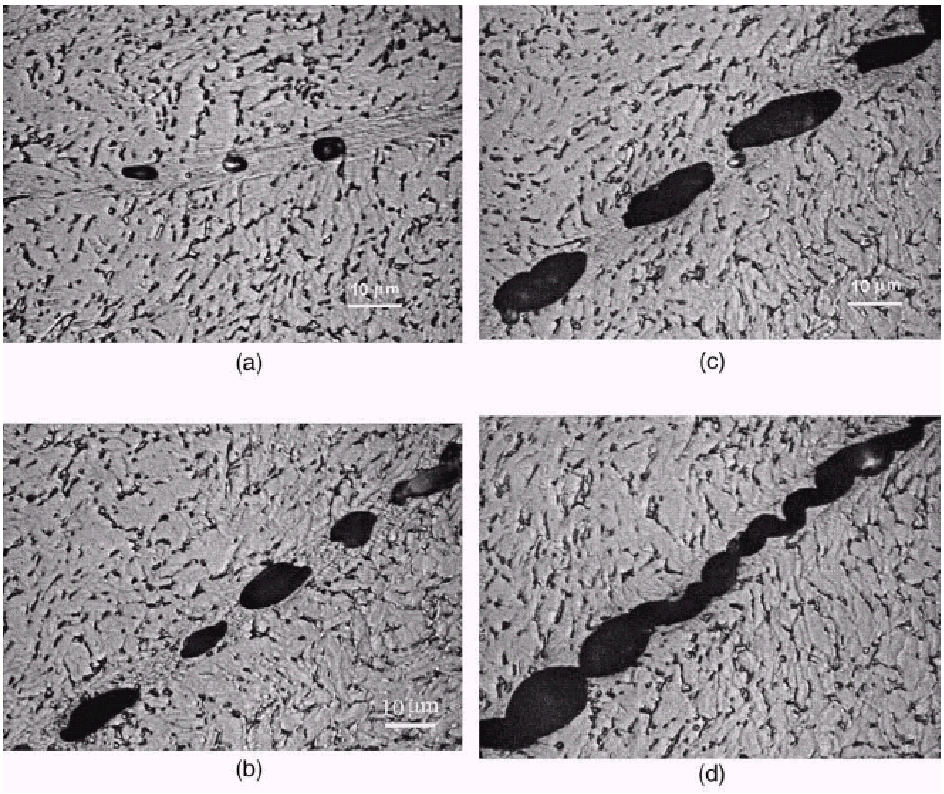

Figure 2.13 Nucleation, growth and coalescence of void on the shear band [16].

2.6 Disadvantages of Classical Implants Used in Orthopedic Applications

2.6.1 Interfacial Bonding

Loosening mechanism is one of the biggest problems occurring due to weak interfacial bonding and affects the implant life substantially in vivo. Long-term experience indicates that insufficient load transfer from the artificial implant to the adjacent bone may result in loosening of the prosthetic device [3]. Recent studies reported that 10–20% of joints need to be replaced within 15–20 years and that loosening accounts for approximately 80% of these revisions [17]. The results are considerably worse in young adults and the middle aged people. This complication results in significant problems and requires re-operation and revision of the joint replacement. Main reason for loosening of an implant is weak bonding between the implant and the bone causing insufficient load transfer. For metallic implants, one way to increase bonding of an implant and a bone is coating of an active material onto the surface of metallic implant [18]. Another way to improve bone bonding ability of the implant is producing metallic implant with porous structure. Previous studies have shown that porous biocompatible implants provide bone cell ingrowth and cause stronger implant bonding. Therefore, these structures have the capability of prevention of loosening mechanism when used as an implant [6]. Porous implants or metallic bulk implants with porous coating structure have given good clinical results by means of their good fixation by bone ingrowth (osteo-integration) into a three dimensional matrix of interconnected porosity [19].

2.6.2 Elastic Mismatch of Implants and Natural Tissues

Another problem for biomedical metallic implants is known as elastic mismatch. It has been shown that when the tension/compression load or bending moment transmitted to living bone is reduced, consequently, decreased bone thickness, bone mass loss, and increased osteoporosis ensue. This phenomenon, termed ‘stress shielding’, has been related to the difference in flexibility or stiffness between natural bone and the implant material [20]. Unfortunately, classical metallic implant materials have much higher elastic modulus values than that of natural bone. For example the elastic modulus of pure titanium is 110 GPa while natural bone has that of only 1-20 GPa [21]. Any reduction in the stiffness of the implant, for example, through substitution of present orthopedic alloys with newer, lower modulus materials, is expected to enhance stress redistribution to the adjacent bone tissues, therefore minimizing stress shielding and eventually increasing device lifetime.

The problems related to the elastic mismatch of bone and implant have resulted in a number of proposed solutions like more flexible designs and the use of materials with low elastic modulus. A first attempt at reducing the elastic modulus of orthopedic alloys was made by the introduction of α+β titanium alloys having elastic modulus values approximately half of that of stainless steels or CoCrMo alloys. Table 2.3 shows the differences of elastic modulus (E), yield strength (σ_y) and ultimate tensile strength (UTS) properties between various metals and natural bone. However, the modulus of Ti6Al4V and related α+β alloys is still high (110 GPa), approximately 5–10 times that of bone. Recent attempts at further minimizing moduli of orthopedic alloys have led to the introduction of metastable β titanium alloys, Ti15Mo5Zr3Al, Ti12Mo6Zr2Fe, Ti15Mo3Nb0.3O and Ti13Nb13Zr, having minimum elastic modulus values ranging from 74 to 88 GPa. The elastic modulus values of these second generation β alloys are still 2–7 times higher than elastic modulus of the bone. Finally, TiNbZrTa (TNZT) alloys having minimum modulus has recently been demonstrated [3]. These alloys exhibit moduli 20–25% lower than other available alloys (Table 2.3).

Table 2.3 Mechanical properties of several materials.

Material	Elastic Modulus (GPa)	Yield strength (GPa)	UTS (GPa)
Pure Ti	105	692	785
Ti-6Al-4V	110	850-900	960-970
Ti-13Nb-13Zr	79	900	1030
Co-Cr-Mo	200-230	275-1585	600-1795
Stainless Steel	200	170-750	465-950
Bone	1-20	-	150-400

Elastic mismatch of metallic implant materials and natural bone is still a big problem for orthopedic applications whether they are pure metal or alloy. New trends in this field are on production of porous structures, whose elastic modulus can be tailored by altering the porosity level. Guden et al. [22] have recently predicted the porosity level of Ti foams which has elastic modulus comparable with cancellous bone as shown in Figure 2.14.

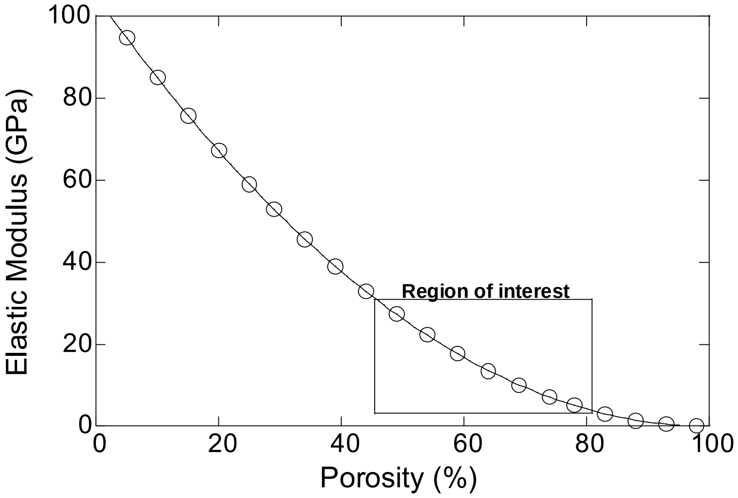

Figure 2.14 Variation of elastic modulus of pure Ti foam as function of porosity [22].

Chapter 3

NATURAL BONE

Bone is described as a connective tissue, helping to support and bind together various parts of the body. It is a composite material consisting of both fluid and solid phases. Bone has hard structure because the organic cellular collagen matrix is impregnated with inorganic materials, principally hydroxyapatite $Ca_{10}(PO_4)_6(OH)_2$. Calcium and phosphate account for roughly 65 to 70 % of the bone's dry weight. The organic material, collagen, gives bone flexibility while the inorganic material gives bone its resilience. Bone is the principal reservoir of several minerals that the body uses like calcium, phosphorous, sodium, magnesium and carbonate, and cortical bone, contains about 70% of these minerals as well as providing the body with structural strength and internal organ protection.

Bone is identified as either cancellous (also referred to as trabecular or spongy) or cortical (also referred to as compact). Cortical bone represents approximately 4 times the weight of cancellous bone in any long bone. The basic material comprising cancellous and cortical bone appear identical, thus the distinction between the two is the degree of porosity and the organization. The porosity of cortical bone ranges from 5% to 30 % (mostly in the range 5%-10%) while cancellous bone porosity ranges from 30% to 90 % (mostly in the range 75%-95%). Bone porosity is not fixed and can change in response to altered loading, disease, and aging.

3.1 Types of Bone

3.1.1 Cortical Bone

Cortical bone represents nearly 80% of the skeletal mass. It is also called compact bone, because it forms a protective outer shell around every bone in the body. It consists of repeating units called Haversian systems (Figure 3.1). Haversian systems or osteons have concentric layers of the mineralized collagen fibers called lamellae, which are deposited around a central canal called Haversian canal, containing blood vessels and nerves that service the bone. The osteons are cylindrical at about 200-250 µm in diameter running roughly parallel to the centerline axis of the bone. Cortical bone is semi-brittle, viscoelastic and anisotropic material, and these material properties are influenced by porosity, mineralization level and the organization of the solid matrix.

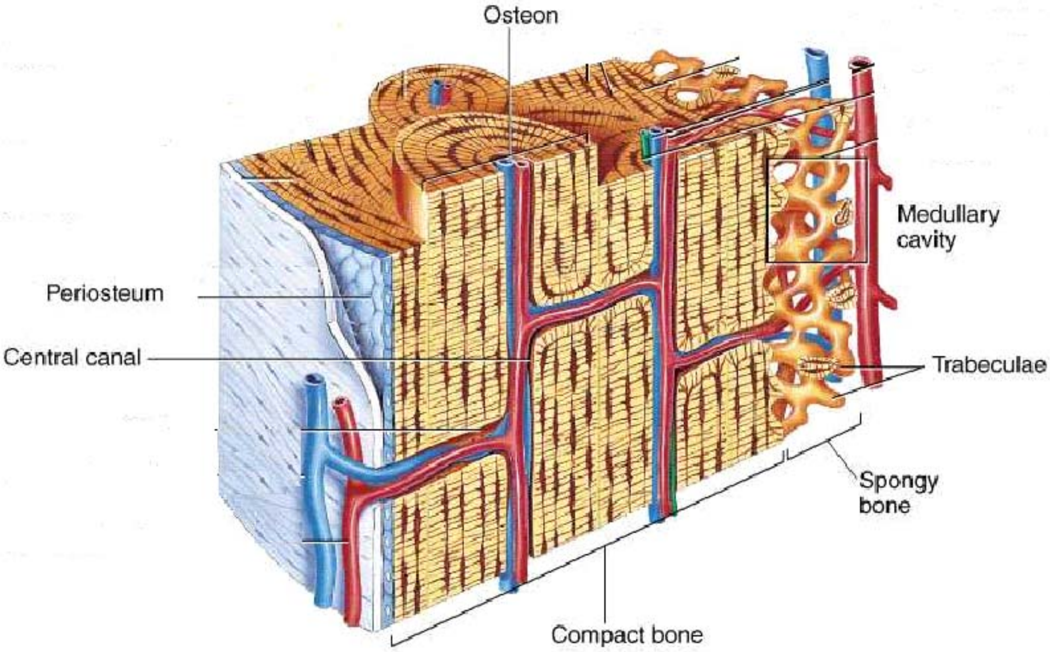

Figure 3.1 Haversian systems (osteons) in cortical and cancellous bone.

3.1.2 Cancellous Bone

Cancellous bone is usually found in the interior of the bones (Figure 3.1). This bone represents only 20% of the skeletal mass, but 80% of the bone surface. Cancellous bone constitutes most of the bone tissue of the axial skeleton such as bones of the skull, ribs and spine. It is formed in an intricate and structural mesh. The porous lamellar matrix in cancellous bone is formed into plates or struts having an approximate thickness of 100 µm. The cancellous bone does not have Haversian canals as the structures are too thin to contain osteons. The porous structure of cancellous bone consists of network of marrow filled voids surrounding the trabeculae.

Cancellous bone is active metabolically and is remodeled more often than cortical bone, therefore the mechanical properties of the bone change with age.

3.2 Characterization of Bone

The mechanical properties of bone and other biological tissues depend on many parameters such as test direction and the freshness of the tissue. The properties of bone can change significantly if allowed to dry out. Thus, it is very important to keep bone specimens wet during testing. The material properties of bone are generally determined using destructive testing. However ultrasonic techniques have also been employed. Mechanical testing consists of applying tensile, compressive, torsional, or shear loads to bone specimens and recording the deformation of the material. Application of different load types is important since bones undergo different types of loading in vivo. Mechanical testing of bone is really complicated because of the anisotropy (requires multiple samples for testing) and the small sample sizes that are obtainable. For these reasons efforts have been made to use ultrasonic techniques. These techniques make use of the relations between the speed of sound and the elastic properties of the material. Ultrasound requires fewer and smaller specimens to characterize the material properties of bone. The disadvantage is that the relationship between the speed of sound and the tissue's elastic properties must be known.

From the mechanical point of view, cortical bone can be understood as a composite material consisting of at least three phases: the mineralized matrix, the collagen fiber network, and the fluid-filled pore phase.

3.3 Mechanical Properties of Bone

Mechanical properties of the cortical and cancellous bone are very different. Cortical bone is stiffer than cancellous bone and can sustain greater stress but less strain before failure. Cancellous bone can sustain strains of 75 % before failing in-vivo, but cortical bone will fracture if the strain exceeds 2%. Cancellous bone has a greater capacity to store energy compared to cortical bone. It should be stated that the volume fraction of calcium is the dominant factor in determining the mechanical properties; the higher the volume fraction of calcium the higher the stiffness and strength and the lower the toughness [23].

The strength and fracture toughness of bone are also time dependent and biological aging and strain rate effect are two major mechanisms in this concern [24].

(i) *Biological aging*. The strength and the modulus of elasticity of bone are affected by aging and decrease after maturation. Moreover, children's bones tend to absorb more energy before failure as compared to adults. Children's bones are weaker, but more compliant.

(ii) Strain rate effect. Ultimate strength and the modulus of elasticity of cortical bone increase with increasing loading or strain rate whereas the ultimate strain decreases. Bone is strain rate sensitive material and tends to be more strain rate sensitive than other biological tissues. At low strain rate, bone behaves like a viscous material. Also, the fracture toughness shows strong strain rate dependence.

Biological materials differ in one respect from other structural materials under repeated loading and unloading. They possess repair mechanisms. Under normal conditions cycling loading of a biomaterial will cause microdamage. However, damage accumulation will not occur in the case when the repair mechanism is active in a timely fashion. The repair activity can be slowed down for various reasons. Naturally there are age-related changes manifesting as a decrease of bone mineral density. Normal repair can also be impaired by metabolic diseases (e.g., osteoporosis) or by certain drugs. Furthermore, repeated loading without sufficient time for repair activity causes fatigue failure.

Three important parameters that characterize some of the mechanical properties of bone are ultimate force, maximum deformation to failure, and energy that it can store before failure. These properties can be obtained from a force-deformation curve. The ultimate force represents the maximum load that the bone can sustain before it breaks. The ultimate force varies depending on the type of load applied (e.g. tensile, compressive, shear) and the loading rate. The energy absorbed before failure can be calculated from the area under the force-deformation curve and therefore depends on both the ultimate force and the ultimate strain.

3.4 Replacement of Bone

Bone tissue replacement is an essential phenomenon for biomedical application field. Many operations involve bone repair for replacement surgery, disease, trauma, abnormal development or skeletal deficiency. The traditional approaches to bone grafting include utilization of autograft and allograft. Autograft is bone graft that serves as a source of osteogenesis and mechanical support. Allogfaft is also tissues that are routinely transplanted from one human to another. However, they impose several limitations such as donor site morbidity, infection, pain, genetic differences, limited donor bone supply, anatomical and structural problems, loss of bone inductive factors and high levels of resorption during healing. This situation presents significant economical implications for healthcare providers. Therefore, the use of artificial bone implants for stabilization of fractured bones has gained more interest, recently.

Artificial scaffolds are examples of this new trend implants and directly affect the formation of bone tissue. Hence, this scaffold should meet some requirements for the regeneration of bones. The major chemical requirement for the scaffold is its biocompatibility, the absence of any inflammatory response or toxicity upon implantation of scaffold. In addition to biocompatibility, the scaffold should support growth of bone cells into a three dimensional structure to form bone. Surface energy may play a role in interaction of proteins with the surface of the material thus affecting the affinity of the cells to the material. Particle size, shape and surface roughness also influence cellular adhesion and proliferation. The macrostructure of the scaffold should mimic the physiological functions of the native extra cellular matrix for cells so that they differentiate and proliferate properly. Interconnected porous structure is required to provide necessary space for cell ingrowth and vascularization. The optimum pore size varies from 200 to 500 μm depending on the tissue to be replaced [5]. The interconnective structure should allow uniform cell distribution, cell survival proliferation and migration. In particular it should allow free passage of body fluids, nutrients and gases to the cells and removal of metabolic waste and by products from cells. High internal surface area to volume ratio is essential to accommodate a large number of cells.

Scaffolds should possess a high mechanical strength until the new tissue is formed completely in addition to its macrostructure and biocompatibility properties. They should be strong enough to tolerate any in vivo stresses and physiological loadings that are imposed on them. The implants should also be supplied at any time and in any quantity. It is difficult to define standards for tissue engineering scaffolds due to the diverse characteristics such as pore size, total porosity, pore shape, pore interconnectivity, material surface chemistry, effective scaffold permeability and scaffold’s stiffness that can affect bone regeneration.

Chapter 4

PROCESSING AND CHARACTERIZATION OF POROUS METALS

4.1 Production Techniques for Open and Closed Cell Foam Metals

There are quite many routes for the manufacturing of cellular metallic materials. Some are similar to techniques used for foaming aqueous or polymer liquids, whereas others are specially designed by taking advantage of characteristic properties of metals such as their sintering activity. The various methods can be classified according to initial state of the metal for the process. By this explanation, metal foam production methods can be classified into two groups: Foaming from liquid metal and solid metal in the powder form.

4.1.1 Liquid State Processing of Cellular Metals

The molten metal can be processed into a porous material either by foaming it directly, using an indirect method via a polymer foam originally and by casting the liquid metal around solid space holding filler material which reserve space for what after further processing becomes the pore space. Although, melting methods have been successfully applied to the manufacture of Al, Zn and Mg foams, they are not suitable for the manufacture of Ti foams due to high melting temperature and reactivity of Ti. Main liquid foaming processes are Cymat/Hydro, Alporas and investment casting with a cellular polymer.

The Cymat/Hydro metallic foam casting process shown in Figure 4.1 is a continuous method and named after developer companies. Method was originally developed by Alcan and now licensed by Cymat Aluminum Corporation. A similar process is employed by Hydro Aluminum, Norway. Aluminum-SiC or Aluminum-Alumina metal matrix composites are used as starting materials [25].

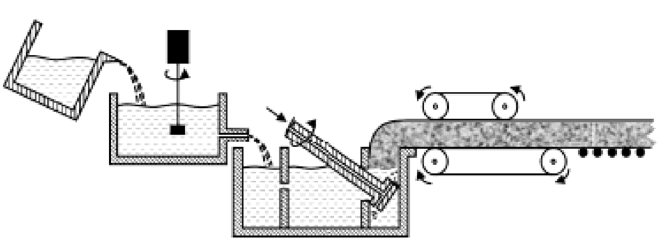

Figure 4.1 Cymat/Hydro processing method.

The starting material is melted with conventional equipment and transferred to a department where gas (typically air) is introduced. The resulting liquid metal foam is removed by means of a conveyor belt. The average cell size is related to the density and ranges between 2.5 and 3 mm. Cymat's production line is capable of continuous casting of foam panels at an average rate of 900 kg/h [25].

The manufacturing process of the ALPORAS foam is a batch casting process. For stabilizing the bubbles in the molten aluminum 1.5% Ca is added at 680 °C and stirred for 6 min in an ambient atmosphere. The high oxygen affinity of the Ca leads to the quick formation of oxides. The thickened aluminum is poured into a casting mold and stirred with an admixture of 1.6% TiH_2 as a blowing agent. After stirring the molten material expands and fills up the mold [26].

Foam can also be manufactured by investment casting using a polymer foam precursor. The polymer foam with open cell is then filled with a slurry of sufficiently heat resistant material, e.g. a mixture of mullite, phenolic resin and calcium carbonate or simple plaster. After curing, the polymer foam is removed by thermal treatment and molten metal is cast into the resulting open voids which replicate the original polymer foam structure. Application of pressure and heating of the mould may be necessary if no filling of the narrow cavities with the liquid metal can be achieved in simple gravity casting. After removal of the mould material, a metallic structure is obtained which is an exact replicate of the original polymer foam. This method is also known as “duocel” since its trademark company in Japan. Complex shaped parts can be fabricated by pre-forming the polymer foam. Duocel aluminum foam has porosities typically range from 80 to 97% and a cell density of 2-20 pores per centimeter, with material density and cell size independently variable [26].

4.1.2 Solid State Processing of Cellular Metals

Instead of a molten metal, solid metal in powder form is used to produce cellular metallic structures. The powder remains solid during the entire process and goes through a sintering treatment or other solid state operations. This is crucial for the morphology of the resulting cellular structure because surface tension in liquid state can form closed pores whereas final product after sintering has open cell characteristic. Alulight foaminal, hollow spheres and space-holder technique are common solid state foaming methods.

In the production of Alulight-Foaminal technique, metal powders are mixed with a foaming agent and compacted to yield a dense semi finished product. Compaction methods, uniaxial compression, extrusion or powder rolling, are used to produce dense foamable material. During heating, the foaming agent decomposes and the released gas forces the material to expand. Prior to foaming, the precursor material can be processed into sheets, rods, profiles, etc. by conventional techniques. Near-net shaped parts are prepared by inserting the precursor material into a mold and expanding it by heating [25]. By injecting the expanding foam into molds quite complicated parts can be manufactured. Sandwich panels consisting of a foamed metal core and fully dense face sheets can be obtained by gluing the face sheets to a sheet of foam.

In hollow sphere foam production method, closed cell foam structures can be obtained by filling the interstices between the spheres with metal powder followed by a sintering treatment. Thin walled spheres are sufficient in this case. One of the advantages of hollow sphere structures is that the pore size distribution of the foams is not random and it can be tailored by a proper selection of the hollow spheres. The mechanical and other physical properties of hollow sphere structures are therefore more predictable than the properties of foams with a random pore size. A further advantage is that, in principle, the full range of materials available in powder metallurgy can be used for the process, such as superalloys, titanium and titanium alloy. Hollow sphere structures can therefore be used in high temperature applications. But, the production is not economical and cost is the biggest problem for this foaming technique [25].

4.1.2.1 Space Holder Method

Since the methods of Alulight foaminal and hollow sphere sintering unavoidably result in enclosed pores (closed cell foam), they are also not suitable for the manufacture of foamed metal implants because of the requirement of body fluid transport. Open cellular metallic implants can be however successfully manufactured by a versatile powder metallurgy (PM) based process known as space holder method. The method can be used to manufacture fully and/or partially (as coatings on solid implants for bone fixation) porous biomedical metals. The size, level and geometry of pores can be easily altered by varying the size, amount and shape of space holder. Therefore, it is one of the appropriate methods for manufacturing designed porous metallic implants. Space holder method consists of mixing, compaction, space holder removal and sintering steps. These steps of the process are illustrated in Figure 4.2.

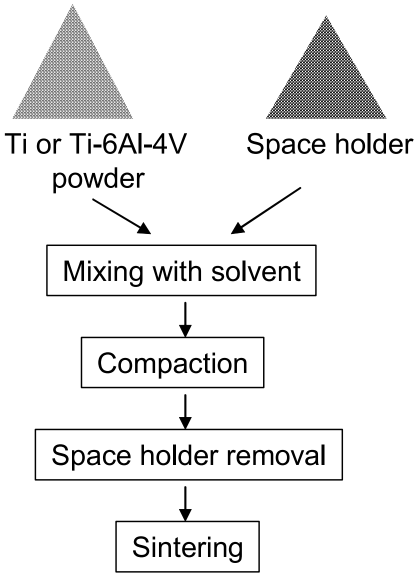

Figure 4.2 Steps of production in space holder method.

The metal powder is either filled into a dry bulk of fillers, or a suitable solvent. Ceramic particles or hollow spheres, polymer grains or hollow polymer spheres, salts or even metals can be used as space holders [25]. The filled bulk is then either simply compacted at room temperature or at elevated temperatures to improve compaction. Therefore, a composite is obtained which consists of a metal matrix with embedded filler granules. If the metal content is sufficiently low, it is possible to remove the space holder material almost completely in a further process step because the network formed by the filler material is interconnected. This can be done by thermal treatment, leaching, or by use of an aqueous solvent. A final sintering step can be applied to increase density of the porous metallic network. Copper, nickel, steel or titanium powders can be used to create highly porous structures by bonding the individual powders together by sintering. Open structures are obtained by creating sintering necks between adjacent metal particles during sintering. By applying forces during sintering the powders may be deformed leading to an increase of sintering contacts but also to a reduction of the degree of open porosity.

Open cell porous Ti structures potentially to be used in biomedical applications were previously prepared using space holder method [4, 5]. The method allows a direct near net-shape fabrication of foamed implant components having elastic modulus comparable with that of natural bone and with a relatively homogeneous pore structure and a high level of porosity (60-80%). Bram et al. [4] investigated the preparation of highly porous titanium using carbamide (urea) and ammonium hydrogen carbonate as a space holder. The porosities varied between 60 and 80 %. The pores were spherical and angular within the range of 0.1-2.5 mm depending on the shape and size distribution of the space holder used. Wen and co-workers [5] also produced open cell Ti foams using the same method. It was shown that porous titanium produced consisted two types of pores; macro-pores (Figure 4.4(a)) with the size of 200-500 μm fabricated to provide bone ingrowth and transportation of body fluids and micro-pores (Figure 4.4(b)) resulted from volume shrinkages during sintering particles which was also reported as preferable in osteoinductivity [5].

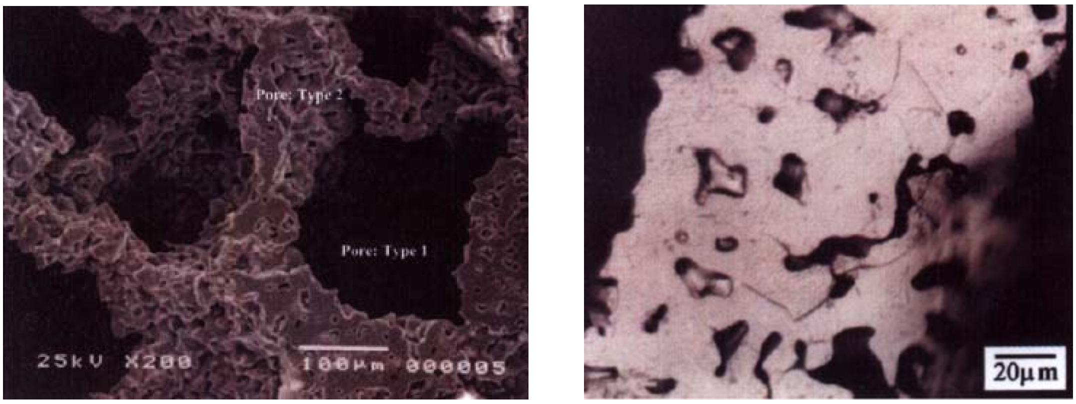

Figure 4.3 SEM micrograph of porous foam [5].

Nominal stress-strain curves of Ti foams with 80% porosity were also shown to be very similar to universal metallic foam characteristic which starts with elastic deformation and followed by plateau stress region and finally densification of the foam at the strain of 62%. The change of elastic modulus of porous Ti via porosity was also given in Figure 4.5 (b). The plateau stress and elastic modulus of the foams with 80% porosity were reported as 40 MPa and 2.87 GPa respectively [5]. Although the compression strength of the foams (40 MPa) was sufficient for cancellous bone replacement, it was quite low for cortical bone replacement.

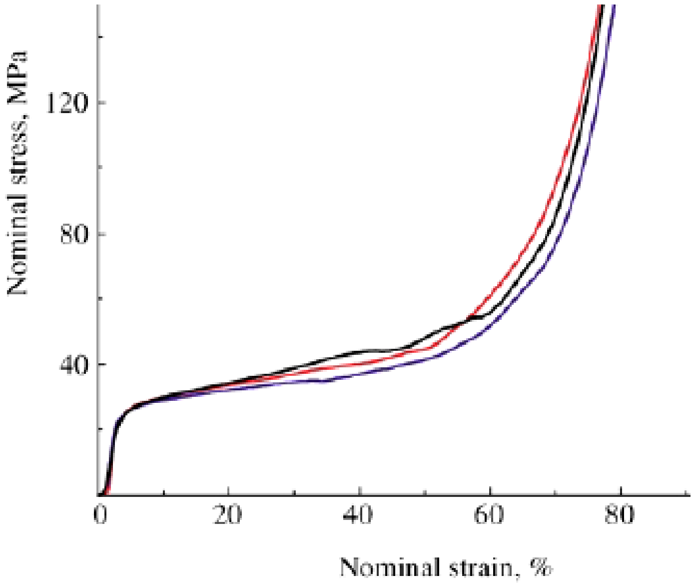

(a)

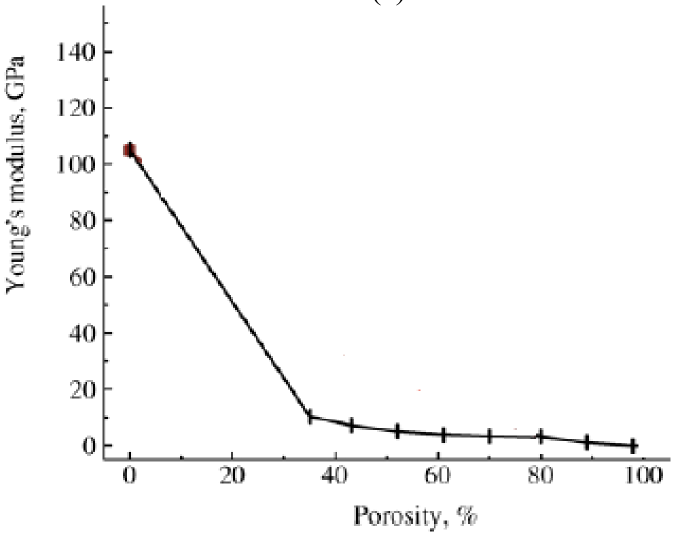

(b)

Figure 4.4 Mechanical properties of titanium foam (a) Nominal stress-strain curves of foam with 80% porosity (b) Change of young modulus via porosity [5].

4.2 Characterization

Cellular metals and alloys can be characterized in many ways. The objective is either to obtain mechanical or physical data characteristic of the cellular material investigated or to carry out a technological characterization of a component containing cellular metal. Cellular material is a construction consisting of a multitude of struts, membranes or other elements which themselves have the mechanical properties of some bulk metal. Testing a cellular material is therefore equivalent to testing any engineering component. Hence, a cellular structure can be considered as a homogeneous medium which is represented by averaged material parameters.

The overall density of a porous material can be determined by weighing it and by measuring its volume using Archimedes' principle. According to this principle liquid should not be penetrated into pores of metal. If the sample to be characterized does not have a closed outer skin, penetration of liquid into the pores has to be prevented by coating its surface with a polymer or paraffin film.

The liquid processing methods yield cellular materials with closed cells or even a closed outer skin. However, in practice imperfections occur while making the foams such as in the cooling stage after processing. Such imperfections can include little holes or cracks in the cell walls or in their outer skin. Penetration techniques are ideal for detecting such surface defects. In this technique, a liquid chemical is firstly applied to the cellular metal to be investigated. The chemical is eventually absorbed by the holes and cracks. After drying the surface, a coloring developer is applied which creates color where the penetrant chemical has been retained. In this way, maps of the imperfections can be obtained in a simple visual manner.

4.2.1 Optical Image Analysis

The cell morphology and microstructure of cellular metals can be analyzed by microscopy observations at various magnifications. Although the actual analysis is nondestructive, sample preparation usually requires cutting, embedding or polishing of the materials and is therefore effectively a destructive technique. Optical image analysis programs help to investigate structure photographs of cellular materials taken by optical or electron microscopes.

Cell or pore size distributions can be determined or a shape analysis of the cells can be performed by using commercial image analysis programs. A very careful preparation of the materials is required to obtain reasonable analysis results. In optical image analysis, cell membranes and the interior of the cells must appear in different brightness. One way is to embed the cellular material in a black resin and to polish the preparation plane. This process which is treated to obtain more contrast between pores and cell walls is given in Figure 4.3.

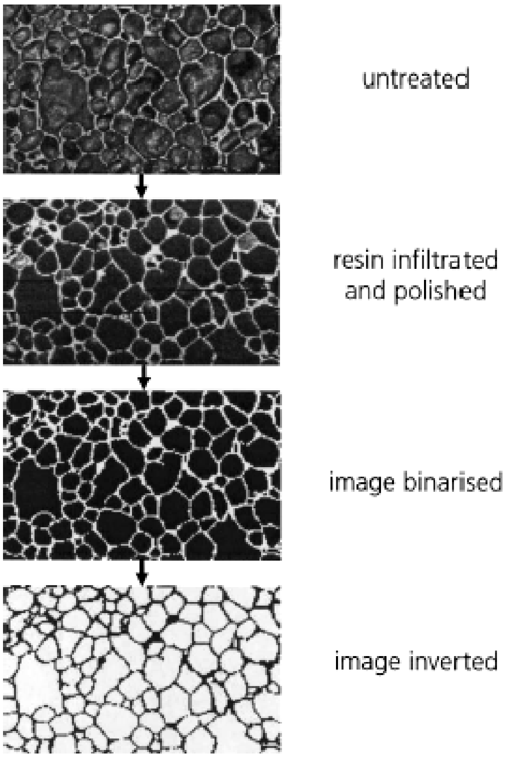

Figure 4.5 Sample preparation in image analysis.

4.2.2 Mechanical Testing

Mechanical testing of cellular metals is essential for any structural application. Mechanical characterization methods for cellular materials are, in principle, the same as for other non-cellular materials. However, some modifications of the test procedures are necessary to account for the specific nature of cellular materials sometimes. Statistics is one specific feature of these materials. If a cellular metal of a given alloy is tested, the resulting mechanical properties of a number of samples with the same overall foam density may show a much larger scatter than usually found in testing conventional materials. Some parameters such as mass distribution and heterogeneous microstructure can distinguish various samples of the same overall density from each other. In order to obtain meaningful results and to average out these parameters, a larger number of samples may be necessary compared to what is required by the testing standards for non-cellular materials. Also, as in cellular materials the length scale for macroscopic heterogeneities is sometimes in the range of millimeters, the sample dimensions in mechanical tests might have to be enlarged compared to existing standards.

The various different mechanical tests can be labeled according to applied stress, modes and time dependence of loading features. Type of applied stress can be uniaxial, biaxial, multiaxial and hydrostatic. Uniaxial tests have been the standard in most experimental work on mechanical properties of cellular metals so far.

There are also various modes of loading such as compression, tension, shear, bending and torsion. Compression tests are the most frequently carried out because, simple shaped specimens can be used for the tests and clamping of the sample is not necessary. Tension tests have been performed with both cubic and dogbone-shaped samples. Shear tests require one or two flat sheets of cellular metal attached to two or three steel plates. Bending tests can be carried out in three or four point configuration.

Time dependence of load can be constant, slowly increasing, dynamic and cyclic. Most of the work found in the literature was obtained under quasi-static conditions. High strain rates can be realized in drop weight tests (up to 100 s^{-1}), with a split Hopkinson pressure bar (up to 5.10^3 s^{-1}) or in ballistic tests (up to 10^5 s^{-1}). Fatigue tests are most easily carried out in a compression–compression mode for the same reasons which apply to quasi-static tests, but compression–tension, tension–tension and cyclic bending tests have also been performed by preparing and fixing appropriate samples. Creep tests are carried out under given constant loads. Other mechanical tests include fracture toughness measurements on notched samples and indentation tests with various indentor shapes. For sandwich panels with a cellular core, there are technological tests to describe the bonding between the face sheets and the core, such as the drum peel test (ASTM D1781).

Chapter 5

MATERIALS AND METHODS

5.1 Materials

The sintered powder compacts were prepared using two different Ti6Al4V alloy powders; atomized spherical particles (Powder A) and angular particles (Powder B). Powder A was manufactured by Phelly Materials with atomization process and Powder B was produced by Solea-Sas Company, France via a patented process. The chemical composition of Powder A and Powder B complied with ASTM 1580-1 standard [27] is tabulated in Table 1. Moreover, the chemical composition of Powder A given by producer company is shown in the same table. The particle size of Powder A ranged between 74 and 250 µm with a mean particle size of 140 µm. The particle sizes of Powder B ranged between 40 and 400 µm with a mean particle size of 170 µm. The powders were sieved in the particle size range of <100µm, 100-200 µm and 200-300 µm in order to determine the effect of particle size on the porosity attained in the powder compacts. Mean powder sizes were microscopically measured as 55, 157 and 212 µm for Powder A and 42, 160 and 251 µm for Powder B. The SEM images of powders sieved into 3 three different powder size ranges are shown sequentially in Figures 5.1 and 5.2 for Powder A and Powder B, respectively. As-received Powder A particles are spherical and have nearly uniform particle size while Powder B particles are almost spherical if the particle size is less than 100 µm and in the form of oblate plates if the particle size >100 µm.

Table 5.1 ASTM standard for Ti6Al4V powder and chemical composition of Powder A.

Element	Al	V	O	Fe	C	H	N	Cu	Sn	Ti
ASTM F1580-01	5.5~6.75	3.5~4.5	0.2	0.3	0.08	0.015	0.05	0.1	0.1	Balance
Testing Results	6.38	3.93	0.17	0.27	0.013	0.003	0.0072	0.091	<0.01	Balance

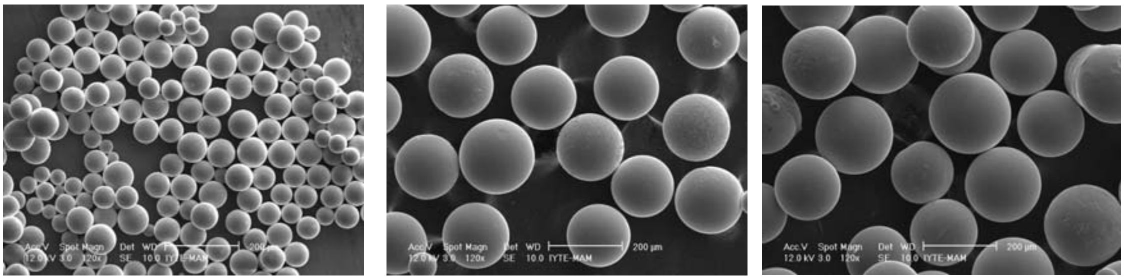

(a) (b) (c)

Figure 5.1 SEM micrographs of Powder A (a) <100 (b) 100-200 (c) 200-300 μm.

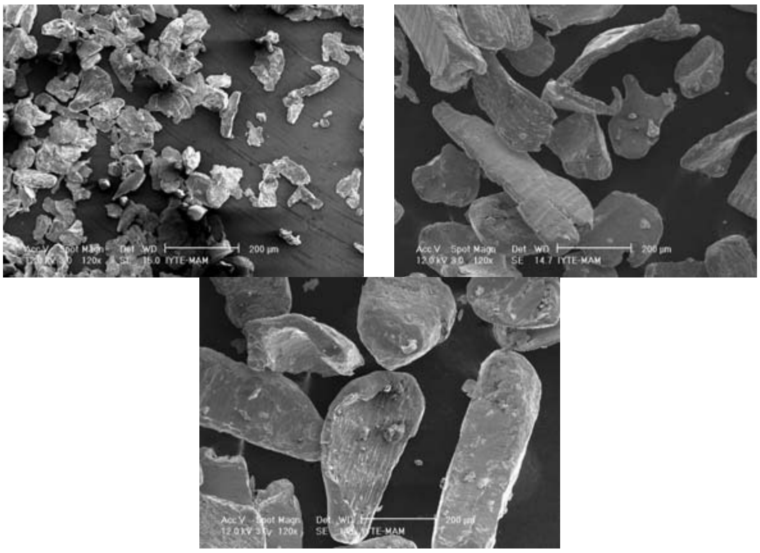

(a) (b) (c)

Figure 5.2 SEM micrographs of B powders (a) <100 (b) 100-200 (c) 200-300 μm.

5.2 Powder compaction

Green powder compacts, 10 mm in length and 16 mm in diameter were compacted at room temperature inside a steel die. It was found that without using a binder Powder A could not be shaped until about the pressures of 400 MPa; therefore, PVA solution 10% by volume was used as the binding material in an amount of 10% by weight. Compaction pressures chosen for Powder A and B were 200, 300, 400 and 500 MPa and 50, 100, 200 and 400 MPa, respectively. At the compaction pressures lower than 200 MPa, Powder A green compacts could not retain shapes after removing from the die and the compaction pressures higher than 400 MPa formed lateral cracks on Powder B compacts. The sintering of green compacts was performed in a tightly enclosed horizontal tube furnace under the high purity (99.998%) Ar atmosphere at 1200 ^{o}C for 2 hours. The sintering temperature and time were chosen based on the previous sintering studies of Ti foam and powder compacts [5-6]. For comparison purposes, relatively dense Powder B compacts (<75μm) compacted at 1000 MPa were sintered at 1350 ^{o}C for 2 hours. The compacts were inserted into the furnace at room temperature inside an enclosed Ti box on a graphite plate which prevented the bonding between Ti box and compacts. The compacts were heated and cooled with a rate of 5 ^{o}C per min. In the heating cycle, the compacts were kept at 450 ^{o}C for ½ hour in order to allow the burning of the binder.

5.3 Compression testing

Quasi-static compression tests were conducted on the cylindrical samples, 15 mm in diameter and 10 mm in length, using a displacement controlled SHIMADZU AG-I universal tension-compression test machine. Eccentric compression test plate was used in all tests in order to prevent shear forces formed by uneven surfaces of the test specimens (Figure 5.3). Tests were performed at a cross-head speed of 2 mm min^{-1} corresponding to a strain rate of 2x10^{-3} s^{-1}, respectively. During compression test, the test plates and surfaces of the samples were lubricated in order to reduce the friction between sample and the test plates. At least three tests were conducted for each set of powder samples. Elastic modulus, yield stress, ultimate compressive stress and failure strain values were determined from the determined stress-strain curves. The measured strain values were corrected with the compliance of the compression test machine.

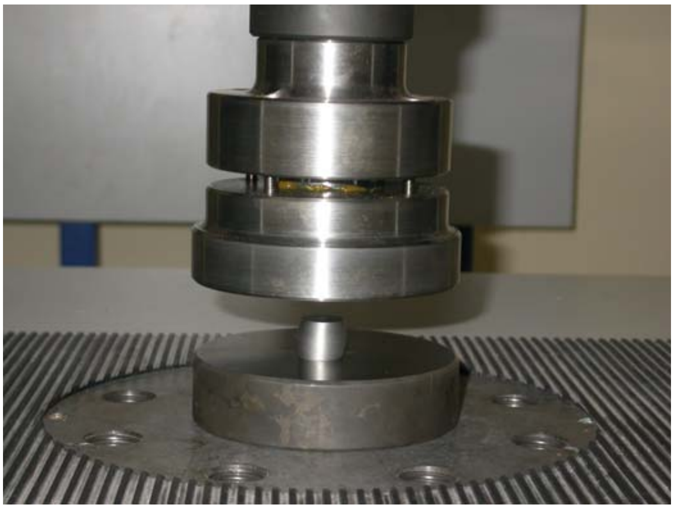

Figure 5.3 Eccentric compression testing apparatus.

High strain rate compression tests were performed on sintered Powder A compacts compacted at 400 MPa using a compression type Split Hopkinson Pressure Bar (SHPB) set-up at 300 and 900 s^{-1} at The University of Delaware. The Split Hopkinson Pressure Bar technique of testing of materials at moderate strain rates (1000's s^{-1}) is a widely accepted and used method for dynamical studies. In this method, a small cylindrical specimen of the material to be tested is sandwiched between two long bars, the incident and transmitter bars (see Figure 6.4(a)). By impacting the incident bar with a third bar (the striker bar), a constant amplitude elastic compressive wave is created, which propagates down the incident bar to the specimen/bar interfaces. When this elastic wave reaches the bar-specimen interfaces, part of it is reflected back to the incident bar and the rest is transmitted through the transmitter bar, depending on the relative difference between the acoustic impedance of the bar material and the specimen. By measuring the corresponding pulses on the incident and transmitter bars with strain gages mounted on them, the specimen response (stress-strain) to the applied compressive load can be easily established using uniaxial elastic wave theory. The SHPB apparatus used consists of Inconel 718 bars, 326 mm striker, 3450 mm incident and 1850 mm transmitter bars, all with a diameter of 19 mm. Detailed information about the SHPB used is given in elsewhere [28]. The strain rate ($\dot{\varepsilon}$), the strain (ε) and the stress (σ) of the tested sample were calculated using the following equations;

$$\dot{\varepsilon}(t) = -\frac{2C_b}{L_s}\varepsilon_r(t) \qquad (5.1)$$

$$\varepsilon(t) = -\frac{2C_b}{L_s}\int_0^t \varepsilon_r(t) \qquad (5.2)$$

$$\sigma(t) = \frac{E_b A_b}{A_s}\varepsilon_t(t) \qquad (5.3)$$

where, C_b is the elastic wave velocity in the bar, E_b is the elastic modulus of the bar, L_s is the sample length and A_s and A_b are the sample and bar cross-sectional areas respectively. ε_I, ε_r and ε_t are incident, reflected and transmitted strains measured from strain gages on the bar, respectively. Typical SHPB test record of a tested sample of compact, composing of incident, reflected and transmitted strain records is shown in Figure 5.4 (b). Since the transmitter bar of the used SHPB is shorter than the incident bar, the tensile wave reflected from the transmitter bar end separates the bars and, therefore, the sample deforms only once under compression. The specimen dimensions, 15 mm in diameter and 10 mm in height, were the same for both quasi-static and high strain rate tests. At least three compression tests were performed at each strain rate studied. Few samples were also recovered without failure at quasi-static and high strain rates in order to assess the deformation modes of particles.

(a)

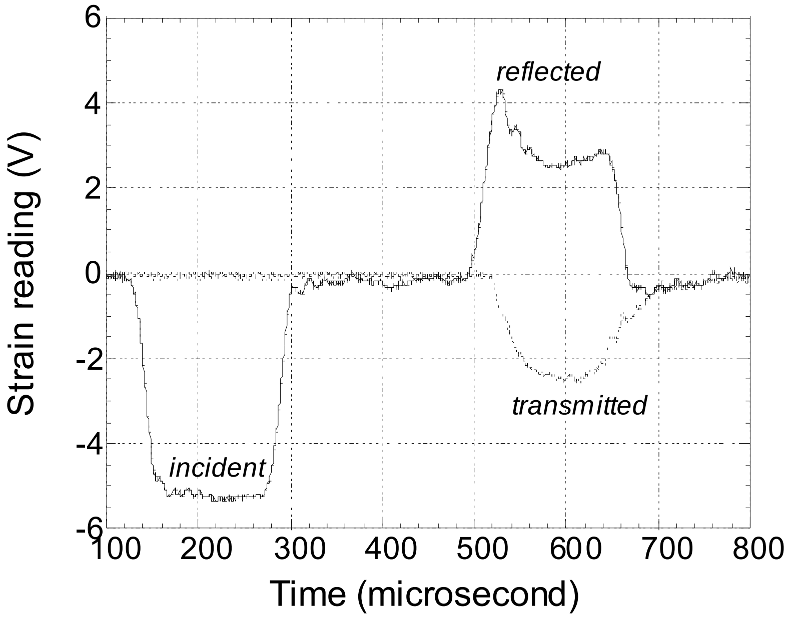

(b)

Figure 5.4 (a) Schematic of SHPB and (b) Typical SHPB strain gage readings of Ti6Al4V compact.

5.4 Microscopic studies

Microscopic analysis was performed on the vacuum epoxy-mounted as-received powder and untested and compression tested compact samples using optical microscopy and a Philips XL30-SFEG scanning electron microscope (SEM) with an Energy Dispersive X-ray (EDX) analyzer. Vacuum mounting was performed using a vacuum mounting equipment as shown in Figure 5.5. In the mounting process 200 ml epoxy was mixed with 1ml initiator and 2 ml accelerator and then poured onto the compacts under vacuum atmosphere. The polished cross-sections of samples were etched with Kroll's reagent (3 cm^3 of HF and 6 cm^3 of HNO_3 in 100 ml of H_2O). The percent porosity of sintered compact was measured by the Archimedes' method. The open and closed porosities of compacts were calculated by the differences between dry and wet weights (boiling in water).

Figure 5.5 Vacuum-mounting equipment.

5.5 Porosity and Pore Size Measurements

Porosity measurements were performed by the Archimedes' method after coating the surface of the compacts with paraffin to prevent penetration of water into the pores, similar to the method used previously [6]. After measuring the density of the compacts, porosities (P) were calculated via density values by using the following equations;

$$P = 1 - \rho_{rel} \tag{5.4}$$

$$\rho_{rel} = \frac{\rho_{com}}{\rho_{solid}} \tag{5.5}$$

where, ρ_{rel} is the relative density of the compact, ρ_{com} is the density of compact and ρ_{solid} is the density of Ti6Al4V. To determine the mean pore size of sintered Ti6Al4V, porous compacts were transversely cut and epoxy-mounted. Mean pore sizes of the compacts were calculated applying the linear intercept method on the images of the polished surface of the compacts using a Nikon Eclipse L150 optical microscope. At least 5 random lines were drawn onto the image of the powder compact and then pore sizes intercepting with the random lines were measured. The percentages and thicknesses of α and β phases were determined using an image analyzer.

Chapter 6

RESULTS

6.1 Microstructure of the as-received powders and thermogravimetry analysis of polyvinyl alcohol (PVA)

The microstructure of as-received Powder A (Figures 6.1 (a) and (b)) consists of acicular needle-like α which is known as martensitic α. This type of microstructure can form as a result of fast cooling (quenching) after heat treatment above β-transition temperature during atomization process. The microstructure of angular Powder B is bimodal microstructure (Figures 6.2 (a) and (b)). The microstructure is a combination of equiaxed α grains dispersed in a transformed β matrix. In Figure 6.2 (a) light regions are equiaxed α phase while dark phase is transformed β matrix consisting of lenticular α and β phases. Bimodal microstructure can be formed after annealing in $\alpha+\beta$ processing region (Figure 2.6).

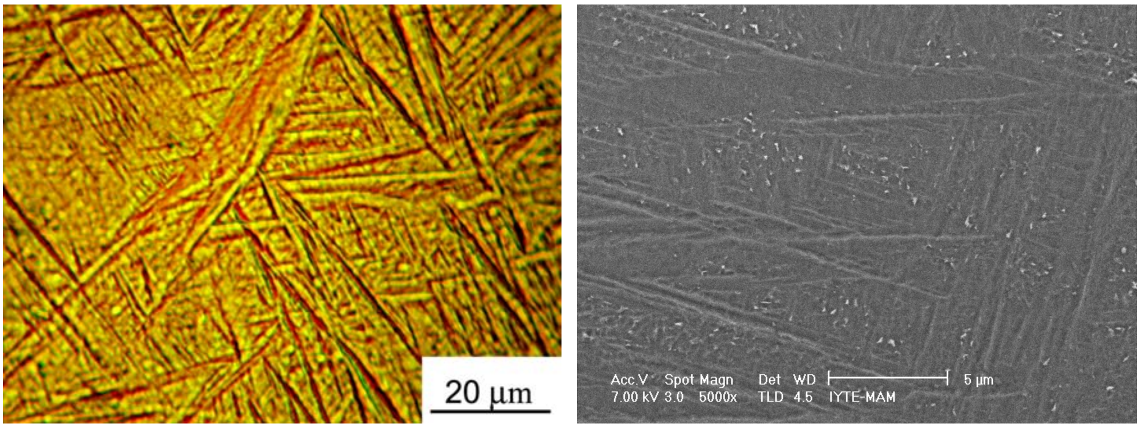

(a) (b)

Figure 6.1 (a) Optical and (b) SEM micrographs of spherical Powder A.

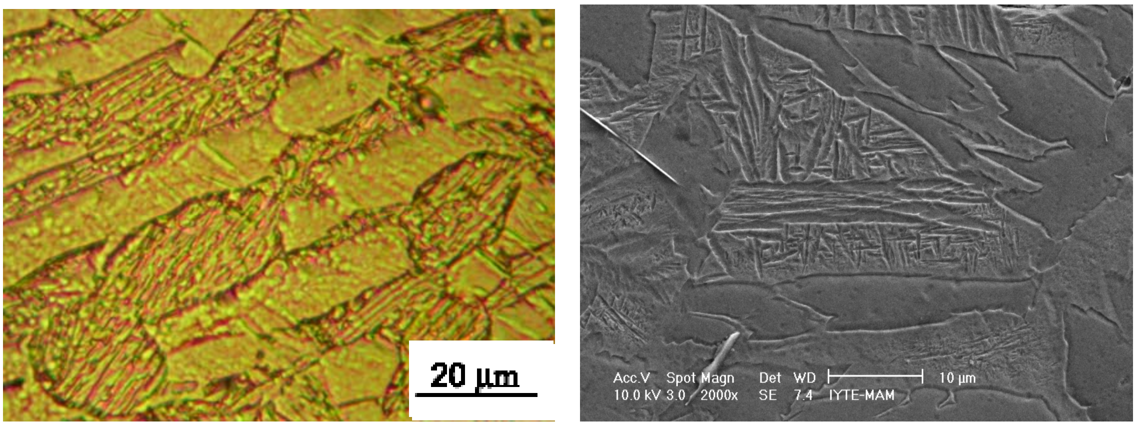

(a) **(b)**

Figure 6.2 (a) Optical and (b) SEM micrographs of angular Powder B.

Thermogravimetry analysis (TGA) curve of PVA used as binder in the compaction of powders is shown in Figure 6.3. The test was performed at a rate of 5 °C min^{-1}, the same as that of the heating rates of powder compacts. As depicted in Figure 6.3, the decomposition of PVA starts at a temperature of nearly 280 °C and continues up to 500 °C. In accord with TGA curve shown in Figure 6.3, the compacts prepared with PVA were kept for ½ hour at 450 °C for the removal of PVA.

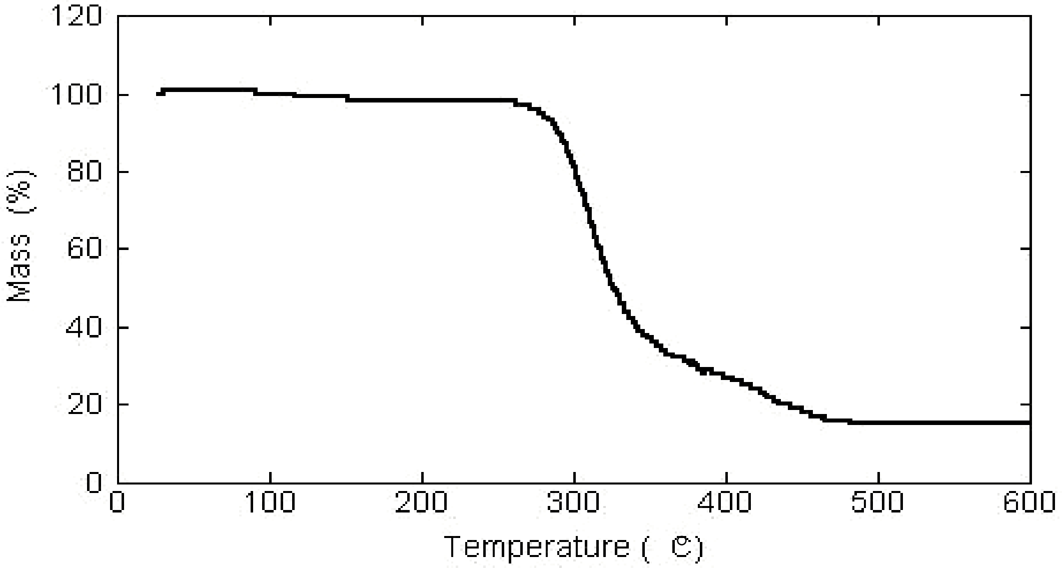

Figure 6.3 TGA curve of PVA used as binder.

6.2 Porosity and pore size measurements

The porosity and mean pore size of the compacts of powders <100 µm are tabulated together with the applied cold compaction pressures in Table 6.1. The porosity levels of the sintered Powder A and B compacts with <100 µm particle size are very similar; between 29% and 40% for Powder A and 33% and 44% for Powder B compacts (Table 6.1). The cold compaction pressure has a significant effect on the final measured porosity of the compacts. Increasing compaction pressure increases the relative density of green compacts by providing higher contact areas between particles, leading to decrease in final compact porosities. In Figures 6.4 and 6.5 the optical microscope micrographs of the sintered Powder A and Powder B compacts at different compaction pressures are shown, respectively. At increasing compaction pressures both porosity and pore sizes are seen to decrease in these figures for both types of powder compacts. The mean pore sizes of the powder compacts of <100 µm range between 34 and 96 µm.

Table 6.1 Compaction pressure, porosity and pore size of the compacts (<100 µm).

Compaction Pressure (MPa)	**Powder A**		**Powder B**	
	Porosity (%)	**Mean Pore Size (µm)**	**Porosity (%)**	**Mean Pore Size (µm)**
50	-	-	44	96 (14-326)
100	-	-	42	81 (16-372)
200	40	44 (9-128)	36	67(16-216)
300	34	38 (9-120)	35	64 (19-187)
400	32	37 (9-120)	33	56 (18-200)
500	29	34 (8-125)	-	-

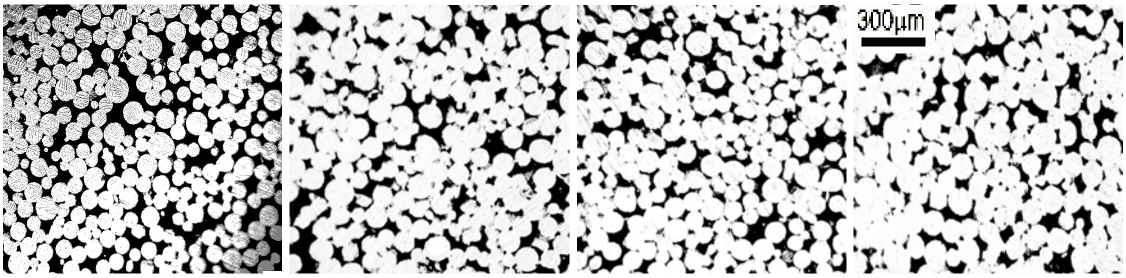

(a) (b) (c) (d)

Figure 6.4 Optical micrographs of Powder A compacts (<100 μm) (a) 40% (200 MPa), (b) 34% (300 MPa), (c) 32% (400 MPa) and (d) 29% (500 MPa).

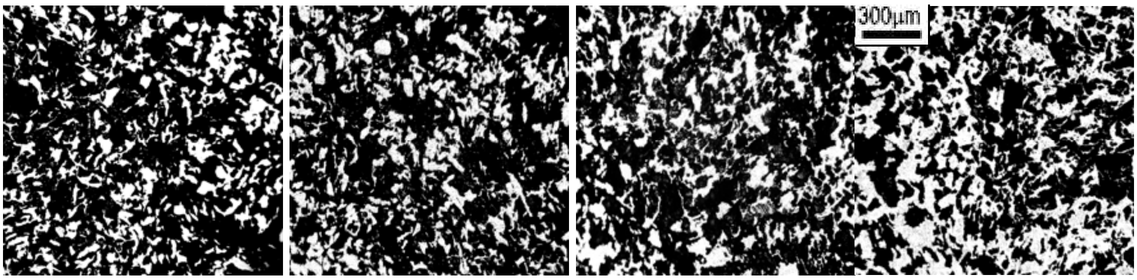

(a) (b) (c) (d)

Figure 6.5 Optical micrographs of Powder B compacts (<100 μm) (a) 44% (50 MPa), (b) 42% (100 MPa), (c) 36% (200 MPa) and (d) 33% (400 MPa).

The final percent porosities and mean pore sizes of the sintered Powder A and B compacts of 100-200 μm are tabulated in Table 6.2 together with the applied cold compaction pressures. The percent porosity levels in these compacts as tabulated in Table 6.2 are between 34% and 41% for Powder A and 43% and 54% for Powder B compacts, higher than those of <100 μm. Relatively higher porosity found in Powder B compacts than Powder A compacts at the same cold compaction pressures (200 and 400 MPa) is most likely due to angular particle shape, leading to the packing of irregular shaped particles. The mean pore sizes range between 80 and 98 μm for Powder B and 53 and 81 μm for Powder A compacts. The minimum and maximum pore sizes are 10 and 300 μm, respectively.

Table 6.2 Compaction pressure, porosity and pore size of the compacts (100-200 μm).

Compaction Pressure (MPa)	**Powder A**		**Powder B**	
	Porosity (%)	**Mean pore size (μm)**	**Porosity (%)**	**Mean pore size (μm)**
50	-	-	54	98 (10-300)
100	-	-	51	90 (10-300)
200	41	81 (16-272)	49	87(10-300)
300	40	82(16-200)	46	85(10-300)
400	38	63(16-200)	43	80(10-300)
500	34	53(16-200)	-	-

Optical microscope images of the polished surfaces of Powder A and B compacts with different porosity levels are shown in Figures 6.6 and 6.7, respectively. Larger pore sizes of Powder B compacts are clearly seen in these figures, proving the higher porosity level. These figures also show a more nonhomogenous pore size distribution in Powder B compacts than Powder A compacts due to differences in the morphologies of the powders.

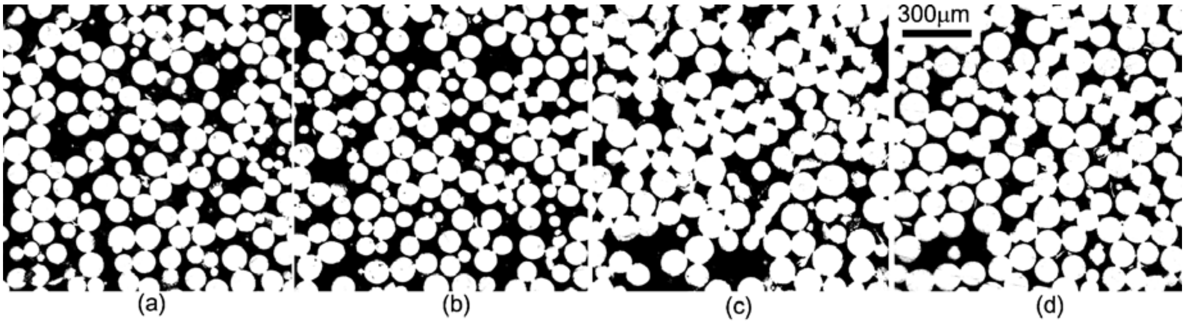

Figure 6.6 Optical micrographs of Powder A compacts (100-200 μm) (a) 41% (200 MPa), (b) 40% (300 MPa), (c) 38% (400 MP) and (d) 34% (500 MPa).

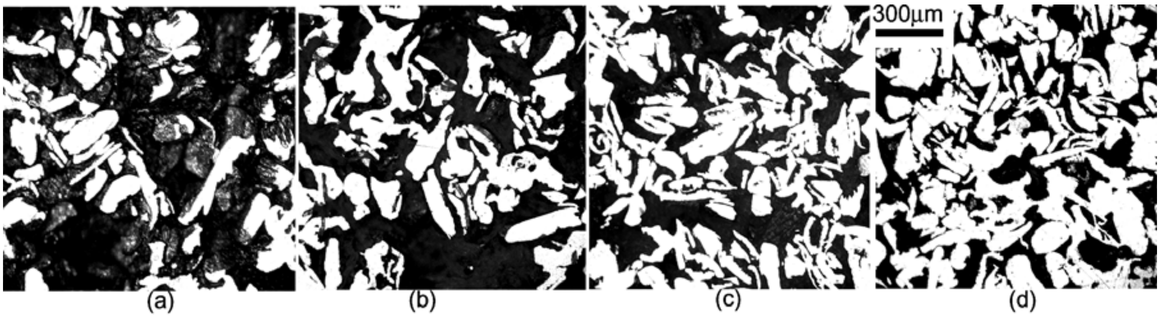

Figure 6.7 Optical micrographs of Powder B compacts (100-200 μm) (a) 54% (50 MPa), (b) 51% (100 MPa), (c) 49% (200 MPa) and (d) 43% (400 MPa).

The final percent porosities and mean pore sizes of the sintered Powder A and B compacts of 200-300 μm are tabulated in Table 6.3 together with the applied cold compaction pressures. The percent porosity levels are between 40% and 50% for Powder A and 45% and 63% for Powder B compacts. Again, the porosity levels in Powder A compacts are higher than those of Powder B compacts for the reason of the angular particle shape and also higher mean particle size of Powder B compacts. Optical microscope images of the polished surfaces of Powder A and B compacts with different porosity levels are shown in Figures 6.8 and 6.9, respectively. Again, larger pore sizes of Powder B compacts are clearly seen in these figures.

Table 6.3 Compaction pressure, porosity and pore size of the compacts (200-300 μm).

Compaction Pressure (MPa)	**Powder A**		**Powder B**	
	Porosity (%)	**Mean Pore Size (μm)**	**Porosity (%)**	**Mean Pore Size (μm)**
50	-	-	63	171 (14-442)
100	-	-	59	152 (14-471)
200	50	113 (12-331)	53	112 (16-395)
300	42	99 (7-251)	49	98 (14-329)
400	41	79 (11-277)	45	86 (27-273)
500	40	61 (10-182)	-	-

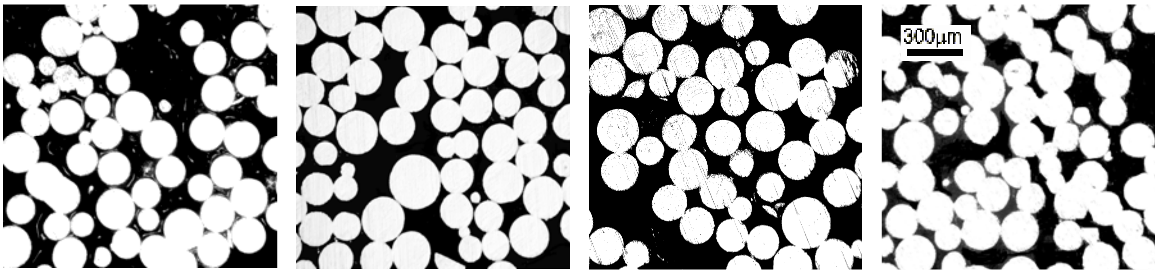

(a) (b) (c) (d)

Figure 6.8 Optical micrograph of the cross-section of Powder A compacts (200-300 μm) (a) 50% (200 MPa), (b) 42% (300 MPa), (c) 41% (400 MPa) and (d) 40% (500 MPa).

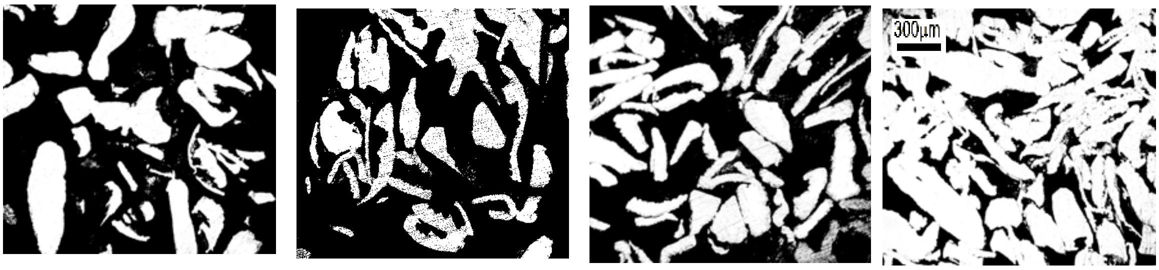

(a) (b) (c) (d)

Figure 6.9 Optical micrograph of the cross-section of Powder B compacts (200-300 μm) (a) 63% (50 MPa), (b) 59% (100 MPa), (c) 53% (200 MPa) and (d) 45% (400 MPa).

The variation of mean pore size with percent porosity of the compacts prepared is shown in Figure 6.10. The porosity varies between 33% and 64% while the mean pore size range is between 34 and 171 μm. The maximum mean pore size is found in 200-300 μm Powder B compacts compacted at 50 MPa and the minimum in <100 μm Powder A and B compacts. A power-law interpolation to the mean pore size-percent porosity data is also applied as shown in the same figure. Figure 6.11 further shows the variation of porosity with the applied compaction pressure for the three different group of particle size ranges of the powder compacts. At the same compaction pressure highest porosity level was found in powder compacts prepared from the powders having the largest particle size.

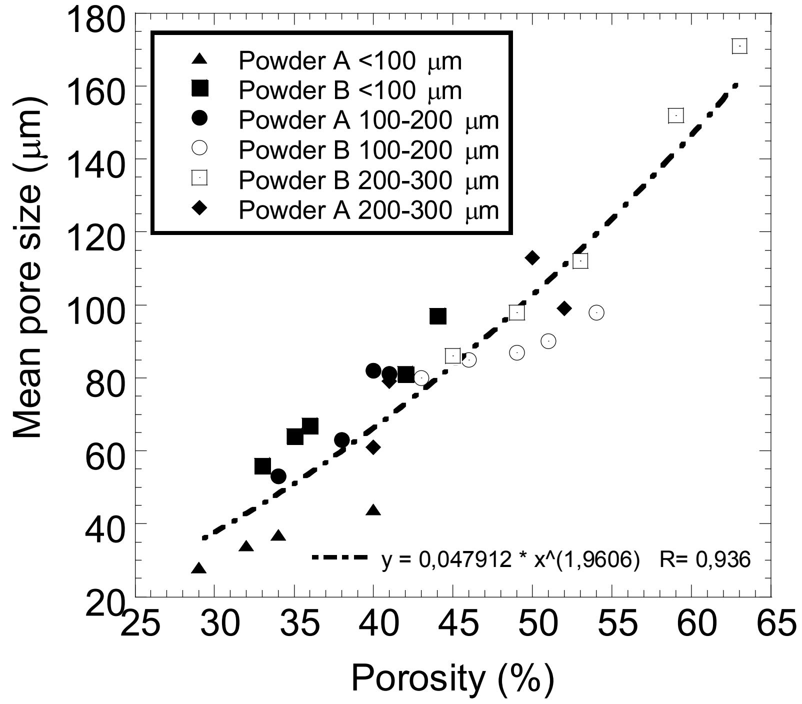

Figure 6.10 Variation of mean pore size with percent porosity of Powder A and B compacts and power-law interpolation.

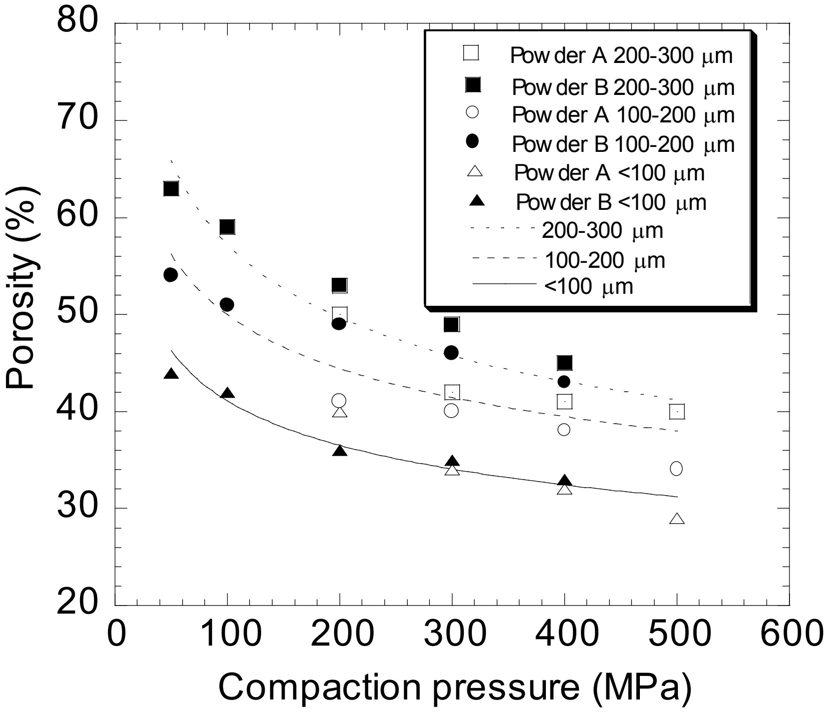

Figure 6.11 Variation of porosity with compaction pressure in each particle size range of powders.

6.3 Compression mechanical properties at quasi-static strain rates

The representative compressive stress-strain curves of Powder A and Powder B compacts of particle size <100 μm are shown at various compaction pressures in Figures 6.12 and 6.13, respectively. The elastic modulus of the compacts is determined in the initial linear region of stress-strain graph and the yield strength is taken as the proportional limit as shown in Figures 6.12 and 6.13. Powder A compacts show compression behavior composing of two deformation regions; a linear elastic region followed by an inelastic deformation region, similar to the compression behavior of the bulk alloys. These compacts did not fail until about large strains, ~30%. The effect of increasing compaction pressure is to decrease the porosity and hence increase the yield and flow stresses. Contrary to Powder A compacts, Powder B compacts show relatively lower yield strength values and fracture strains. In these samples, the stress rises to a maximum stress (compressive strength) as marked by arrows in Figure 6.13, after which the compacts fail by shear banding. The strains corresponding to the maximum stress in these figures are considered as the failure strain.

Powder A and B compacts of particle sizes of 100-200 μm show very similar compression stress-strain behavior; after maximum stress (compressive strength), the stress decreases rapidly due to failure via shear banding except Powder A compacts compacted at 400 and 500 MPa (Figures 6.14 and 6.15). In Powder A compacts with higher compaction pressure after attainment of the maximum stress the samples deform almost at constant stresses, a behavior similar to that of foamed metals. The higher compressive strength found in Powder A compacts as compared with Powder B compacts is due to the lower porosity attained in Powder A compacts at the same compaction pressures. Compressive strengths of angular compacts also increase with increasing compaction pressure or with decreasing percent porosity as depicted in Figure 6.15.

Compression stress-strain curves of Powder A and Powder B compacts of particle sizes 200-300 μm at various compaction pressures are shown in Figures 6.16 and 6.17, respectively. The compression strength values are higher for Powder B compacts at similar porosity levels. The relatively higher strength of Powder B compacts will be discussed in Chapter 7 in terms of microstructures of the compacts.

Finally, the compressive strength values range between 30 and 115 MPa and 7 and 125 MPa for Powder A and Powder B compacts, respectively.

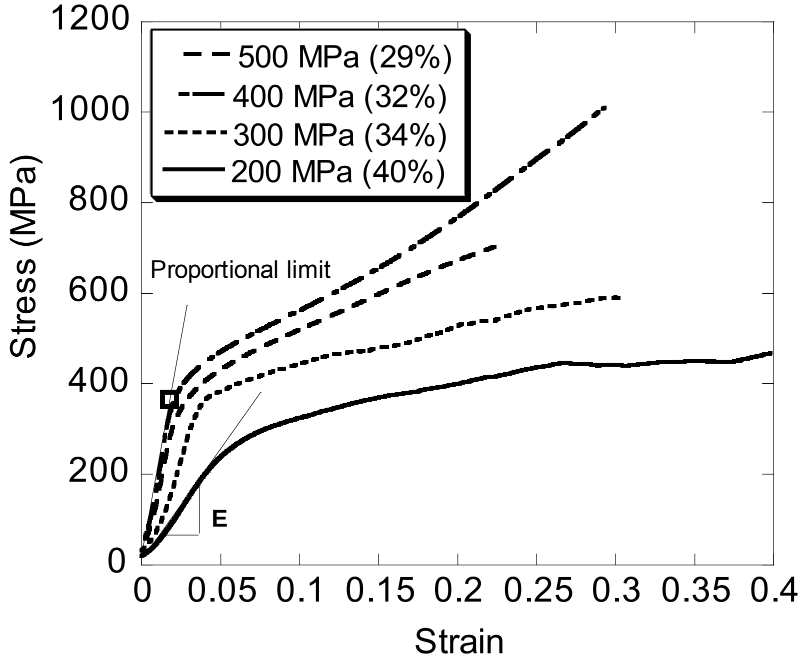

Figure 6.12 Compression stress-strain curves of Powder A compacts (<100 μm) at various compaction pressures.

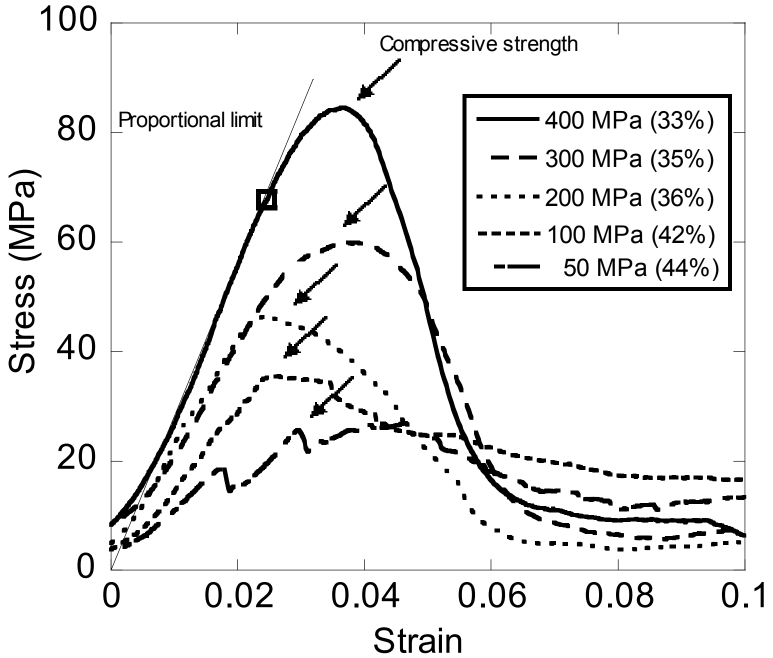

Figure 6.13 Compression stress-strain curves of Powder B compacts (<100 μm) at various compaction pressures.

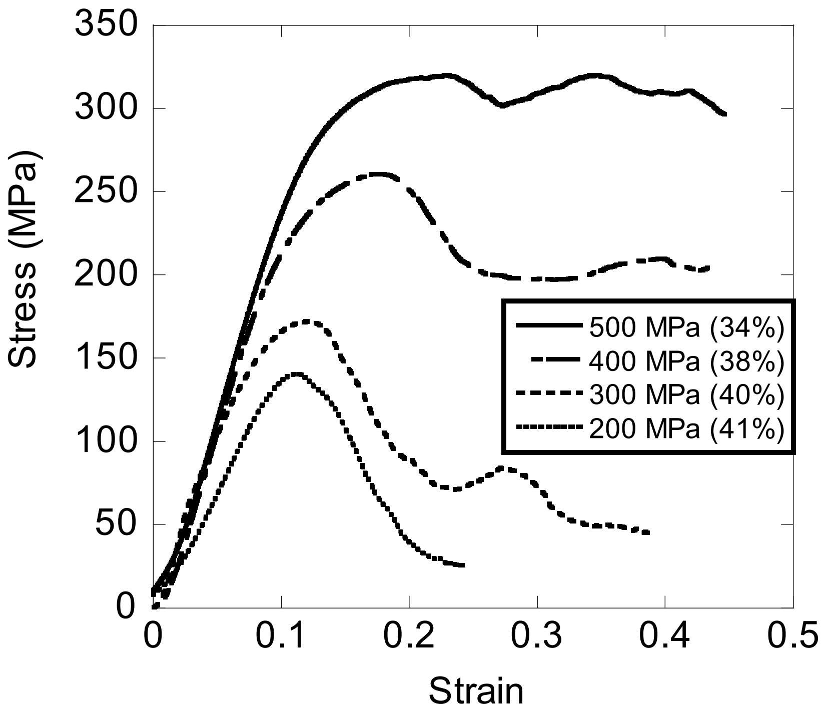

Figure 6.14 Compression stress-strain curves of Powder A compacts (100-200 μm) at various compaction pressures.

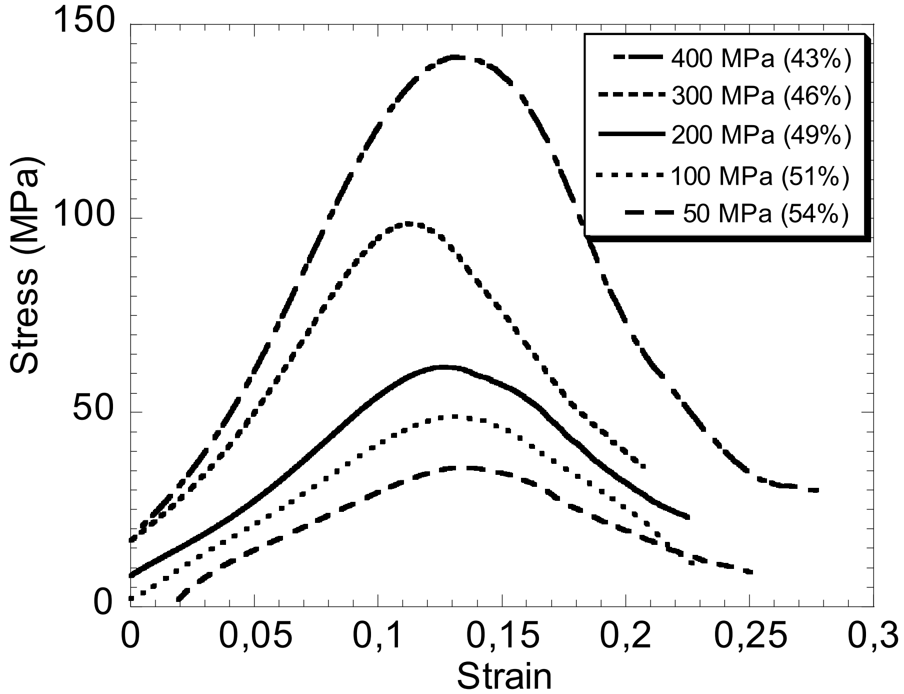

Figure 6.15 Compression stress-strain curves of Powder B compacts (100-200 μm) at various compaction pressures.

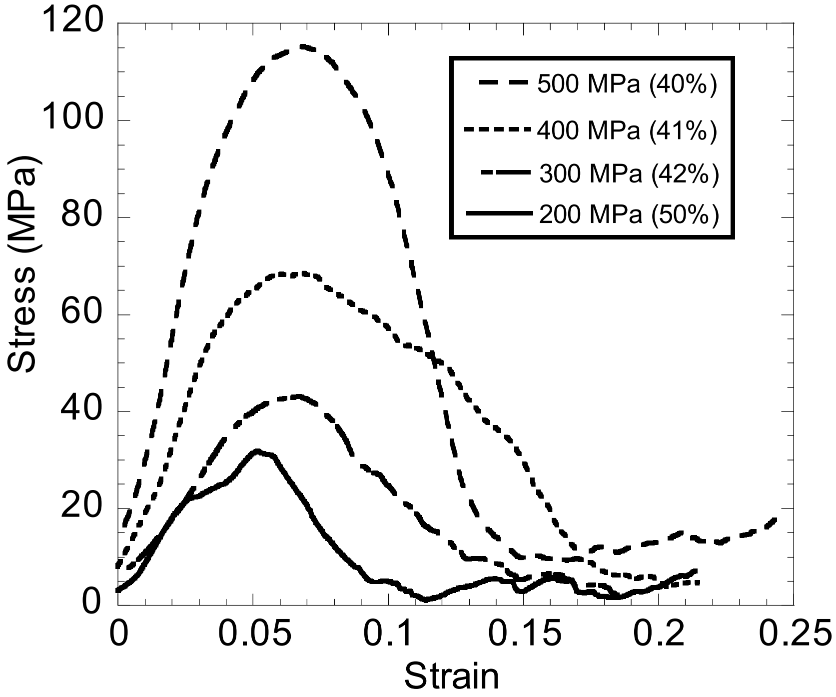

Figure 6.16 Compression stress-strain curves of Powder A compacts (200-300 μm) at various compaction pressures.

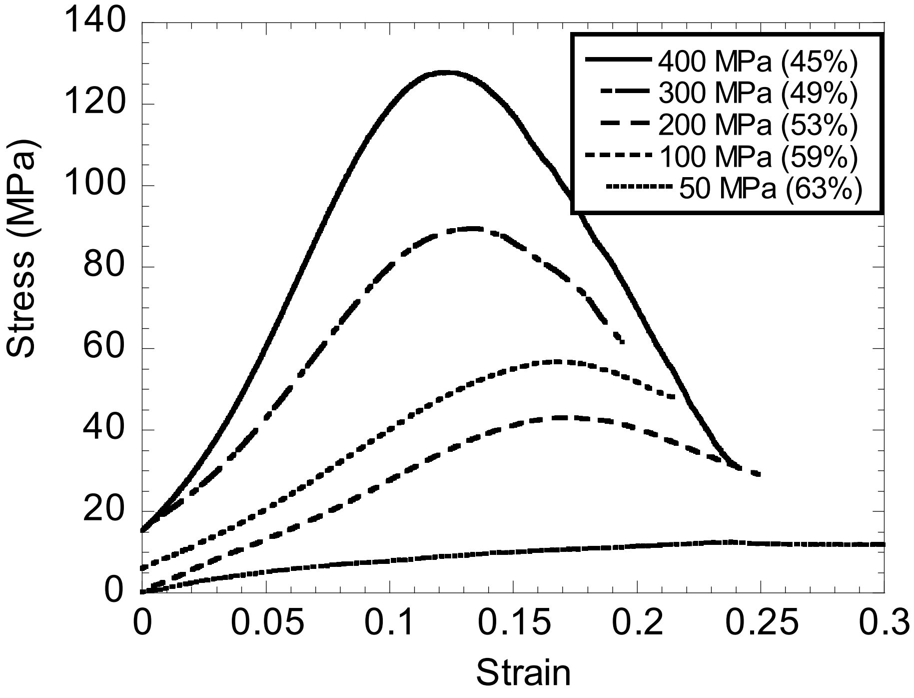

Figure 6.17 Compression stress-strain curves of Powder B compacts (200-300 μm) at various compaction pressures.

6.4 Effects of porosity and powder type on the elastic modulus

The effect of porosity on the modulus of Powder A compacts of 3 different sizes of particles is shown in Figure 6.18. The modulus values range between 1 and 17 GPa for Powder A compacts. In Powder B compacts the modulus values are lower, ranging between 0.5 and 6 GPa (Figure 6.19). The lower modulus values of Powder B compacts as seen in Figure 6.20 are due to the higher porosity levels found in these compacts.

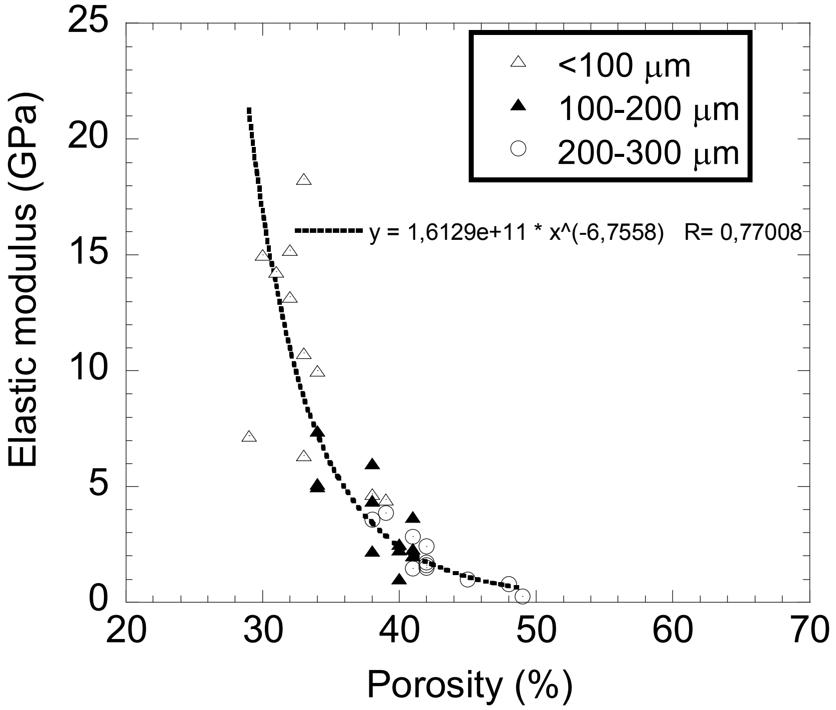

Figure 6.18 Variation of elastic modulus with percent porosity of Powder A compacts.

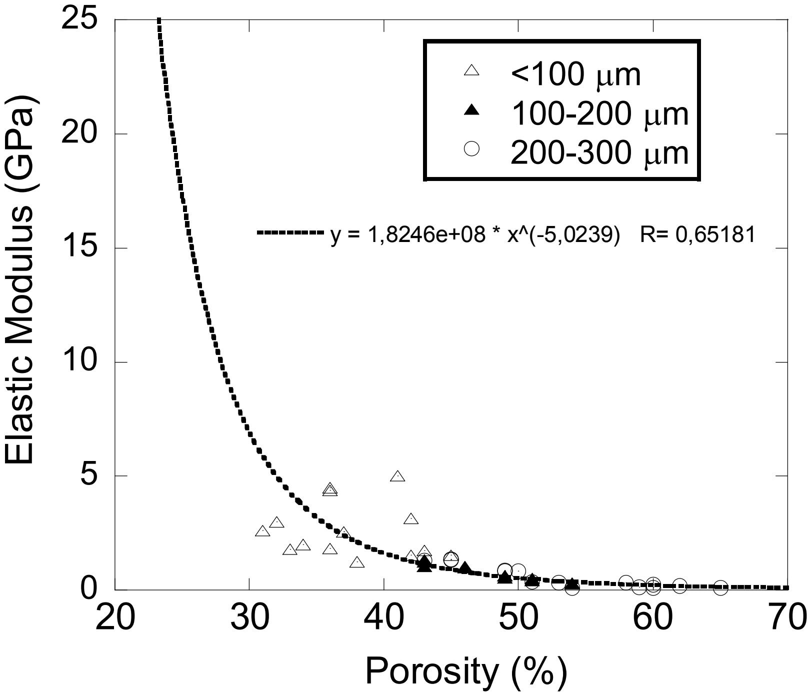

Figure 6.19 Change of elastic modulus and porosity of Powder B compacts.

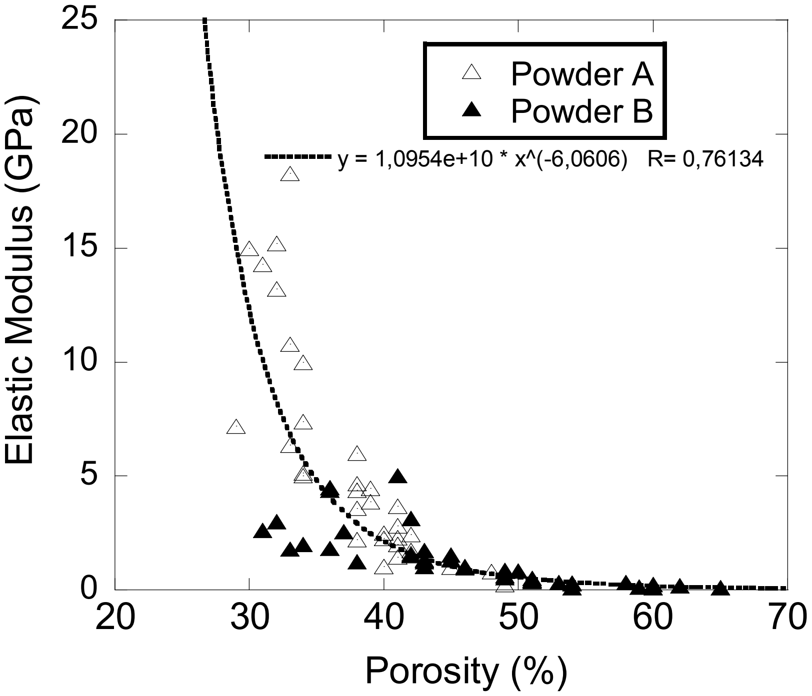

Figure 6.20 Variation of elastic modulus of compacts with percent porosity.

6.5 Effects of porosity and powder type on the yield and compressive strength

The effects of particle size and porosity on the yield strength of the Powder A and Powder B compacts are shown in Figures 6.21 and 6.22, respectively. The yield strength of Powder A compacts increases with decreasing particle size at the same porosity level (A, B and C in Figure 6.21) and with decreasing porosity level. Unlike the yield strength of powder A compacts of <100 μm, the yield strength of powder B compact of <100 μm is lower than those of larger powder sizes (Figure 6.22). Figure 6.23 shows a linear relation between yield strength and porosity level of powder compacts. It should be noted that the yield strength of Powder B compacts of <100 μm is excluded in the linear interpolation for the reason of a different failure mechanism in these compacts which will be explained in Chapter 7. The compressive strength of Powder A and B compacts increases with decreasing particle size and/or decreasing porosity level (Figure 6.24(a) and (b)), except Powder B compacts of <100 μm (Figure 6.24(b)).

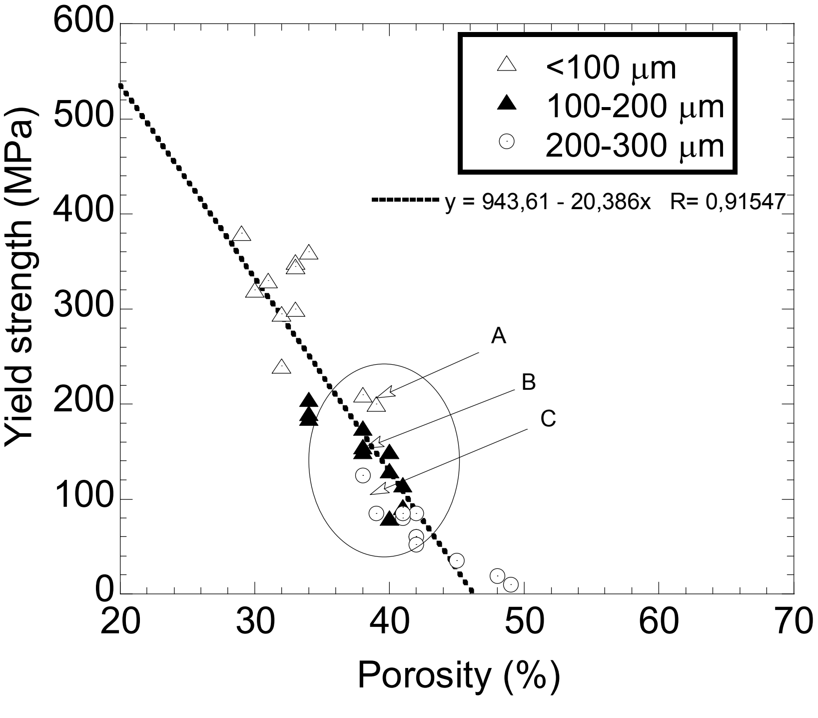

Figure 6.21 Variation of yield strength of Powder A compacts with porosity.

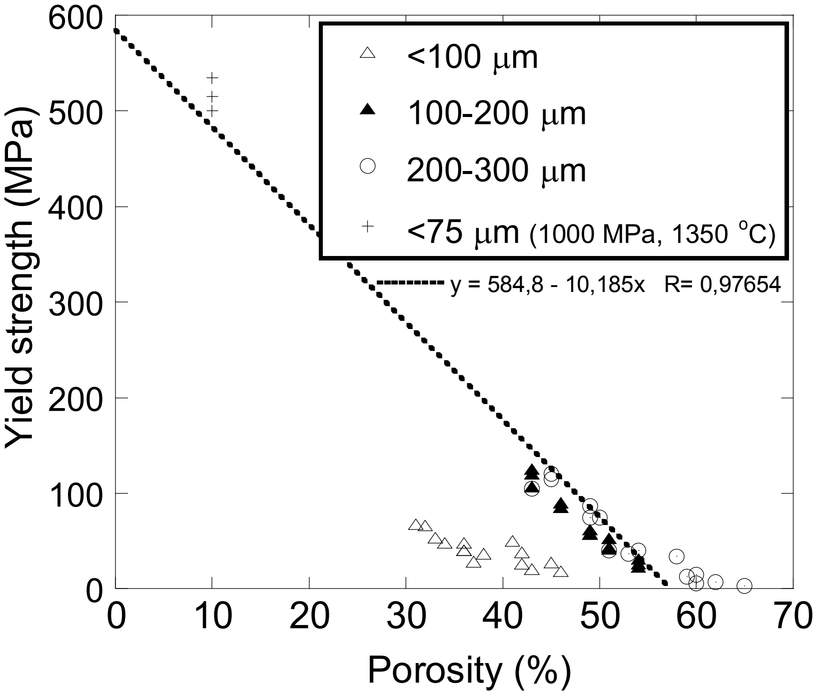

Figure 6.22 Variation of yield strength of Powder B compacts with porosity.

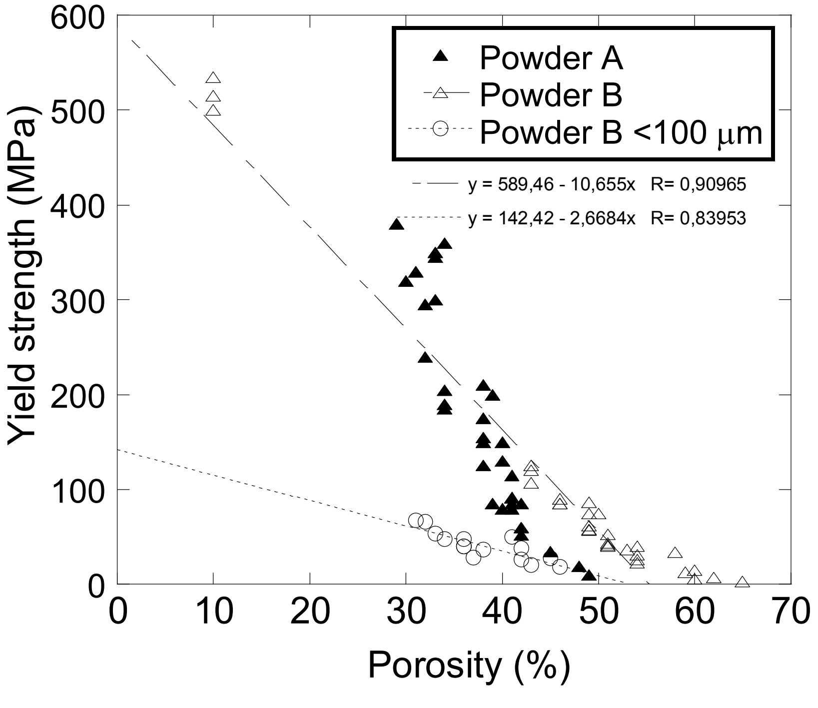

Figure 6.23 Variation of yield strength of powder compacts with porosity.

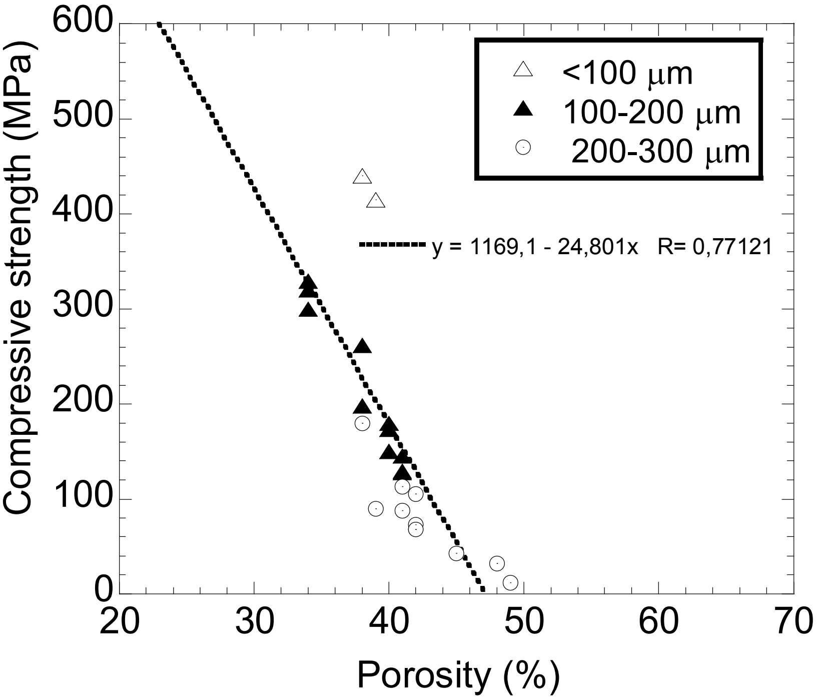

(a)

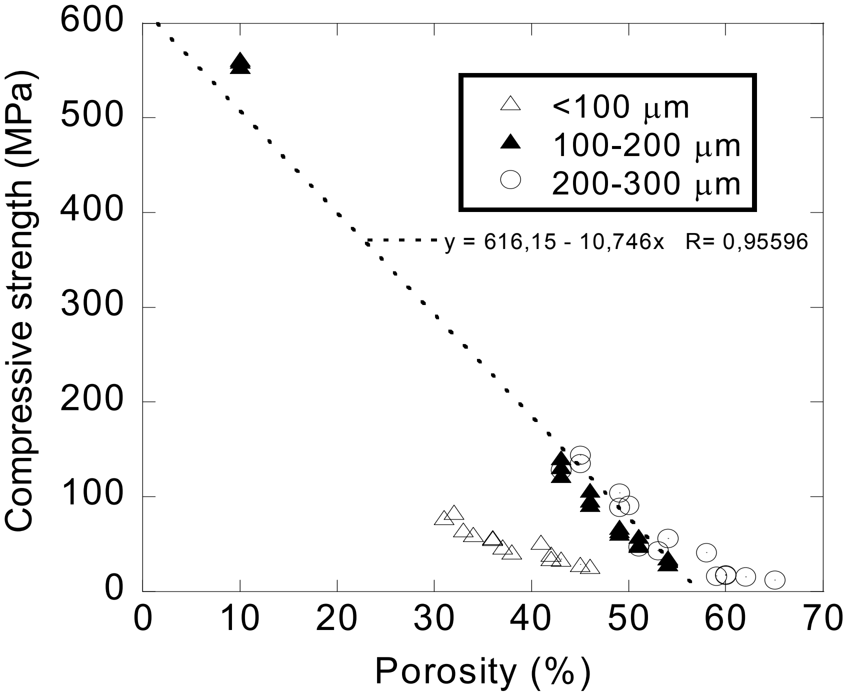

(b)

Figure 6.24 Variation of compressive strength of (a) Powder A and (b) Powder B compacts with porosity.

6.6 Effect of strain rate on the compression behavior

The effect of strain rate on the compression stress strain curves of Powder A compacts of 36-38% porosity is shown in Figure 6.25. Increasing strain rates increases the flow stress and compressive strength of compact. The compressive strength increases from about 240 MPa at quasi-static rates ($1.6\text{x}10^{-3}$ s^{-1}) to 300 MPa at high strain rates (900 s^{-1}) without significantly affecting the strain corresponding to compressive strength (Fig. 6.25).

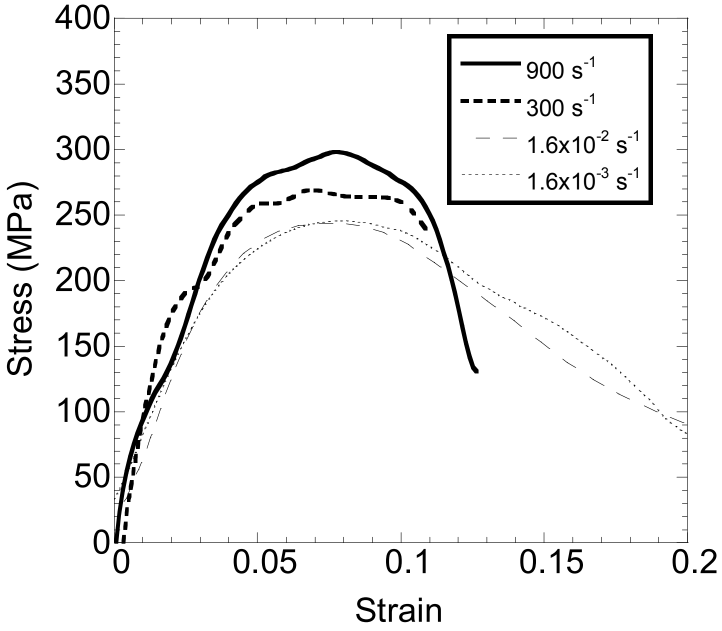

Figure 6.25 Compression nominal stress-strain curves of Powder A compacts of 100-200 μm with 36%-38% porosities at various strain rates.

6.7 Microscopic studies

Powder A compacts showed Widmanstätten structure. In this structure, colonies of β lathes (bcc and rich in V) and α platelets (hcp and rich in Al) formed inside the prior β grains (Figure 6.26(a) and (b)). The percentage and thickness of β phase were measured typically 18-20% and 0.2-1 μm, respectively. The thickness of α platelets varied between 4 and 8 μm and it was also microscopically observed that the thickness of α platelets increases at and near the interparticle bond region. Figures 6.27, 28 and 29 show the microstructures of Powder A compacts of three different size ranges at different compaction pressures. It is clearly seen in these figures (a) the bonding area between particles increases with compaction pressure (b) particle deformation is more pronounced at compaction pressure of 400 and 500 MPa and (c) the microstructure remains to be same for all Powder compacts, compacted at different pressures.

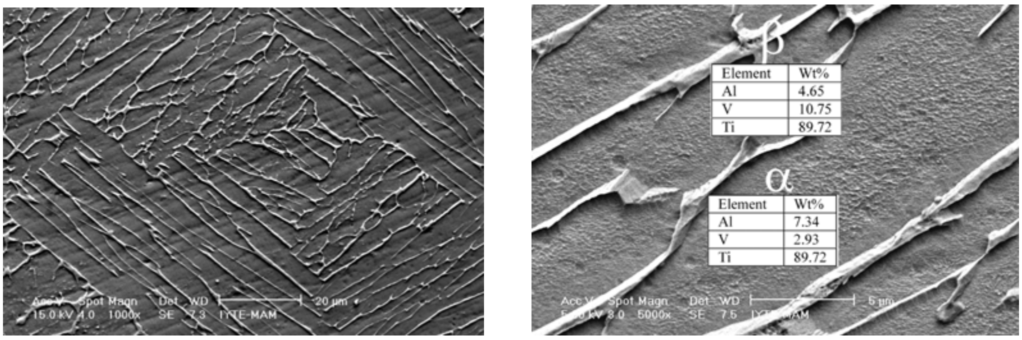

Element	Wt%
Al	4.65
V	10.75
Ti	89.72

Element	Wt%
Al	7.34
V	2.93
Ti	89.72

Figure 6.26 SEM image showing Widmanstätten microstructure of sintered Powder A compact and (b) magnified image of Widmanstätten microstructure showing α and β.

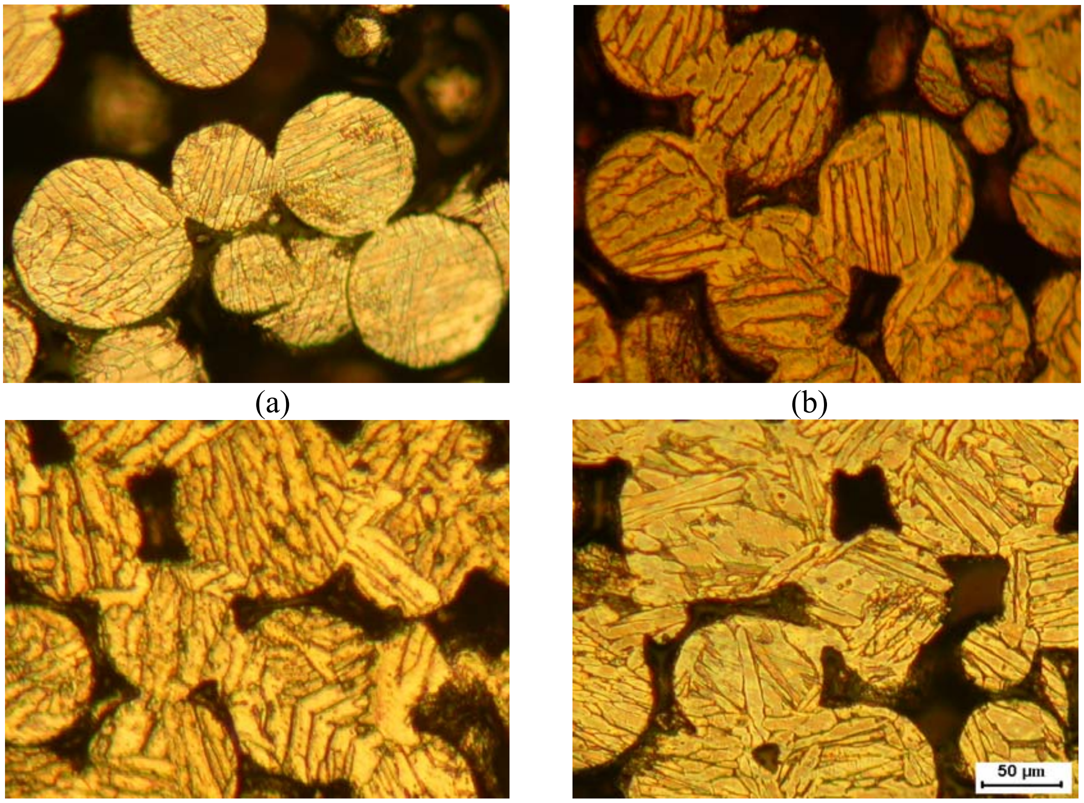

(a) (b)

(b) (d)

Figure 6.27 Microstructure of A compacts (<100 µm) (a) 200 MPa (b) 300 MPa (c) 400 MPa (d) 500 MPa.

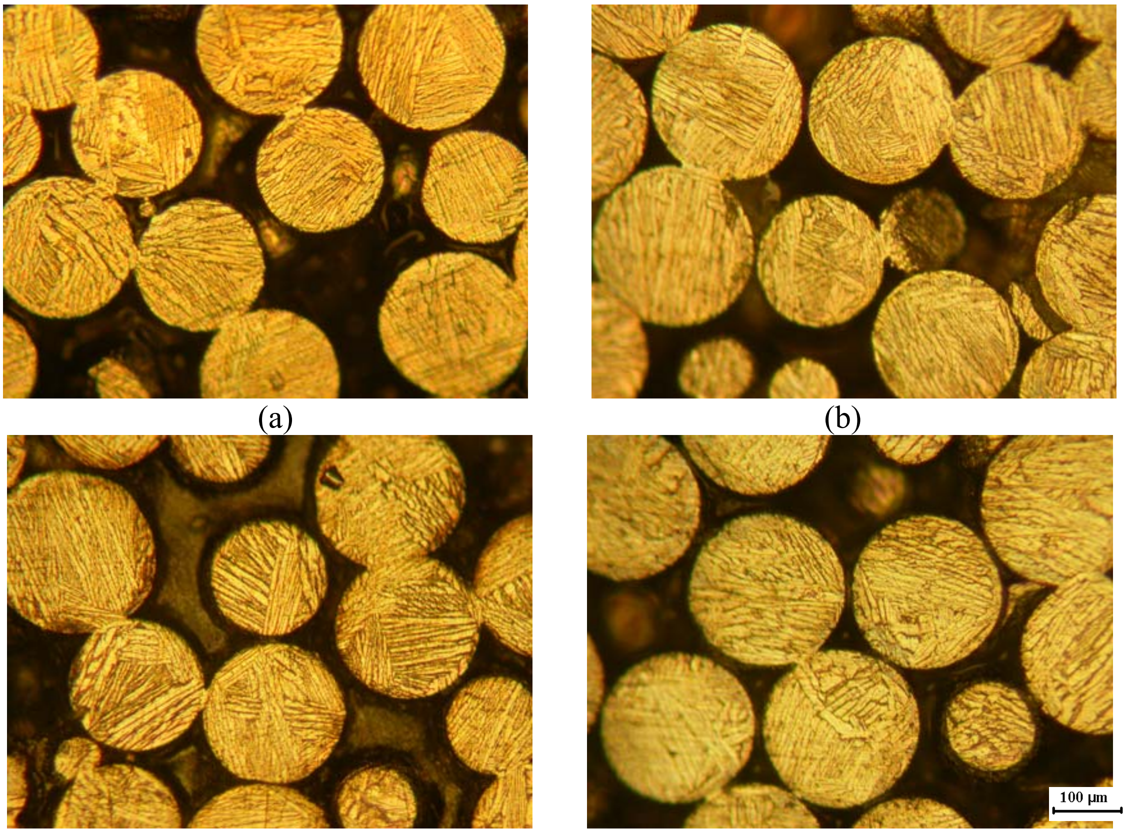

(a) (b)

(c) (d)

Figure 6.28 Microstructure of A compacts (100-200 μm) 200 MPa (b) 300 MPa (c) 400 MPa (d) 500 MPa.

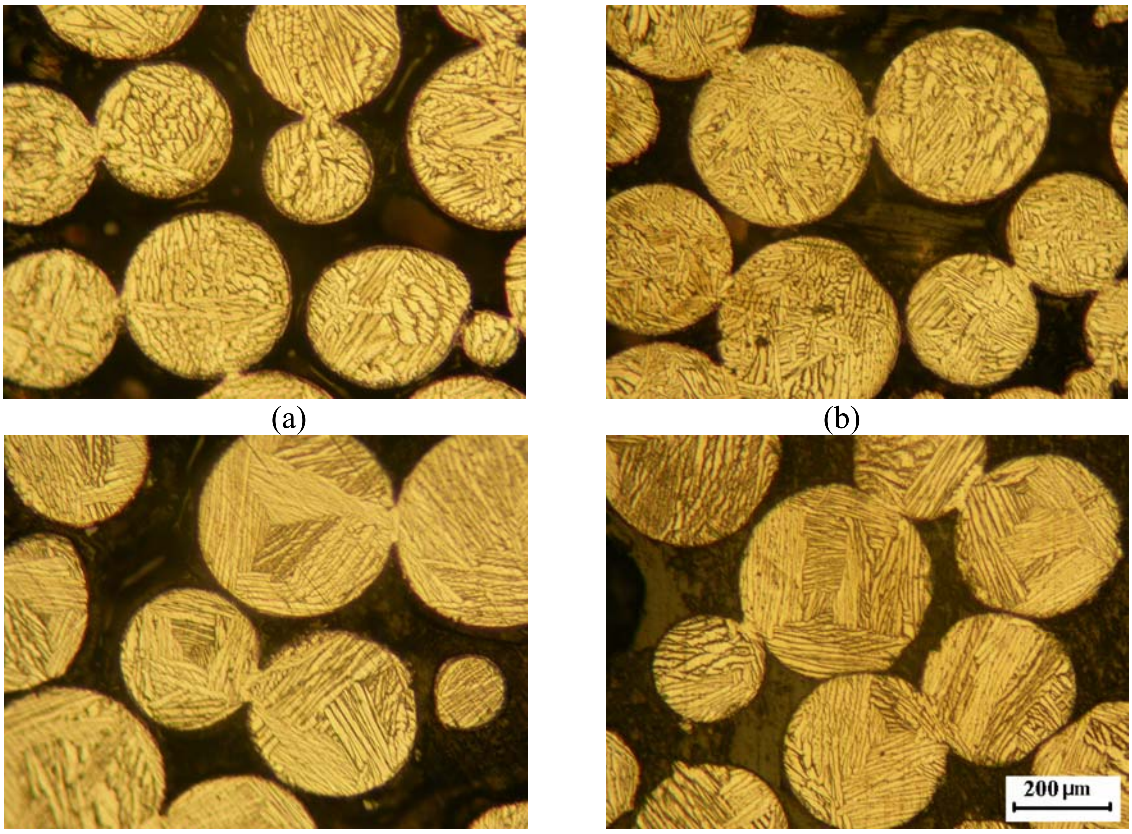

(a) (b)

(c) (d)

Figure 6.29 Microstructure of A compacts (200-300 μm) (a) 200 MPa (b) 300 MPa (c) 400 MPa (d) 500 MPa.

The microstructure of angular Powder B compacts of <100 μm and 100-200 μm is a mixture of Widmanstätten phase and equiaxed α grains as shown in Figures 6.30(a-d). The fraction of equiaxed α grains was measured 10% quantitatively. It was also found that there was no significant effect of pressure on the microstructures of the compacts.

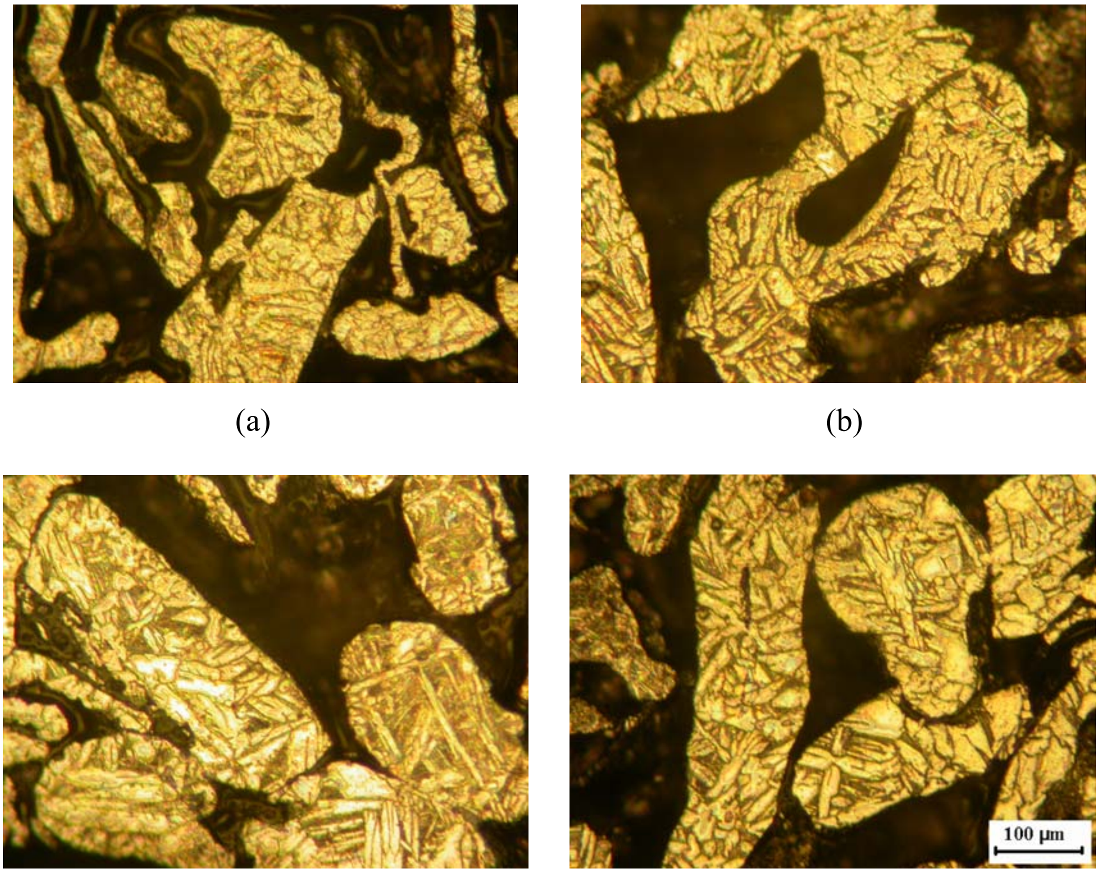

(a) (b)

(c) (d)

Figure 6.30 Microstructure of Powder B compacts (100-200 µm) (a) 50 MPa (b) 100 MPa (c) 200 MPa (d) 400 MPa.

The microstructure of the 200-300 µm angular Powder B compacts is also similar to 100-200 µm angular Powder B compacts except the fraction of equiaxed α grains increased to 72%. Figures 6.31 (a-d) show the microstructure of these compact at various compaction pressures.

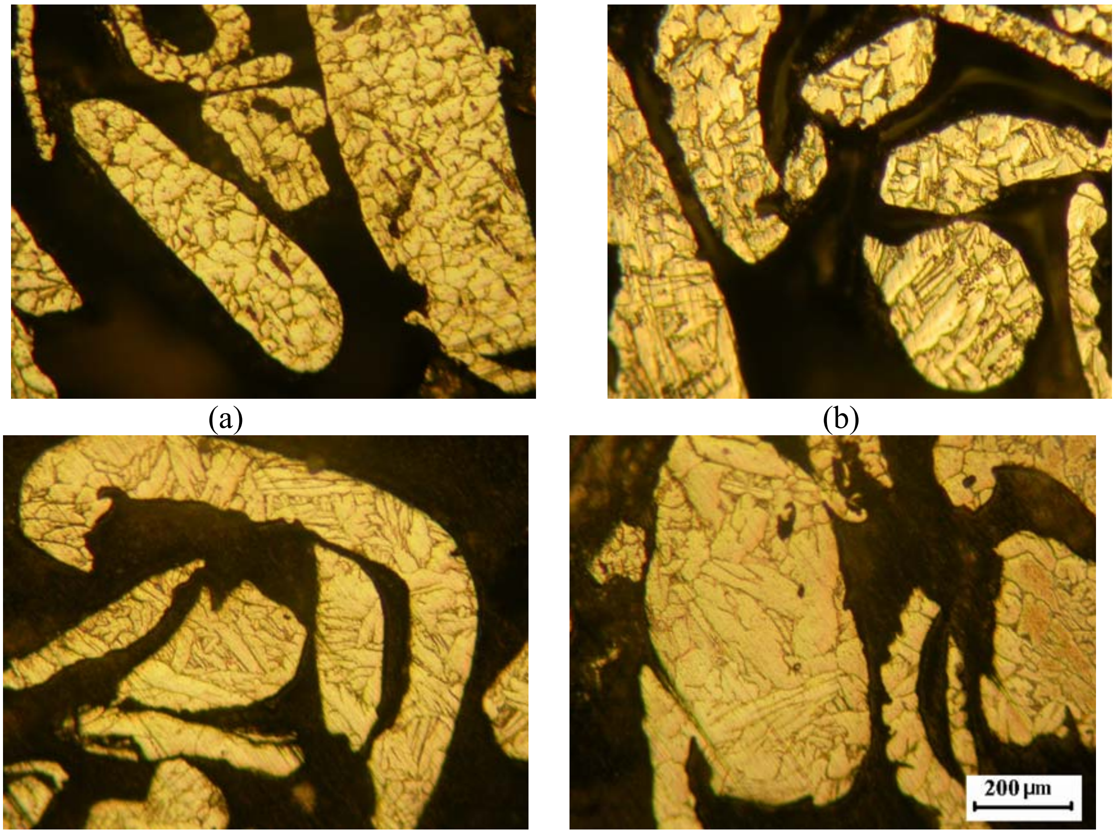

(a) (b) (c) (d)

Figure 6.31 Microstructure of Powder B compacts (200-300 µm) (a) 50 MPa (b) 100 MPa (c) 200 MPa (d) 400 MPa.

6.8 Deformation and failure modes under compressive loads

Typical compression stress-strain curves of the compacts at quasi-static strain rates shown in Figure 6.32 can be considered in three distinct deformation regions marked as I, II and III. In region I, the compact is elastically compressed until about the proportional limit. In region II, particle inelastic deformation takes place under normal and shear forces as will be elaborated later. At and/or before maximum stresses or compressive strength, deformation presumably starts to become non-uniform as two conic shear bands begin to develop along the diagonal axes of the compacts as shown in Figures 6.33 (a) and (b) for a failed Powder A compact. Deformation localization in the shear bands or shear banding results in reduction in load carrying capacity of the deforming compact in Region III (Figure 6.32). The complete failure occurs with the separation of bonded particles on the shear bands, starting from the corners of the cylindrical compact sample (Figures 6.33 (a) and (b)). This failure mode of deformation was found to be the same at both quasi-static and high strain rates tested Powder A compacts and also for Powder B compacts. The exemption is the Powder A compact of <100 μm. In these compacts failure did not occur until about large strains but cracks were observed on the surface (see Figure 6.34).

The polished and etched cross-sections of Powder A samples deformed until about the maximum stress in Region II of Figure 6.32 showed that particles were compressed into oblate spheroids and complex shapes, particularly near the shear band region (Figure 6.35(a)). SEM micrographs of fracture surface of failed specimen shown in Figures 6.35(b) and (c) feature few of the important deformation mechanisms of compact as (i) the separation of particles primarily occurs at the interparticle bond region, (ii) the fracture of interparticle bond region is ductile type composing of dimples (iii) originally non-contacting particles develop contacts with neighboring particles during deformation as marked by arrows in Figure 6.35(b), and (iv) as a result of particle inelastic deformation the contact area between bonded particles increases over the interparticle bond area. The presence of localized shear regions on the interparticle bond regions (Figure 6.36(a) and (b)) and the evidence of ductile dimpled fracture surfaces (Figure 6.37) further indicated the development of large shear and/or normal stresses between particles in the interparticle bond regions. In samples deformed through Region III, voids and macrocracks were observed in the interparticle bond region at both quasi-static and high strain rates (Figure 6.38(a)). Voids were observed to initiate primarily in α platelets and/or at β/α interface and their sizes were measured 1-2 μm before coalescence. The growth and coalescence of these voids eventually lead to the development of macrocracks and complete separation of interparticle bond region. Figure 6.38(b) and (c) show the magnified SEM image of the interior and tip of a macrocrack. On the crack surface many dimples are seen and the distance between the dimples is well agreed with the measured void size. Finally, the fracture surface of particles should be composed of two different sizes of dimples; small dimples formed by the void coalescence in α platelets with a distance between them determined by the void size (1-2 μm) and large dimples formed due to the ductile failure of β lathes with a distance between them determined by the thickness of α phase (4-8 μ). These are consistent with the dimple sizes on the fracture surface shown in Figure 6.37, composing of large (arrows A) and small (arrow B) dimples with distances comparable with thickness of α platelets and void size. On the fracture surface the pull-out β phase as shown in Figure 6.39 also proved relatively high ductility of the β phase.

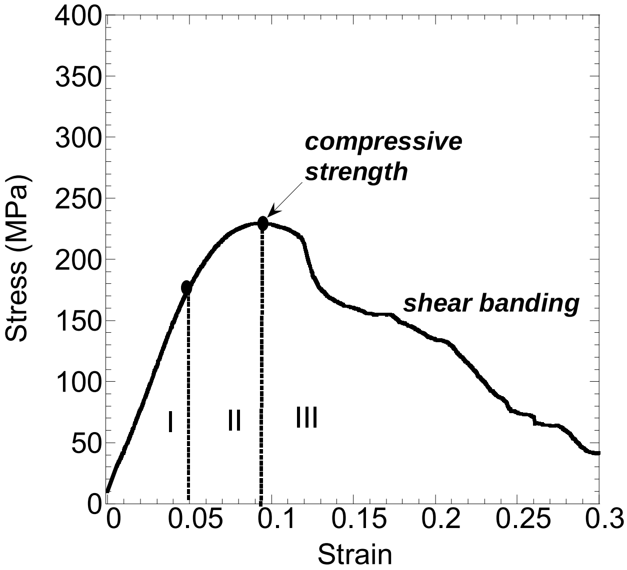

Figure 6.32 Compressive stress-strain curve of Powder A compact of 36% porosity, showing 3 regions of deformation; I: elastic, II: inelastic and III: shear banding.

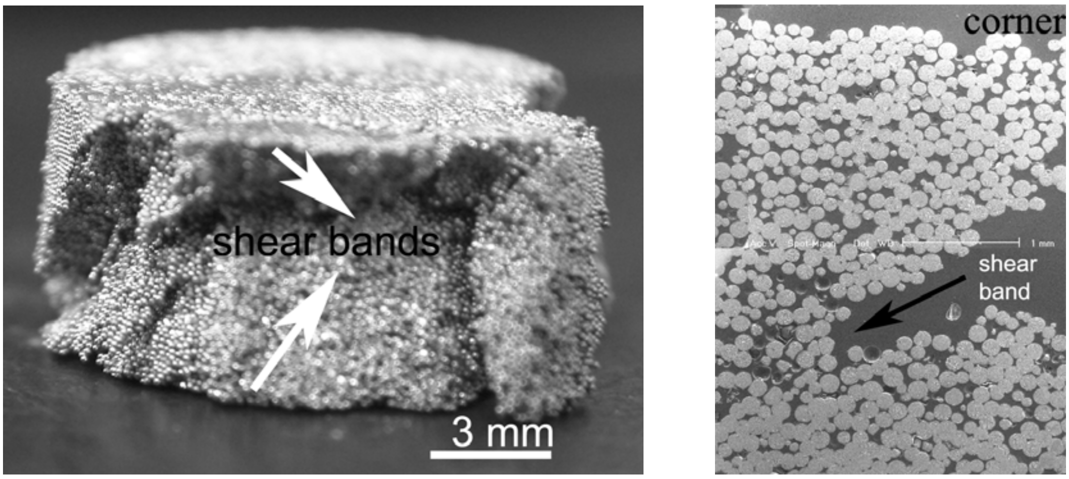

(a)

(b)

Figure 6.33 Shear bands formed in Powder A compacts (a) Shear bands in a failed Powder A sample (100-200 µm) tested at $1.6\text{x}10^{-3}$ s^{-1} and (b) The montages SEM images of Powder A compact sample (100-200 µm) tested at 300 s^{-1}, showing shear band progression starting from the corner, in Region III of Figure 6.32.

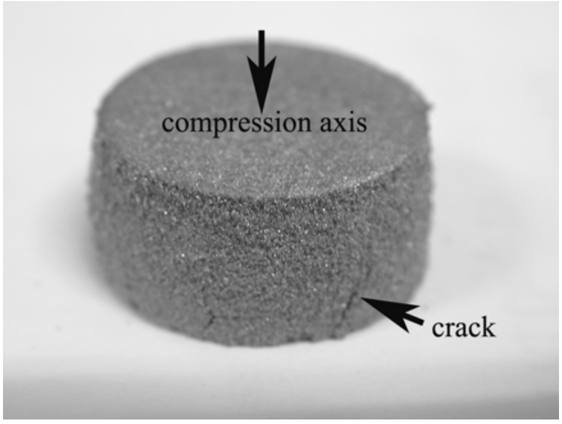

Figure 6.34 Compression tested (30% strain) Powder A compact of particle size <100 μm compacted at 500 MPa.

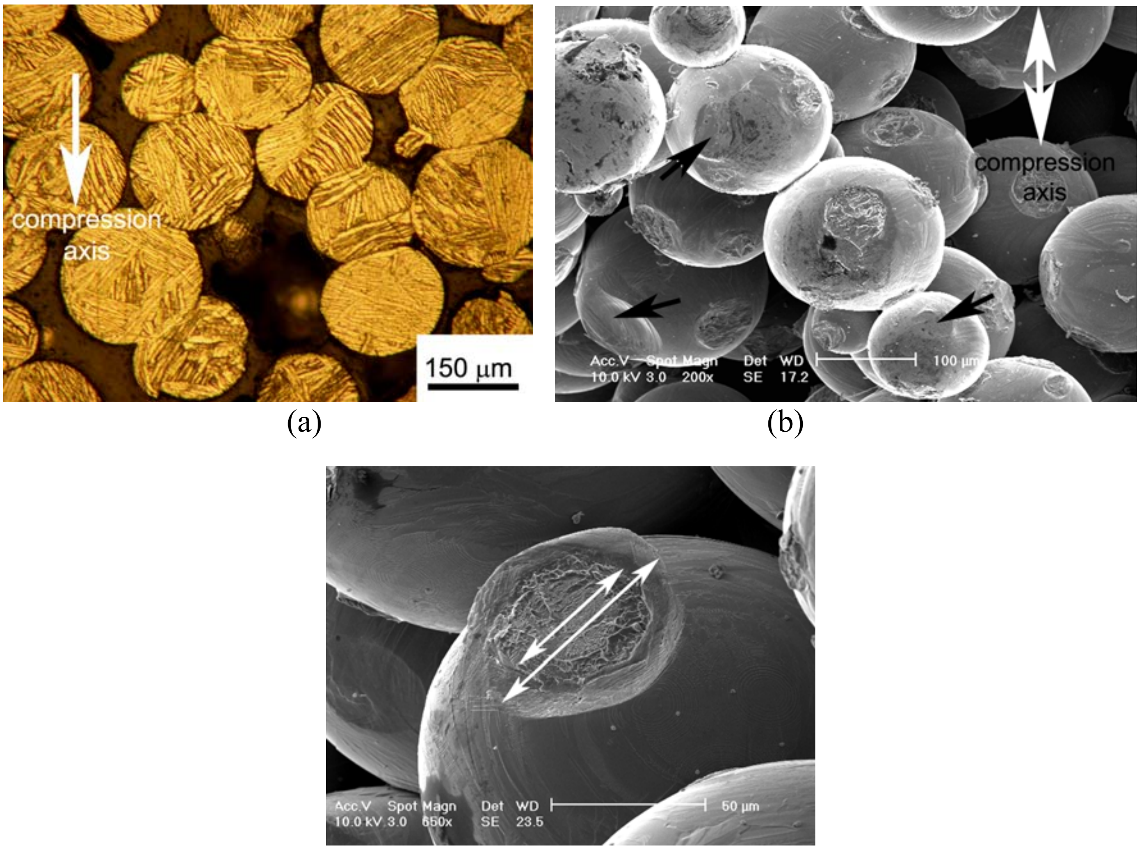

(a) (b)

(c)

Figure 6.35 Images of tested Powder A compact sample (100-200 μm) showing (a) complex deformation of particles in contact near to shear band (b) separated particles on the shear band and (c) interparticle bond area and contact region on a separated particle.

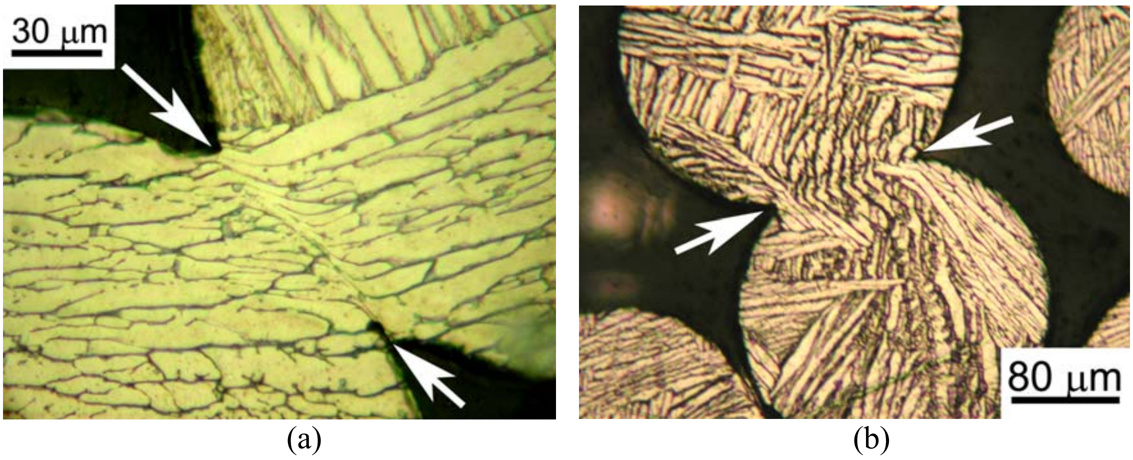

(a) (b)

Figure 6.36 Development of localized shear regions in interparticle bond regions of Powder A compact samples tested (a) $1.6x10^{-3}$ s^{-1} and (b) 900 s^{-1}.

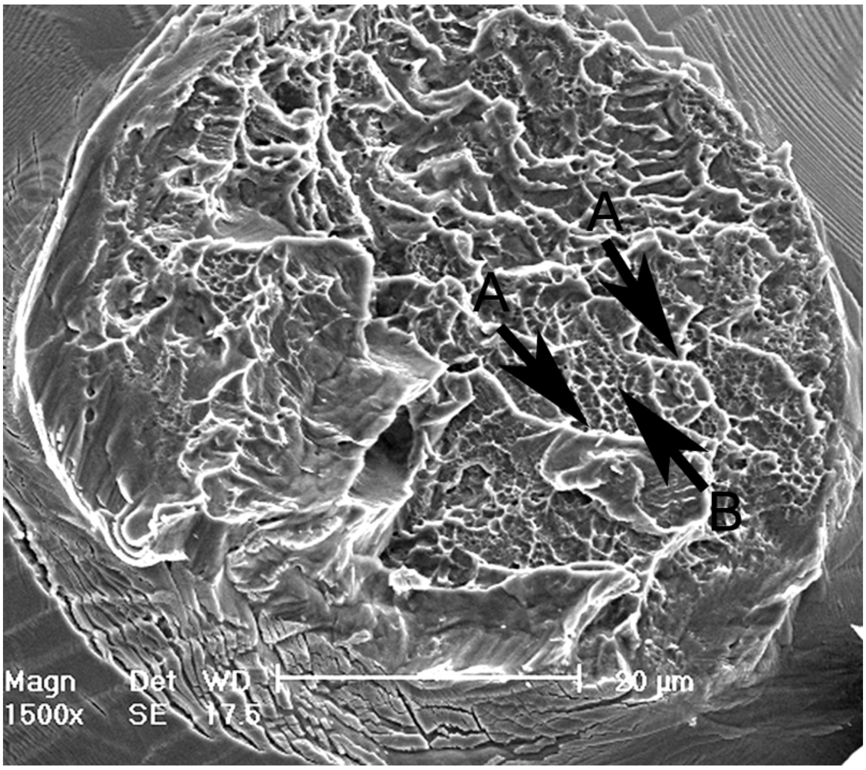

Figure 6.37 Dimpled mode of failure of interparticle bond region (Powder A sample tested $1.6x10^{-}s^{1}$).

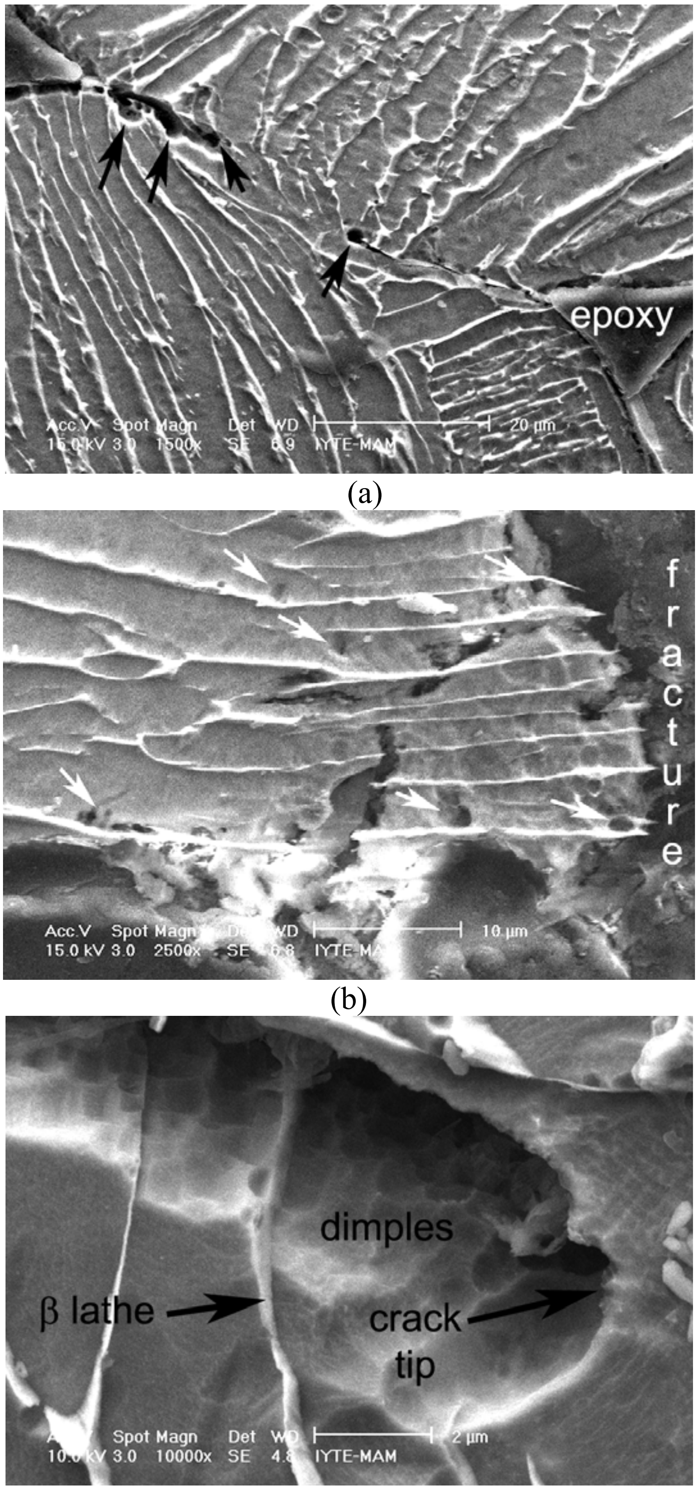

(a)

(b)

(c)

Figure 6.38 Voids and macrocraks at (a) interparticle bond region and (b) near the failed bond region and (c) interior and crack tip of a macrocrack in interparticle bond region (Powder A sample tested at $1.6x10^{-3}s^{-1}$).

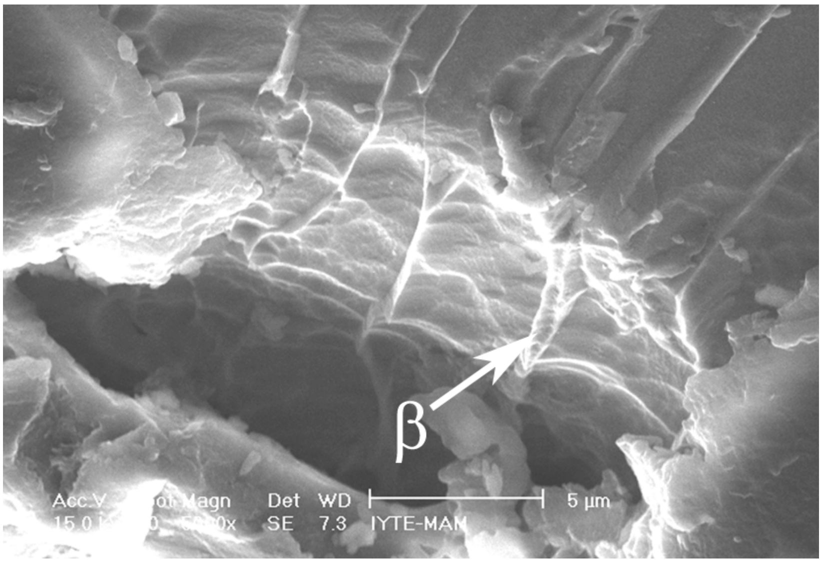

Figure 6.39 Fracture surface of particle of Powder A compact showing pull-out β lathe and dimpled fracture in α phase.

Figures 6.40 and 6.41 show the images of untested samples and tested 100-200 µm particle Powder A and B compacts samples of various compaction pressures, respectively. The failure modes seen in these figures are independent of compaction pressure and very similar for both powder compacts. The fracture surface of Powder B compacts shows however a more brittle type of failure. Figures 6.42 (a-c) also show clearly the difference between the failure modes of <100 µm and larger size of Powder B compacts. In powder B compacts with <100 µm particle size the fracture is transgranular (through the particles) (Figure 6.42 (a)) while the failure in larger size particles through the separation of the interparticle bond region, similar to Powder A compacts (Figures 6.42(b) and (c)). The separation of interparticle bond region is also brittle as seen in Figure 6.43.

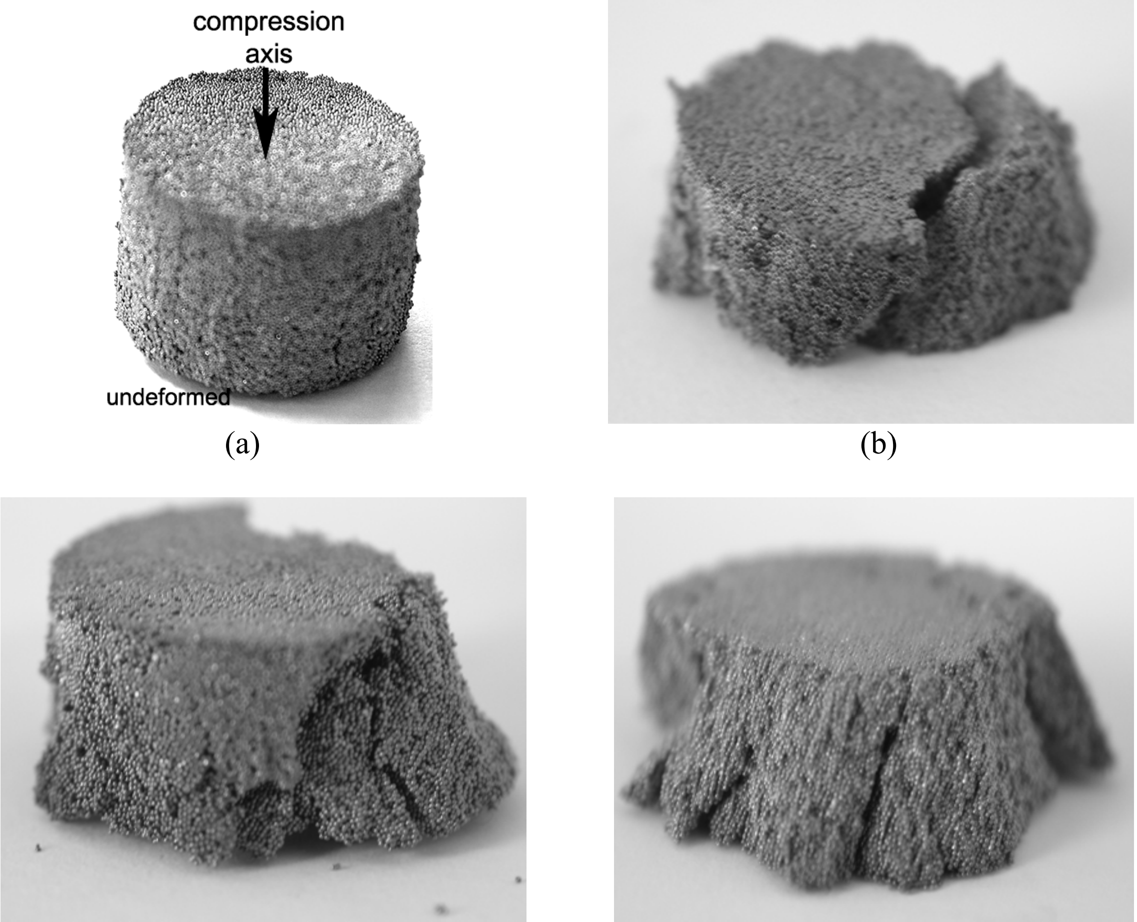

(a) (b)

(c) (d)

Figure 6.40 Undeformed and deformed behavior of Powder A compacts (100-200 μm) (a) Undeformed, (b) 100 MPa, (c) 200 MPa and (d) 500 MPa.

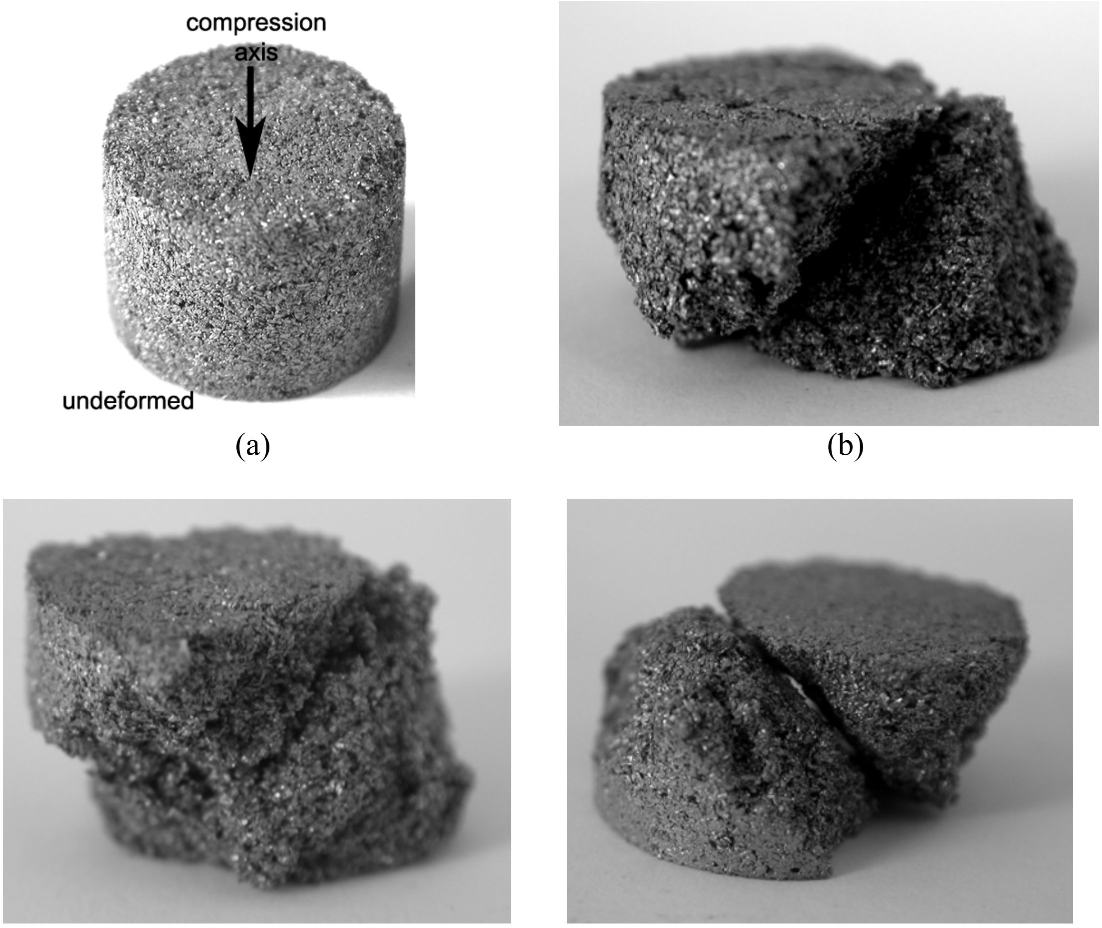

(a) (b)

(c) (d)

Figure 6.41 Undeformed and deformed behavior of Powder B compacts (100-200 μm).

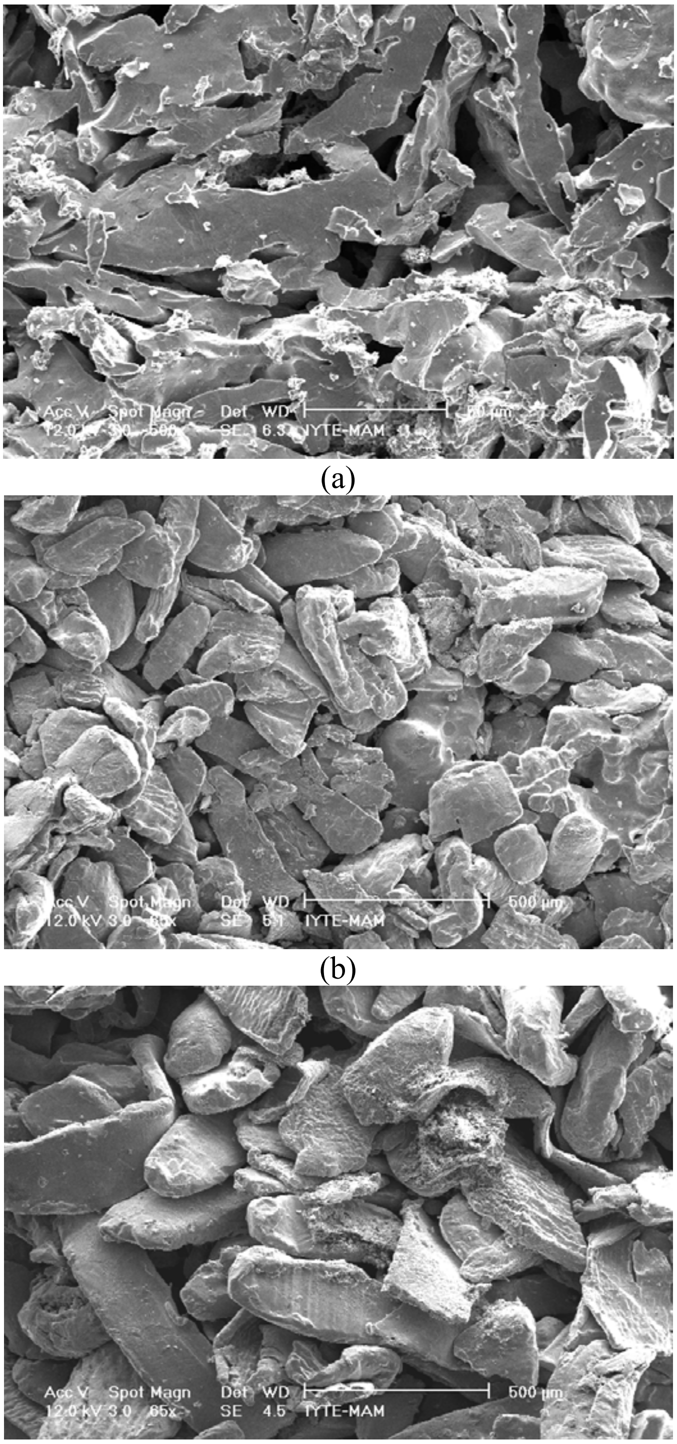

(a)

(b)

(c)

Figure 6.42 Typical fracture surfaces of Powder B compacts (a) <100 μm, (b) 100-200 μm and (c) 200-300 μm.

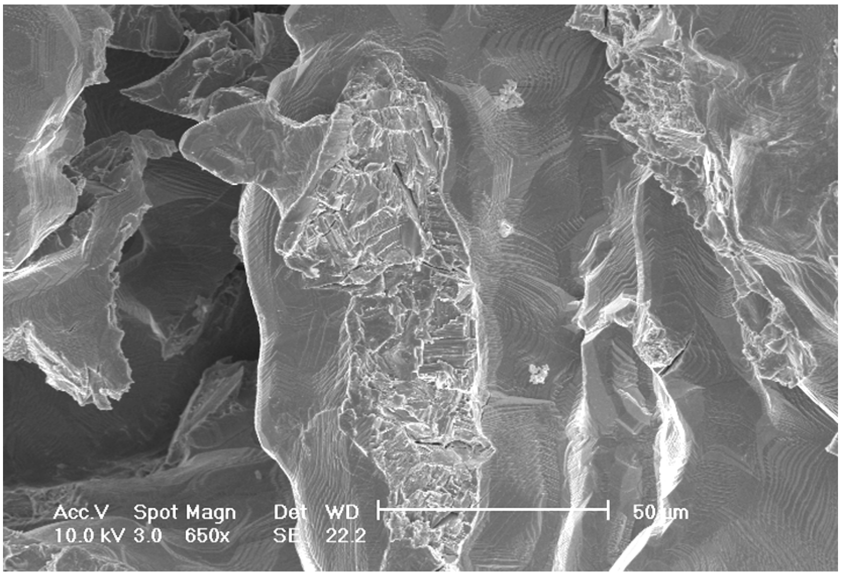

Figure 6.43 Scanning electron micrographs of Powder B compacts of 49% porosity, showing granular fracture at the interparticle bond region.

Chapter 7

DISCUSSION

7.1 Porosity and mean pore size

The mean pore sizes of prepared compacts (29-171 μm) are smaller than the optimum pore size range required for the attachment and proliferation of new bone tissue and the transport of body fluids (200 and 500 μm) [5]. Alternative ways of increasing mean pore size without increasing porosity may include increasing particle size and the addition of predetermined particle size and amount of space holder. Increasing particle size is expected to increase the porosity and hence requires the application of higher compaction pressures in order to reduce the porosity. Tailoring the mean pore size with the use of space holder also requires higher compaction pressures to reach the optimum porosity. The relation between porosity and pore size and the effect compaction pressure with the addition of space holder should therefore be investigated in detail for the manufacturing of implant structures with optimum pore size and porosity. Preliminary experiments with using ammonium bicarbonate (NH_4HCO_3) space holder (200-500 μm in size) were found to be promising in that the mean pore size increased to ~200 μm (see Figure 7.1) while the porosity and compressive strength were kept similar to that of compacts without space holder by increasing the compaction pressures (see Figure 7.2).

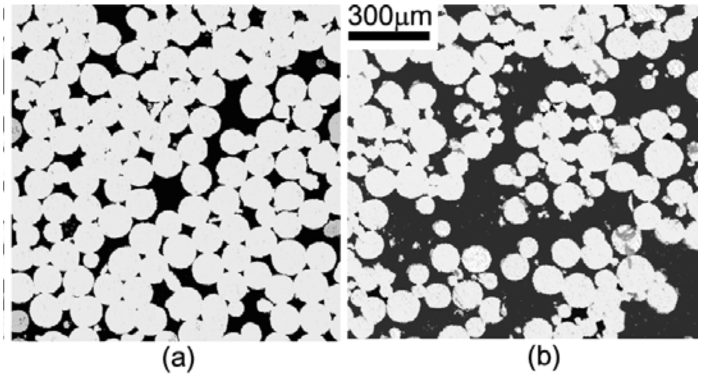

Figure 7.1 Optical micrographs of Powder A compacts of 100-200 μm with porosities of (a) 34% (500 MPa) and (b) 46% with 40% space holder (500 MPa).

Obviously further investigation is required to optimize the porosity and pore size of sintered compacts with the addition of space holder by considering the relations between the process parameters including Ti6Al4V particle size and range, space holder size and amount, compaction pressures and sintering temperature and time.

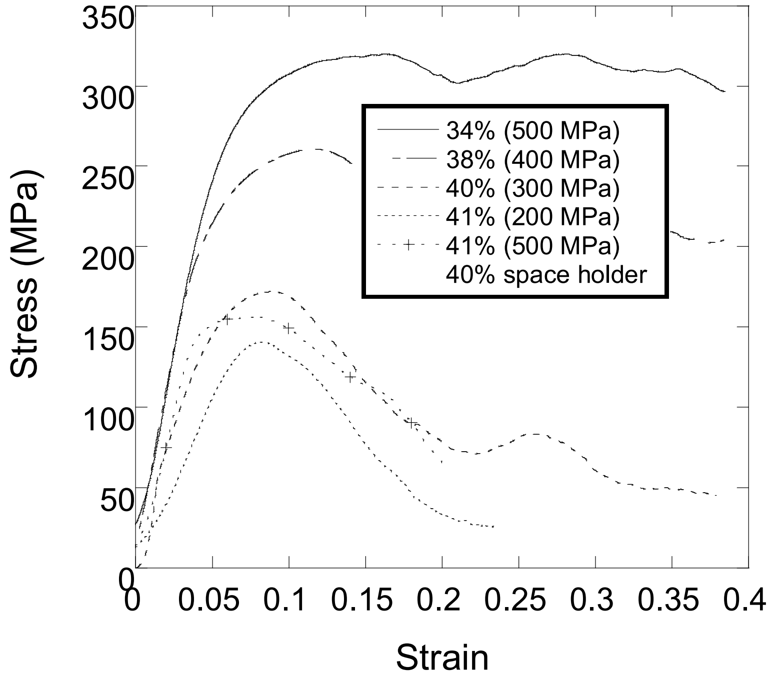

Figure 7.2 Comparison of compression stress-strain curves of Powder A compacts of 100-200 μm and the same powder with 40%, 200-500 μm space holder (NH_4HCO_3).

7.2 Effects of microstructure and particle shape and size on the mechanical properties

Depending on the heat treatment conditions, various microstructures were obtained in bulk Ti6Al4V alloy including Widmanstätten, equiaxed and bimodal microstructures [29]. The Widmanstätten structure is obtained by heat-treatment above β-transition temperature and slow rate of cooling in the furnace. Heat treatment at 950 °C in α+β region followed by furnace cooling results in an equiaxed microstructure, in which β phase is present at triple points of α grains. Bimodal microstructure (α+tempered martensite) is obtained by aging the α+martensite structure (water quenching following heat treatment at 950 °C) at relatively low temperatures (600 °C). When Widmanstätten and equiaxed microstructures were aged at 500-600 °C, nanometer size ordered α_2 (Ti_3Al) phase was precipitated in the α phase [30]. Among above-mentioned microstructures, the highest yield and ultimate tensile strength values were found in bimodal structure and the yield and ultimate tensile strength values of Widmanstätten, equiaxed and bimodal structures were for example sequentially given as 829, 872 and 1070 MPa and 897, 959 and 1134 MPa, respectively [30]. The formation of α_2 phase was also shown to increase yield and ultimate tensile strength of Widmanstätten and equiaxed microstructures [30].

As was expected, the yield and compression strength values of present compacts were significantly lower than those of bulk alloy of the Widmanstätten microstructure tested at quasi-static strain rates (~900 MPa yield strength and ~1600 MPa compression strength [31]). Normalization with the yield strength of bulk alloy gives a normalized compact yield strength value of nearly 0.2 for 40% porosity, ~0.3 for 30% porosity and 0.4 for 20% porosity (Figure 7.3). These values of normalized yield strengths also show good correlations with the values of normalized flow stresses of a porous iron, shown to be 0.4 and 0.3 for 20% and 30% porosities, respectively [32].

Present results have cleared out several important microstructural effects on the mechanical properties of powder compacts. For example at same porosity levels, ~38%, as seen in Figure 7.4 Powder A compact of smallest particle size shows higher yield strength than larger particle sizes. This can be explained with the differences between the contact area radius/particle radius (a/R) ratios of the compacts of similar porosities. From the fracture surfaces of the compacts of similar porosities such as shown in Figures 7.5(a-c), a/R ratios were determined by measuring the radius of circular contact areas and the results are shown in Figure 7.6. Compact of particle size <100 μm has the highest mean a/R ratio, 0.4 followed by compacts of particle size of 100-200 and 200-300 μm with mean a/R ratios of 0.28 and 0.18, respectively. Linear relations between yield and compressive strength of Powder A compacts of 38% porosity and a/R ratios are further shown in Figure 7.7. These results showed that the use of smaller particle size is advantageous as compared with larger particle size in that it will have higher yield and compressive strength at the same porosity levels due to increased contact radius between particles. However, in this case, the mean pore size will be smaller, which should also be taken into consideration.

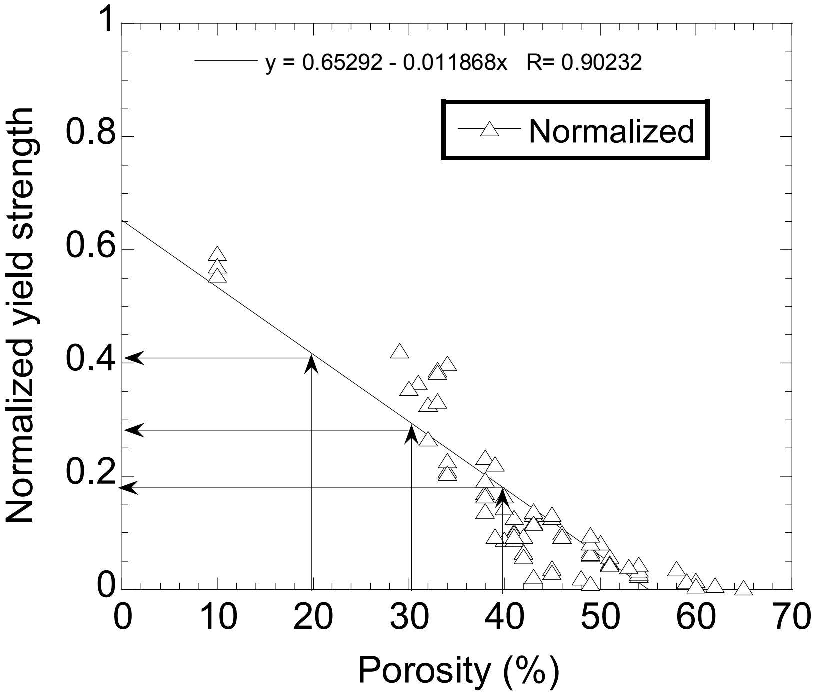

Figure 7.3 Normalized yield strength vs. porosity of powder compacts.

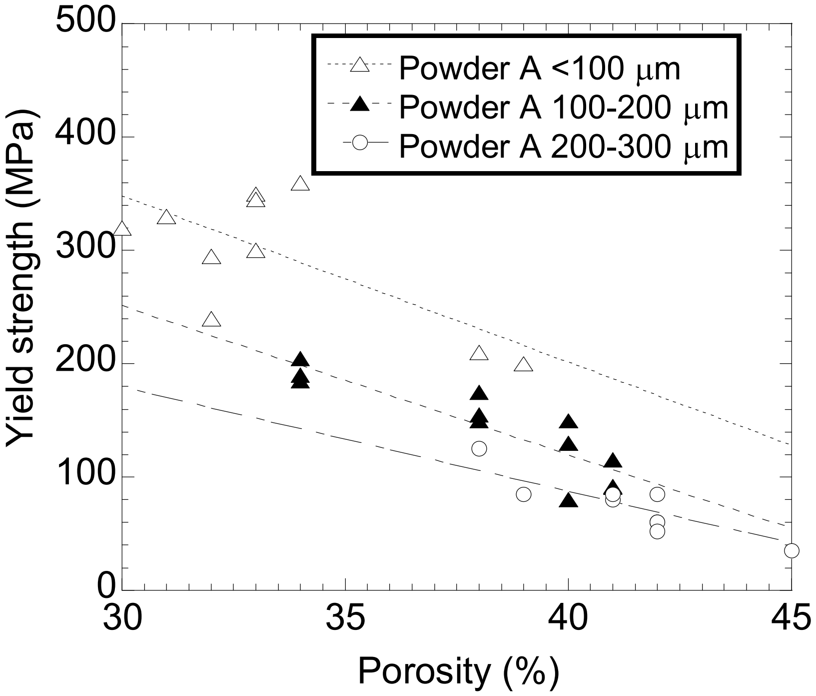

Figure 7.4 Yield strength of Powder A compacts at similar porosity levels.

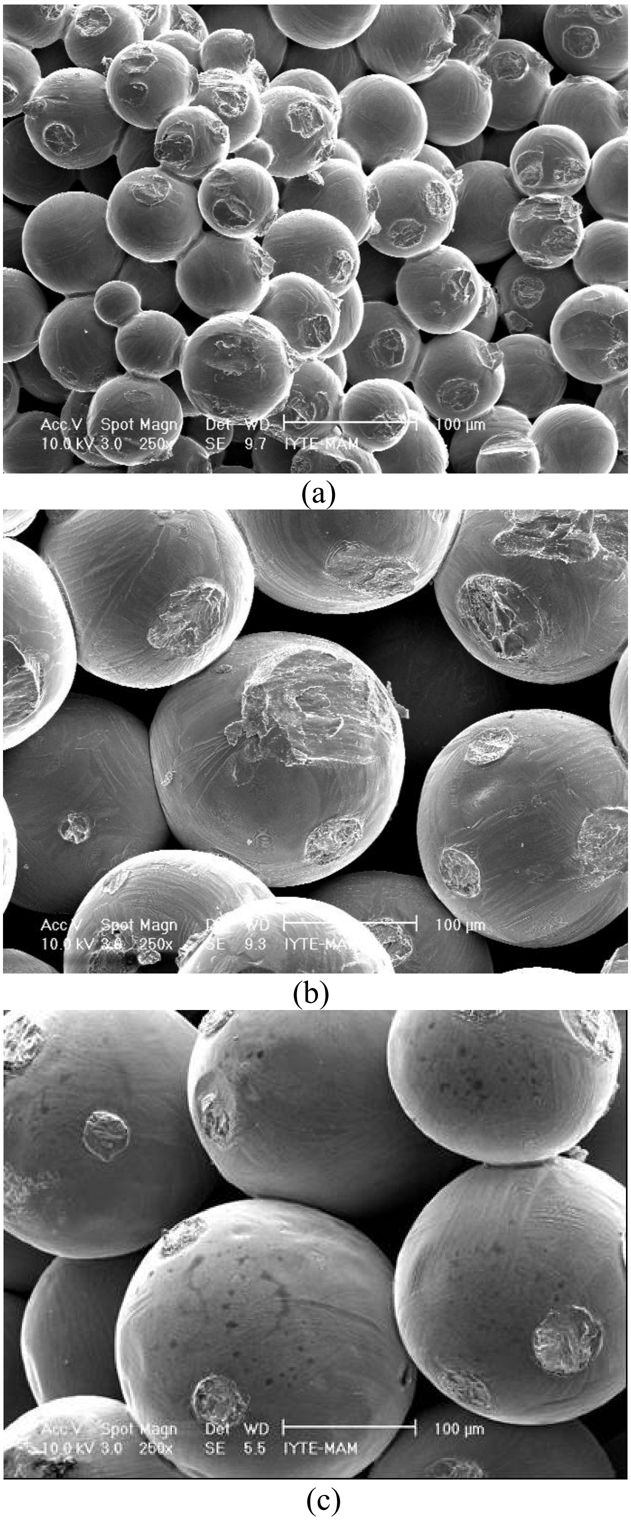

Figure 7.5 SEM micrographs of failed surfaces of Powder A compacts with the same porosity (38%) (a) <100 μm (b) 100-200 μm and (c) 200-300 μm.

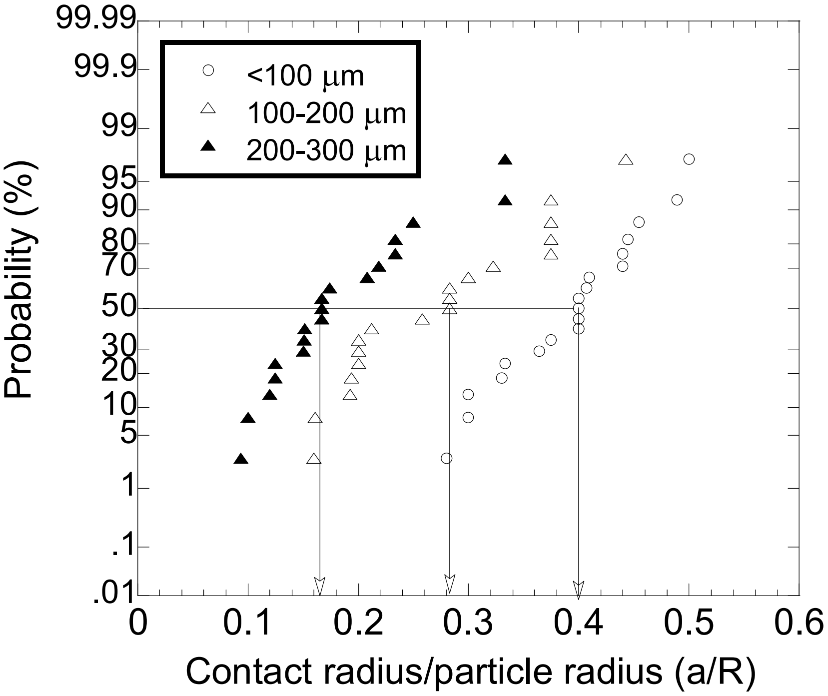

Figure 7.6 Mean a/R ratios of Powder A compacts of ~38% porosity.

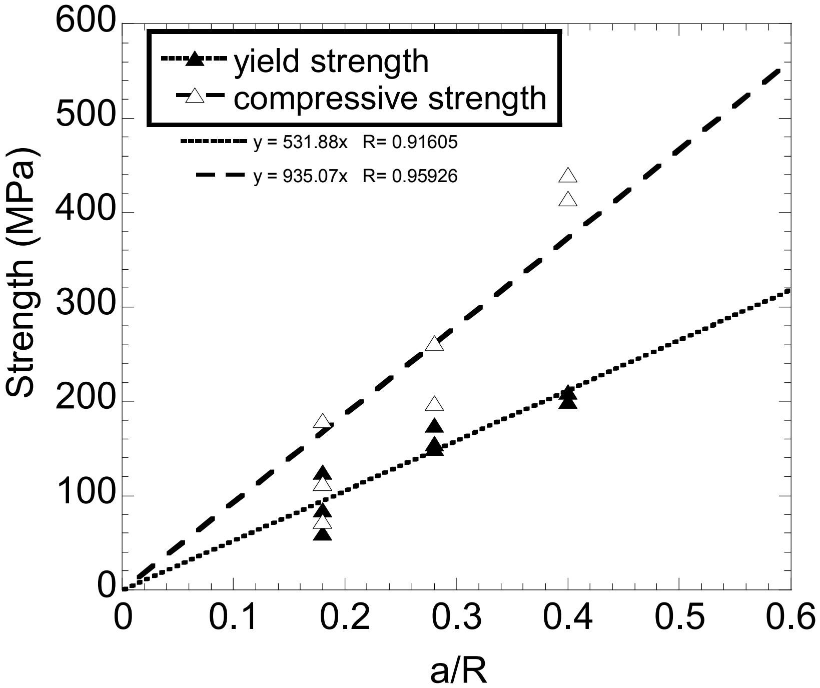

Figure 7.7 Compressive and yield strength of Powder A compacts of 38%-39% porosities vs. a/R ratio.

In contrast to Powder A compacts, in powder B compacts yield and compressive strength decreased as particle size increased. At similar porosity levels, compacts of particle size 200-300 μm show highest yield (Figure 7.8) and compressive strength. A close inspection of the fracture surfaces of the particles have shown that in compacts of particles <100 μm the fracture occurred transgranularly rather than the separation of interparticle bond region as in the case of larger particle size compacts. It was observed that the fracture surfaces of compacts of particles <100 μm contained many small voids (<1 μm in size) which lead to crack initiation sites and eventually brittle type of failure (Figures 7.9 (a) and (b)). The origin of these voids was not known and further microscopy will be needed in order to clarify this. These compacts further failed at a strain of 5% while compacts of larger particle size failed within the strain range of 10-15 % (Figure 7.10). The increased yield and compressive strength of 200-300 μm powder size compacts over the 100-200 μm size compacts at similar porosity levels is likely due to the presence of a higher proportion of equiaxed microstructure in the former. The presence of equiaxed structure in Powder B compacts also explains the higher yield and compressive strength of Powder B compacts than those of Powder A compacts (Widmanstätten structure) at similar porosity levels as shown in Figures 7.11(a) and (b). Due to the higher percentage of equaixed structure in 200-300 μm particle size compacts, the increase is more pronounced in these particle size containing compacts.

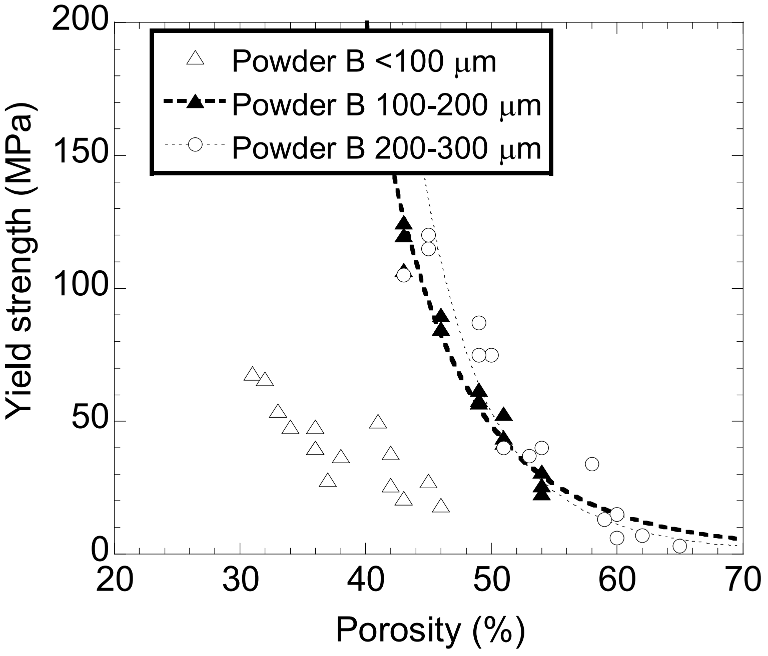

Figure 7.8 Yield strength vs. porosity of Powder B compacts.

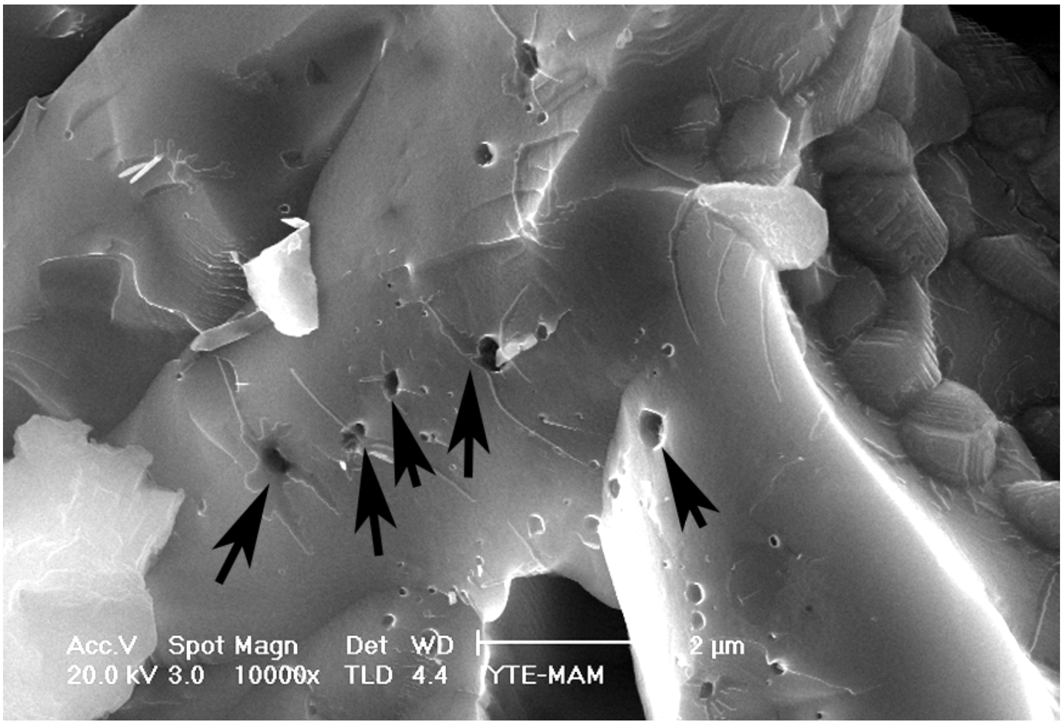

(a)

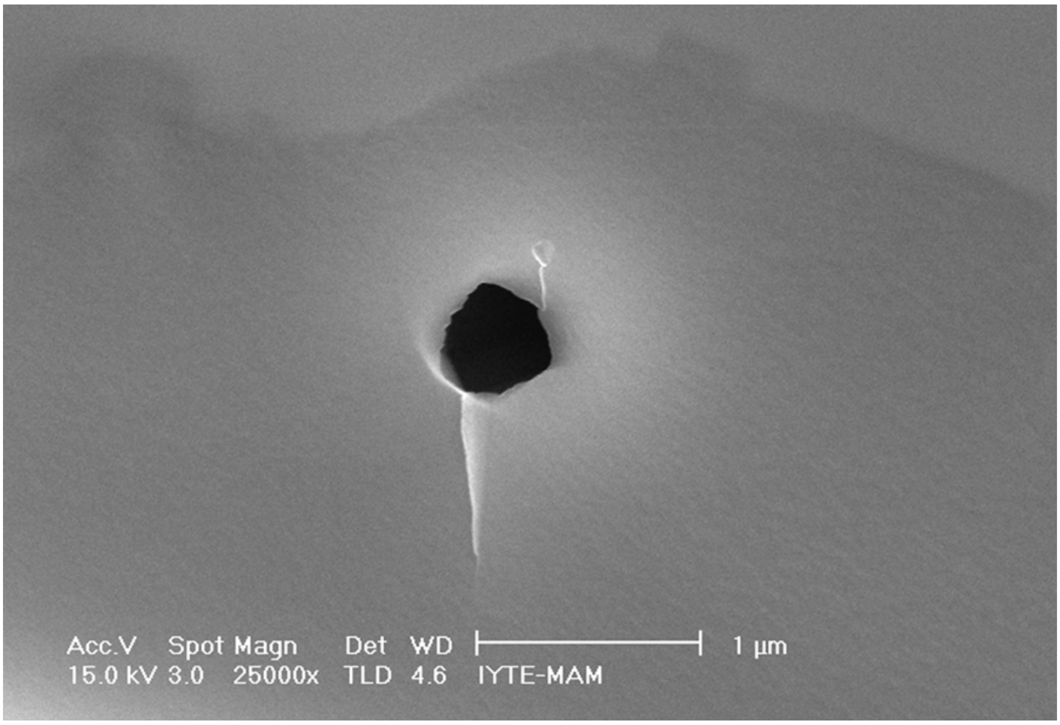

(b)

Figure 7.9 Fracture surface of a particle in Powder B compact of particle size <100 μm (a) voids on the fracture surface of a fractured particle (arrows) and (b) magnified image of a void showing the wing type brittle fracture propagation.

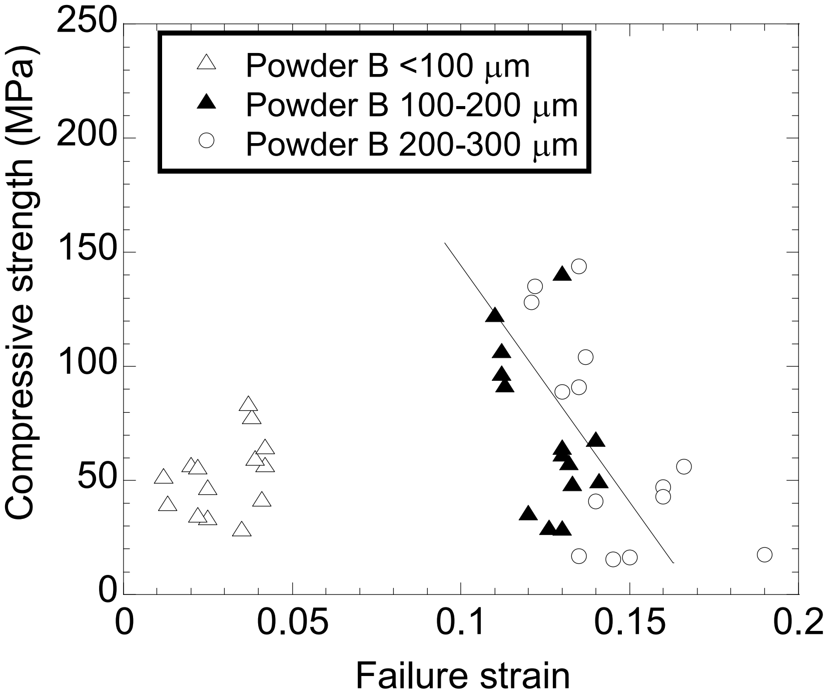

Figure 7.10 Compressive strength vs. failure strain of Powder B compacts, showing relatively low compressive and failure strain of <100 µm particle size compacts.

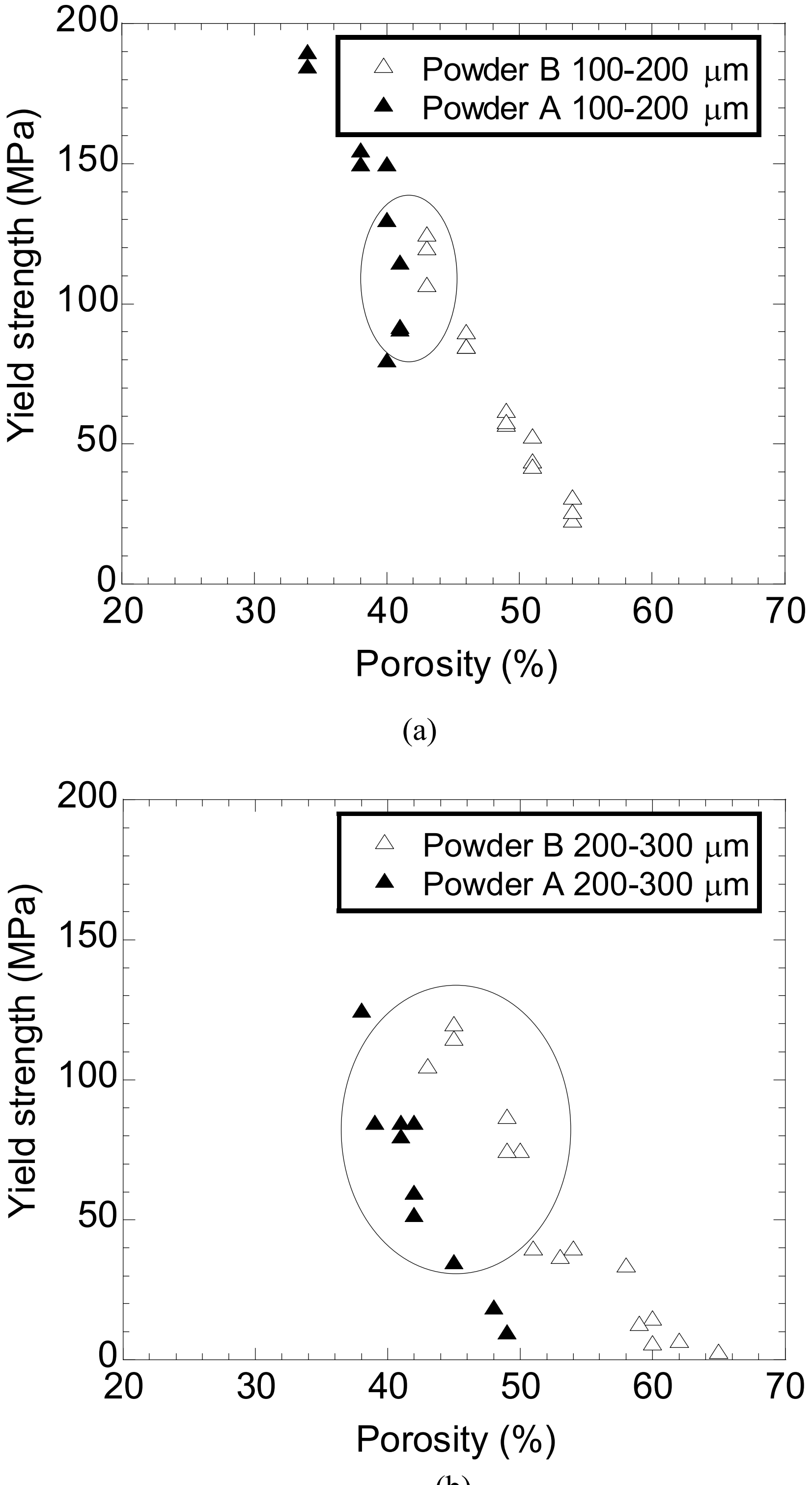

(a)

(b)

Figure 7.11 Comparison of yield strength of Powder B and A compacts at similar porosity levels (a) 100-200 μm and (b) 200-300 μm particle size compacts.

7.3 Effect of strain rate

The strain rate dependent mechanical properties of bulk Ti6Al4V alloy were subjected to several studies [30-33]. Generally, as the strain rate increased both yield and flow stress values were found to increase. It was also shown that the strain rate sensitivities of Widmanstätten and equiaxed microstructures under compression were similar [34]. Silva and Ramesh [31] reported that the percentage increase in flow stress of a bulk Ti6Al4V alloy from quasi-static (10^{-4} s^{-1}) to high strain rates (~1000 s^{-1}) was 30%. In sintered compacts of Powder A Widmanstätten microstructures (38% porous), a similar effect of increasing strain rate on the flow stress (at 5% strain) and compressive strength is also seen in Figure 7.12; the flow and compressive strength increase with increasing strain rate from quasi-static through the high strain rate regime. It is noted that, between the lowest and highest strain rates, the percentage increase in flow stress, about 27%, is very similar with the reported increase in bulk Ti6Al4V alloy (30%). The similar strain rate dependency of powder compact with bulk Ti6Al4V alloy is also in accord with the previous studies on the rate sensitivities of bulk and porous Ti6Al4V [31] and iron alloys [32] and also tends to conclude that powder compact strain rate dependency is merely derived from the rate dependency of bulk Ti6Al4V alloy.

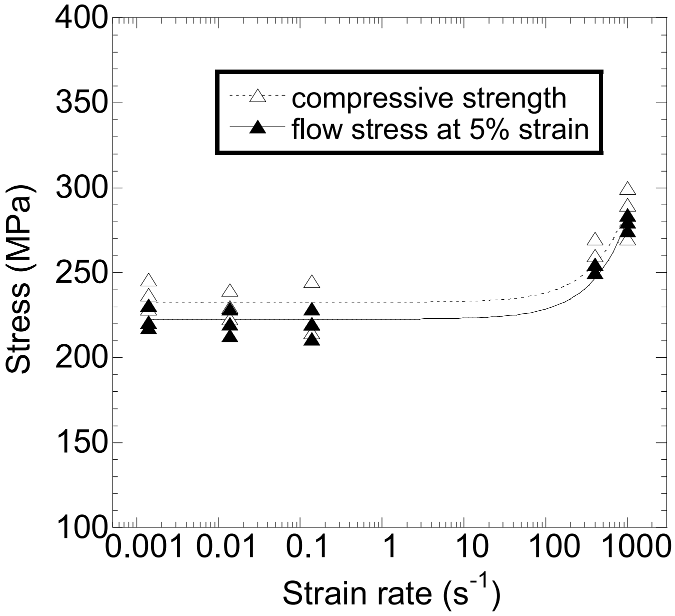

Figure 7.12 Compressive and flow stress vs. log strain rate of Powder A compacts of 36%-38% porosity.

The critical strain, strain corresponding to the maximum stress and at which shear banding presumably started to develop in compacts ranged between 7 and 8% (Figure 6.24), similar with the critical strains (8-10%) for strain localization in a bulk Ti6Al4V alloy tested under compression [31]. It is also interesting to note that the strain rate independent critical strain found in compact within the studied strain rate regime is well agreed with the study of Silva and Ramesh [31], who showed that shear localization in a bulk Ti6Al4V alloy occurred nearly at the same strain at quasi-static and high strain rates. It was also shown by the same authors that the critical strain level was quite different in the Widmanstätten and equiaxed microstructures of a bulk Ti6Al4V alloy; although Widmanstätten microstructure showed strain localization at 8-10% strains, equiaxed structure did not show any localized shearing [31], confirming a strong dependency of mechanical properties on the microstructure.

7.4 Comparison of mechanical properties with those of Ti compacts and human bone

The elastic modulus of compacts prepared within the porosity range of 29% and 63% varied between 0.5 and 17 GPa. The modulus of natural bone is reported to vary between 1 to 20 GPa [21], therefore the elastic modulus range of sintered Ti6Al4V powder compacts are relatively comparable with the elastic modulus of natural bone.

The strength of the sintered Powder A (Figure 7.13) and Powder B (Figure 7.14) compacts within the studied porosity range satisfies the strength requirement for cancellous bone replacement (3-20 MPa) [35]. The yield strength of the cortical bone is however reported to be much higher than that of cancellous bone; within the range of 104-121 MPa [36]. For the studied powder compacts the yield strengths of Powder A and Powder B compacts of 40% and 45% porosity levels are higher than 100 MPa; hence, satisfy the strength requirement for cortical bone replacement. Therefore, the porosity level of the studied powder compacts, which is comparable with the strength of cortical bone ranges in 40% and 45%. A linear interpolation to the data given in Figure 7.15 gives following relation between percent porosity (P) and yield strength;

$$\sigma(\text{MPa}) = 587.63 - 10.681 * \text{P} \tag{1}$$

Eqn.1 predicts a yield strength of 587 MPa for the bulk Ti6Al4V, which is lower than the yield strength of Ti6Al4V which has Widmanstätten or equiaxed microstructure (875-910 MPa, see Table 2.2). Figure 7.15 also shows the variation 0.2% proof strength of Ti compacts (374 μm), which was reported by Oh and co-workers [6]. It is noted in the same figure, compacts of Ti with porosities lower than ~25% satisfy the strength requirement of human cortical bone, whereas the critical porosity increases to ~45% with the use of stronger Ti6Al4V compacts. This, of course, comes with reduced weight and material consumption in the expense of increased cost of use of alloy powder.

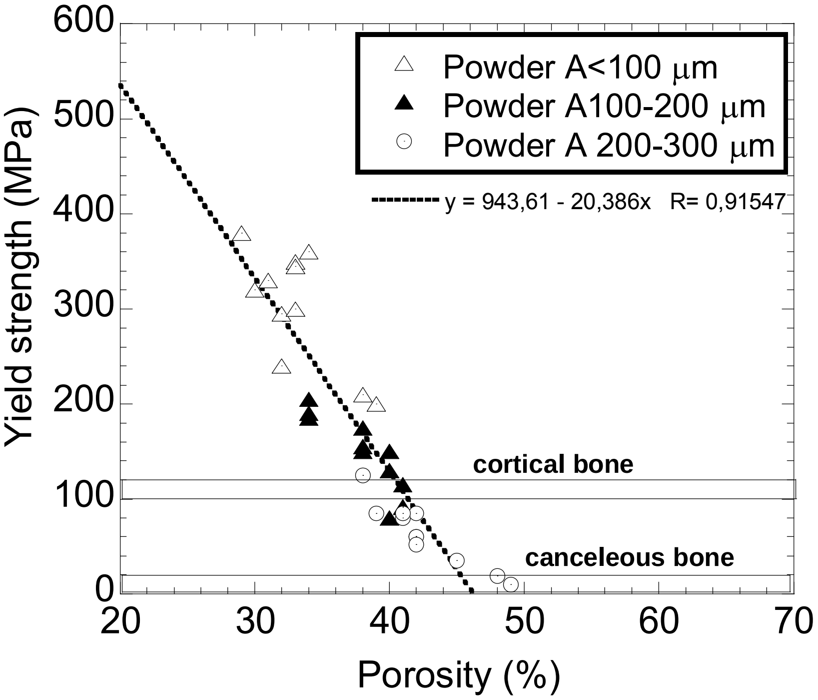

Figure 7.13 Yield strength vs. percent porosity of Powder A compacts and yield strength ranges of cancellous and compact bones.

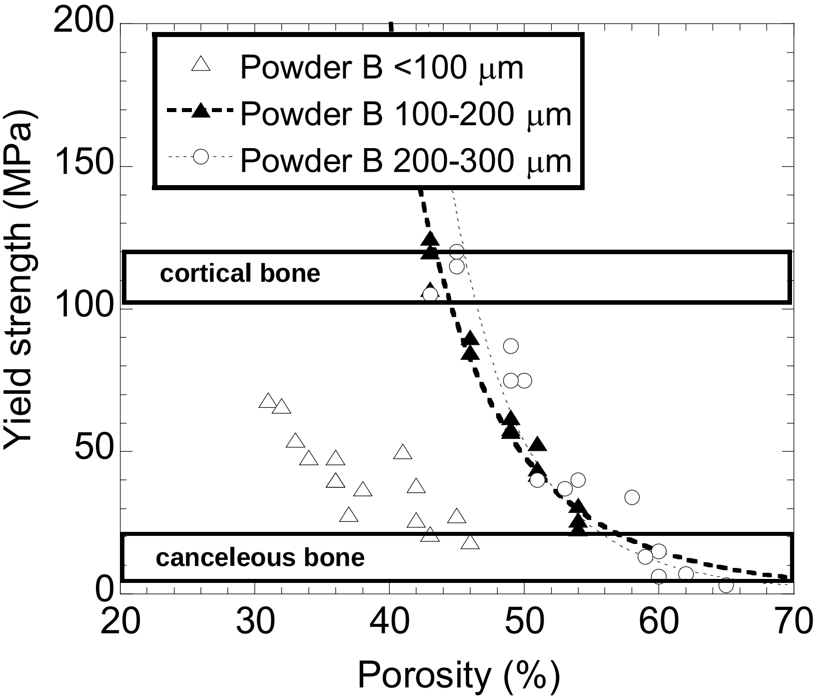

Figure 7.14 Yield strength vs. percent porosity of Powder B compacts and yield strength ranges of cancellous and compact bones.

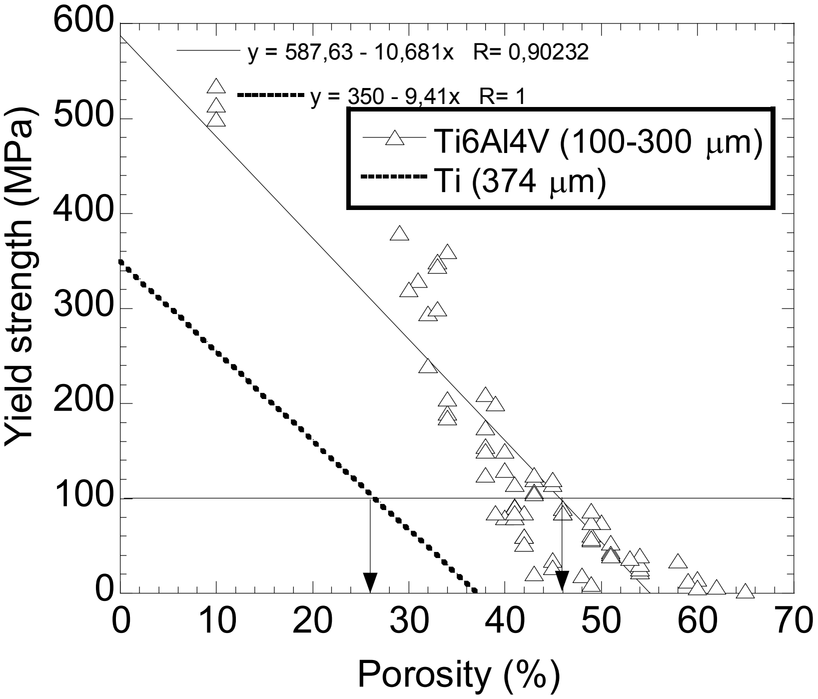

Figure 7.15 Yield strength vs. percent porosity of Ti6Al4V and Ti compacts.

7.5. Summary

Present study has shown that sintered Ti6Al4V compacts with a porosity level of 40-45% satisfy the strength requirement for the cortical bone replacement. The increase in flow stress and compressive strength of compacts with increasing strain rate without any significant reduction in critical strain for localization is certainly beneficial in order to manage sudden increases in the loading rates during service. One of the limitations towards the use of powder compact implants is the relatively low critical strains for shear localization, which could be further optimized with the control of microstructure development and microstructural parameters including percentages and thicknesses of α and β phases through the heat treatment processes applied to bulk Ti6Al4V alloy. Future investigations will therefore be focused on this issue: development of relationships between microstructure and mechanical properties for mechanical property optimization of powder compacts.

Chapter 8

CONCLUSIONS AND RECOMMENDATIONS

Porous sintered powder compacts of Ti6Al4V alloy were prepared in the porosity range of 29%-63% using atomized spherical (Powder A) and angular powders (Powder B) by varying the cold compaction pressure. Cylindrical green powder compacts were cold compacted at various pressures and then sintered at 1200 ^{o}C for 2 hours. The final porosities and average pore sizes were determined as functions of the applied compaction pressure and powder type. The mechanical properties were investigated through compression testing at quasi-static and high strain rate. Microstructural analysis of as-received powder and sintered untested and tested compact samples were performed in order to investigate microstructure development after sintering and deformation and failure mechanisms under compressive loads. The following results were concluded;

1. The final porosities of the compacts were found as functions of the applied cold compaction pressure, powder size and the powder type used.
2. Increasing compaction pressure decreased the final porosities in both sintered powder compacts. The porosity level of compacts ranged between 29% and 63%.
3. In general, due to the angular particle shape, a higher level of porosity was found in Powder B than Powder A compacts at the same compaction pressures.
4. The mean pore size of compacts ranged between 34 and 171 μm depending on the particle size range of the powders. The mean pore size attained in compacts was further found to be smaller than the optimum pore size range required for the attachment and proliferation of new bone tissue and the transport of body fluids (200 and 500 μm). To increase the mean pore size without significantly reducing the strength, the addition of space holder material of certain size range in combination with the higher compaction pressures was recommended.

5. Sintering at high temperature (1200 ^{o}C) and subsequent slow rate of cooling resulted in change of the microstructure of Powder A from acicular α to the Widmanstätten and Powder B from bimodal to equaixed + Widmanstätten.
6. In compression testing, at both quasi-static and high strain rates, the compacts failed primarily via shear bands formed along diagonal axis, 45° to the loading direction. Increasing strain rate was found to increase both flow stress and compressive strength of Powder A compact but it did not affect the critical strain for shear localization.
7. The elastic modulus of compacts prepared within the porosity range of 29% and 63% was relatively comparable with the elastic modulus of natural bone.
8. The mechanical properties of Powder B compacts were further shown to be a function of powder size; larger the particle size higher the percentage of equiaxed structure while in compacts of particles <100 μm relatively large voids lead to reduced strength and ductility.
9. Microscopic analyses of deformed but not failed and failed Powder A compacts have further shown that fracture occurred in a ductile (dimpled) mode consisting of void initiation and growth in α phase and/or at the α/β interface and macrocracking by void coalescence in the interparticle bond region. In Powder B compacts, the failure was granular brittle type at the interparticle bond region while the compact sample of particles <100 μm fractured transgranularly through the voids.
10. The strength of the sintered compacts was shown to satisfy the strength requirement for cancellous bone replacement. The strength of the compacts having a porosity level of 40% and/or lower was further found to be comparable with that of human cortical bone.
11. Compared to Ti powder compacts of previous studies, Ti6Al4V powder compacts provided higher strength and hence increased porosity level of the compacts may be suitable for cortical bone replacement.
12. The effects of the microstructural morphology of powders on the mechanical properties of compacts and the fatigue performance of optimized and selected compacts under cyclic compressive stresses should be further investigated.

13. The effect of heat treatment processes such as precipitate hardening on the mechanical properties of the compacts should be determined in order to tailor the mechanical properties further.

REFERENCES

[1] S. Ramakrishna, J. Mayer, E. Wintermantel, W.L. Kam, “Biomedical applications of polymer-composite materials: a review,” *Composites Science and Technology* **61**, (2001), 1189-1224.

[2] R.M. Pillar, “Porous-surfaced metallic implants for orthopaedic applications,” *Journal of Biomedical Materials Research* **21**, (1987), 1-3.

[3] M. Long, H.J. Rack, “Titanium Alloys in Total Joint Replacement –A Material Science Perspective,” *Biomaterials* **19**, (1998), 1621-1639

[4] M. Bram, C. Stiller, H.P. Buchkremer, D. Stover, H. Baur, “High Porosity Titanium, Stainless Steel and Superalloy Parts,” *Advanced Engineering Materials* **2**, (2000), 196-199

[5] C.E. Wen, Y. Yamada, K. Shimojima, Y. Chino, T. Asahina, M. Mabuchi, “Processing and Mechanical Properties Of Autogenous Titanium Implant Materials,” *Journal Of Material Science : Materials In Medicine* **13**, (2002), 397-401

[6] I.H. Oh, N. Nomurea, S. Hanada, “Mechanical Properties of Porous Titanium Compacts Prepared by Powder Sintering,” *Scripta Materiala* **49**, (2003), 1197-1202

[7] Y.N. Yeni, D.P. Fyrie, “A rate-dependent microcrack-bridging model that can explain the strain rate dependency of cortical bone apparent yield strength,” *Journal of Biomechanics* **35**, (2003), 1343-53.

[8] H.L. Freese, M.G. Volas, J.R.Wood, and M. Textor, ” Titanium and its Alloys in Biomedical Engineering,” *Encyclopedia of Materials: Science and Technology*, (2001), 9374-9381

[9] M. Hagiwara, S. Emura, “Blended elemental P/M synthesis and property evaluation of Ti-1100 alloy,” *Materials Science and Engineering* **A352**, (2003), 85-92

[10] J.O. Peters, B.L. Boyce, X. Chen, J.M. McNaney, J.W. Hutchinson,.O. Ritchie, “On the application of the Kitagawa–Takahashi diagram to foreign-object damage and high-cycle fatigue,” *Engineering Fracture Mechanics* **69**, (2002), 1425-1446

[11] F.H. Froes, T.L. Yau, H.G. Weidinger, Titanium, Zirconium and Hafnium, in *Materials Science and Technology*, edited by K.H. Matucha, (Weinheim, New York, 1996), p.403.

[12] S.L. Semiatin, T.R. Bieler, "The Effect of Alpha Platelet Thickness On Plastic Flow During Hot Working of Ti–6Al–4V with a Transformed Microstructure," *Acta materiala* **49,** (2001) 3565–3573

[13] S.C. Liao, J. Duffy, "Adiabatic Shear Bands in a Ti6Al4V Titanium Alloy," *Journal of the Mechanics* and Physics of Solids **46**, (1998), 2201-2231

[14] A. Molinari, C. Musquar, G. Sutter, "Adiabatic shear banding in high speed machining of Ti–6Al–4V: experiments and modeling," *International Journal of Plasticity* **18**, (2002), 443–459

[15] W.S. Lee, C.F. Lin, "Plastic deformation and fracture behaviour of Ti–6Al–4V alloy loaded with high strain rate under various temperatures," *Materials Science and Engineering* **A241**, (1998), 48–59

[16] Q. Xue, M.A. Meyers, V.F. Nesterenko, "Self-organization of shear bands in titanium and Ti–6Al–4V alloy," *Acta Materialia* **50**, (2002), 575–596

[17] M.A. McGee, "Implant retrieval studies of the wear and loosening of prosthetic joints: a review," *Wear* **241**, (2000), 158-165

[18] E.S. Thian, N.H. Loh, K.H. Khor, S.B. Tor, "Microstructures and Mechanical Properties of Powder Injection Molded Ti-6Al-4V/ HA Powder," *Journal of Materials Science Letters* **22**, (2003), 775-778

[19] V. Amigo, M.D. Salvador, F. Romero, C. Solves, J.F. Moreno, "Microstructural Evolution of Ti-6Al-4V During the sintering of Microspheres of Ti for Orthopedic Implants," *Journal of Materials Processing Technology* **141**, (2003), 117-122

[20] Oh I.H., N. Nomurea, S. Hanada, Microstructure and Mechanical Properties of Porous Titanium Compacts Prepared by Powder Sintering, *Material Transactions* **3**, (2002), 443-446

[21] J.Y. Rho, L.K. Spearing, P. Zioupos, "Mechanical Properties and the Hierarchical Structure of Bone," *Medical Engineering & Physics* **20**, (1998), 92-102

[22] M. Guden, E. Celik, S. Cetiner, A. Aydin, "Metal Foams for Biomedical Applications: Processing and Mechanical Properties," *Biomedical Science and Technology* **20**, (2004)

[23] C. W. Smith and C. P. Winlove, “Elastic Behavior of Biological Materials,” *Encyclopedia of Materials: Science and Technology*, (2001), 2384-2387

[24] W. Pompe, M. Gelinsky, “Biological Structures: Failure,” *Encyclopedia of Materials: Science and Technology*, (2001), 580-584

[25] J. Bahnhart, Manufacture, “Characterization and Application of Cellular Metals and Metal Foams,” *Progress In Material Science* **46**, (2001), 559-632

[26] C. Korner, R.F. Singer, “Processing of Metal Foams-Challenges and Opportunities,” *Advanced Engıneerıng Materıals* **2**, (2000), 159-165

[27] ASTM F 1580-95, Standard specification for titanium and Ti6Al4V alloy powders for coating surgical implants.

[28] M. Güden, I.W. Hall, “High strain-rate compression testing of a short-fiber reinforced aluminum composite,” *Materials Science and Engineering* **A232**, (1997), 1-10.

[29] R.R. Boyer, Titanium and titanium alloys, in *ASM Metals Handbook*, edited by J. Newby, (ASM International, USA, 1989), p. 460.

[30] D.G. Lee, S. Lee, C.S. Lee, “Quasi-static and dynamic deformation behaviour of Ti-6Al-4V alloy containing α_2-Ti_3Al precipitates,” *Materials Science and Engineering* **A366** (2004), 25–37

[31] M.G. Silva, K.T. Ramesh, “The rate-dependent deformation and localization of fully dense and porous Ti-6Al-4V,” *Mater Science and Engineering* **A232**, (1997), 11-22

[32] M.G. Silva, K.T. Ramesh, “The rate dependent deformations of porous pure iron,” *International Journal of Plasticity* **13**, (1997), 587-610.

[33] N.S. Nasser, W.G. Guo, V.F. Nesterenko, S.S. Indrakanti, Y.B. Gu, “Dynamic response of conventional and hot isostatically pressed Ti-6Al-4V alloys: experiments and modeling,” *Mechanics of Materials* **22**, (2001), 425-39.

[34] A.J.W. Johnson, C.W. Bull, K.S. Kumar, C.L. Briant, “The influence of microstructure and strain rate on the compressive deformation behaviour of Ti-6Al-4V,” *Metallurgical and Materials Transactions* **34A**, (2003), 295-306.

[35] F. Tencer, K.D. Johnson, Factors affecting the strength of bone, in *Biomechanics in orthopaedic trauma: bone fracture and fixation*, (Martin Dunitz Ltd, London, 1994), p. 954-962.

[36] A.H. Burstein, D.T. Reilly, M. Martens, “Aging of bone tissue: mechanical properties,” *Journal of Bone and Joint Surgery* **58A**, (1976), 82-86.